



Lecture Notes in Mechanical Engineering

Sabareesh Geetha Rajasekharan  
Srinivasan Arunachalam  
Pabbisetty Harikrishna *Editors*

# Proceedings of the 9th National Conference on Wind Engineering

 Springer

# Lecture Notes in Mechanical Engineering

## Series Editors


Fakher Chaari, National School of Engineers, University of Sfax, Sfax, Tunisia

Francesco Gherardini , Dipartimento di Ingegneria “Enzo Ferrari”, Università di Modena e Reggio Emilia, Modena, Italy

Vitalii Ivanov, Department of Manufacturing Engineering, Machines and Tools, Sumy State University, Sumy, Ukraine

Mohamed Haddar, National School of Engineers of Sfax (ENIS), Sfax, Tunisia

## Editorial Board

Francisco Cavas-Martínez , Departamento de Estructuras, Construcción y Expresión Gráfica Universidad Politécnica de Cartagena, Cartagena, Murcia, Spain

Francesca di Mare, Institute of Energy Technology, Ruhr-Universität Bochum, Bochum, Nordrhein-Westfalen, Germany

Young W. Kwon, Department of Manufacturing Engineering and Aerospace Engineering, Graduate School of Engineering and Applied Science, Monterey, CA, USA

Justyna Trojanowska, Poznan University of Technology, Poznan, Poland

Jinyang Xu, School of Mechanical Engineering, Shanghai Jiao Tong University, Shanghai, China

**Lecture Notes in Mechanical Engineering (LNME)** publishes the latest developments in Mechanical Engineering—quickly, informally and with high quality. Original research reported in proceedings and post-proceedings represents the core of LNME. Volumes published in LNME embrace all aspects, subfields and new challenges of mechanical engineering.

To submit a proposal or request further information, please contact the Springer Editor of your location:

**Europe, USA, Africa:** Leontina Di Cecco at [Leontina.dicecco@springer.com](mailto:Leontina.dicecco@springer.com)

**China:** Ella Zhang at [ella.zhang@springer.com](mailto:ella.zhang@springer.com)

**India:** Priya Vyas at [priya.vyas@springer.com](mailto:priya.vyas@springer.com)

**Rest of Asia, Australia, New Zealand:** Swati Meherishi at [swati.meherishi@springer.com](mailto:swati.meherishi@springer.com)

Topics in the series include:

- Engineering Design
- Machinery and Machine Elements
- Mechanical Structures and Stress Analysis
- Automotive Engineering
- Engine Technology
- Aerospace Technology and Astronautics
- Nanotechnology and Microengineering
- Control, Robotics, Mechatronics
- MEMS
- Theoretical and Applied Mechanics
- Dynamical Systems, Control
- Fluid Mechanics
- Engineering Thermodynamics, Heat and Mass Transfer
- Manufacturing
- Precision Engineering, Instrumentation, Measurement
- Materials Engineering
- Tribology and Surface Technology.

**Indexed by SCOPUS, EI Compendex, and INSPEC**

All books published in the series are evaluated by Web of Science for the Conference Proceedings Citation Index (CPCI)

To submit a proposal for a monograph, please check our Springer Tracts in Mechanical Engineering at <https://link.springer.com/bookseries/11693>

Sabareesh Geetha Rajasekharan ·  
Srinivasan Arunachalam · Pabbisetty Harikrishna  
Editors

# Proceedings of the 9th National Conference on Wind Engineering

 Springer

*Editors*

Sabareesh Geetha Rajasekharan  
Department of Mechanical Engineering  
Birla Institute of Technology and Science  
Hyderabad, Telangana, India

Srinivasan Arunachalam  
Wind Engineering Application Centre  
Jaypee University of Engineering  
and Technology  
Guna, Madhya Pradesh, India

Pabbisetty Harikrishna  
Wind Engineering Laboratory  
CSIR-SERC  
Chennai, Tamil Nadu, India

ISSN 2195-4356

ISSN 2195-4364 (electronic)

Lecture Notes in Mechanical Engineering

ISBN 978-981-99-4182-7

ISBN 978-981-99-4183-4 (eBook)

<https://doi.org/10.1007/978-981-99-4183-4>

© The Editor(s) (if applicable) and The Author(s), under exclusive license to Springer Nature Singapore Pte Ltd. 2024

This work is subject to copyright. All rights are solely and exclusively licensed by the Publisher, whether the whole or part of the material is concerned, specifically the rights of translation, reprinting, reuse of illustrations, recitation, broadcasting, reproduction on microfilms or in any other physical way, and transmission or information storage and retrieval, electronic adaptation, computer software, or by similar or dissimilar methodology now known or hereafter developed.

The use of general descriptive names, registered names, trademarks, service marks, etc. in this publication does not imply, even in the absence of a specific statement, that such names are exempt from the relevant protective laws and regulations and therefore free for general use.

The publisher, the authors, and the editors are safe to assume that the advice and information in this book are believed to be true and accurate at the date of publication. Neither the publisher nor the authors or the editors give a warranty, expressed or implied, with respect to the material contained herein or for any errors or omissions that may have been made. The publisher remains neutral with regard to jurisdictional claims in published maps and institutional affiliations.

This Springer imprint is published by the registered company Springer Nature Singapore Pte Ltd. The registered company address is: 152 Beach Road, #21-01/04 Gateway East, Singapore 189721, Singapore

# Foreword

I am delighted to know that the Springer publishers are bringing out this compilation of papers selected from amongst those which were presented at the 9th National Conference on Wind Engineering, which was conducted during March 3 and 4 at BITS-Pilani Hyderabad Campus.

The National Conference of Wind Engineering is a premiere conference conducted at regular intervals under the aegis of Indian Society of Wind Engineering (ISWE). The society was established in 1993 and presently has over 500 members. The last conference (8th National Conference on Wind Engineering—8NCWE) was held in 2016–2017 at IIT-BHU. Earlier, premier institutes such as IIT Roorkee, CSIR-Structural Engineering Research Centre (SERC), CSIR-Central Road Research Institute (CRRRI), Thapar University—Patiala, Visvesvarayya National Institute of Technology (VNIT), Jadavpur University, Sardar Vallabhai National Institute of Technology (SVNIT), etc., have hosted this conference.

This is the first time the organisers are bringing selected papers presented in the conference in the form of this volume, and it will benefit the wind engineering community across the globe.

With design of tall and complicated building structures, the field of wind engineering has been growing over the decades worldwide. Wind loading codes in different countries provide a general estimate of wind loads on structures. But when structures become complicated in shape, and terrains become uneven, a more realistic estimation of wind loads through wind tunnel testing or CFD analysis, or machine learning techniques are required. The proceedings brought out as part of 9th National Conference on Wind Engineering compiles papers in these different domains, which will help the practising engineers, students, faculty and researchers to have a comprehensive idea of the latest developments in the field of wind engineering.

Further, the book also presents papers in the wind energy domain, which discusses the various aspects such as design of wind turbine blade aerofoils, wind speed estimation, to name a few.

I believe the readers will surely benefit from the variety of papers compiled here and will also have an improved understanding of the field of wind engineering.

Prof. Prem Krishna  
Former Professor, IIT Roorkee  
Former President  
International Association of Wind  
Engineering (IAWE)  
Former President, Indian Society of  
Wind Engineering (ISWE)  
Gurugram, India

# Preface

Wind Engineering is the branch of science that deals with interaction of wind with man-made structures, and it draws upon the fields of meteorology, fluid dynamics, aerodynamics, structural dynamics, mechanics, instrumentation and geographic information systems.

With the increase in population, the land area for buildings and apartments is depleting at a fast rate, and the only alternative is to have high-rise structures. The design and construction of high-rise structures come with its own challenges. With the increase in height, the wind speed increases and consequently the wind loads acting on these structures also increase. As such the design of these structures demands careful analysis of design wind loads. Requiring similar attention is a whole range of other wind-sensitive structures, such as bridges, power structures, transmission structures and so on.

In a broader sense, wind engineering also includes the harnessing of wind energy to supplement the energy requirements. In this era of global warming, when attempts are being made world over to switch to renewable forms of energy, the developments in the wind energy sector are of prime importance.

This volume is a compilation of papers which addresses the recent advances in the field of wind engineering and wind energy, selected from those presented at the 9th National Conference on Wind Engineering during March 3 and 4 at BITS-Pilani Hyderabad Campus.

Papers contained herein comprise the recent advances in wind tunnel testing and futuristic wind tunnels. Also discussed is the computational approach to deal with wind engineering problems. Further, recent advancements in field of big data and use of data-driven techniques in wind engineering are also included. In the wind energy domain, aerodynamic analysis of wind turbines with focus on blade design, characteristics of aerofoils and their impact on energy harnessed are discussed. The volume also comprises papers on wind climate. In general terms, the proceedings contained herein will provide an overview of latest developments in the field of wind engineering and wind energy. Practising engineers will find it handy for improved understanding for analysing the wind loads while designing buildings, particularly with complicated shapes. For students of wind and structural engineering, the volume



provides a detailed understanding of wind tunnel testing and computational and data-driven analysis in the field of wind engineering.

Hyderabad, India  
Guna, India  
Chennai, India

Sabareesh Geetha Rajasekharan  
Srinivasan Arunachalam  
Pabbisetty Harikrishna

# Contents

<b>Implementation of a Simple CFD Tornado Simulator in Open-Source Software OpenFOAM</b> .....	1
Sumit Verma, R. Panneer Selvam, and Miguel Cid Montoya	
<b>Construction and Calibration of a Low-Speed Variable Velocity Profile Wind Tunnel</b> .....	11
Kalyani Panigrahi, Rohan Bhattacharya, Garima Singh, K. Supradeepan, Sabareesh Geetha Rajasekharan, and P. S. Gurugubelli	
<b>Aerodynamic Characteristics of an Inclined Square Cylinder with Corner Fins</b> .....	19
D. Amith, C. Sarath Mohan, C. M. Hariprasad, and R. Ajith Kumar	
<b>Effect of Unusual Terrain on Local Wind Characteristics</b> .....	31
N. Shafeek, K. Anjana, G. Tom, K. Vivek, A. Cini, P. S. Rahul, and K. Suresh Kumar	
<b>Vibrational Characteristics of the LEP Vertical-Axis Wind Turbine Shaft for Various Solidity Ratios</b> .....	43
E. Karthik Vel, G. Vinayagamurthy, Gao Liang, and S. Nadaraja Pillai	
<b>Performance Analysis of N-Beats and Regression Learners for Wind Speed Forecasting and Predictions</b> .....	51
Jatin Prakash, P. K. Kankar, and Ankur Miglani	
<b>Effect of Turbulence Parameters on Alongwind Response of Tall Rectangular Buildings</b> .....	61
Naveen Kwatra and Abhay Gupta	
<b>Wind Pattern and Dispersion in a T-Intersection Street Canyon</b> .....	71
S. K. Udupi, R. Rao, S. Mahesh, C. Tiwari, L. Singh, and S. J. Pal	

**Errors and Uncertainties in Simulation of Unsteady Viscous Flow Over a Circular Cylinder at  $Re = 48$  . . . . . 81**  
Aravind Seeni, Dhanish Ahamed, Chinni Maadesh, Harish Adishwar, and Ayshwarya Mahadevan

**Aerodynamics Analysis of Industrial Wind Turbines . . . . . 93**  
Chinni Maadesh, Dhanish Ahamed, Harish Adishwar, Ayshwarya Mahadevan, and Aravind Seeni

**Computational Technique Adopted to Study Vortex Formation in Industrial Wind Turbines . . . . . 107**  
Dhanish Ahamed, Chinni Maadesh, Harish Adishwar, Ayshwarya Mahadevan, and Aravind Seeni

**Shear Lag Effect in Framed-Tube Buildings Due to Torsional Wind Load . . . . . 123**  
Ashish Singh, Piyush Gaikwad, and Sasankasekhar Mandal

**Wind-Induced Interference Effects on a 125 m Tall RC Chimney in Typical Power Plant . . . . . 133**  
G. Ramesh Babu, Ramya Niranjana, and A. Abraham

**Studies on 1:300 Scale Wind Tunnel Simulation of Atmospheric Boundary Layer Characteristics Under Open Terrain Conditions Using a State-of-the-Art Boundary Layer Wind Tunnel . . . . . 145**  
Sumit Dubey, S. Arunachalam, Sanjeev Gupta, Rajendra Singh, Sumit Gandhi, and Nitin K. Samaiya

**Tornado Speed Estimation Using Convolutional Neural Networks (CNNs) and Long Short-Term Memory (LSTM)-Based Video Processing Approach . . . . . 153**  
Anirudh Marathe, Prerit Daga, Sudha Radhika, and Yukio Tamura

## About the Editors

**Prof. Sabareesh Geetha Rajasekharan** is an Associate Professor in the Department of Mechanical Engineering, BITS-Pilani Hyderabad Campus. He completed his Ph.D. and Post-doctoral studies in the field of Wind Engineering at Tokyo Polytechnic University, Japan. He has to his credit more than 80 publications in International Journals/Conferences. He has ongoing/completed multiple projects to the tune of 2.2 crore funded by DST/DRDO/other agencies. Under him, four Ph.D. students have graduated and is presently guiding three students. His field of interest are in Wind Engineering, Fluid Structure Interaction, Vibrations, Condition Monitoring, Machine Learning and Artificial Intelligence. He is also a recipient of Best Master's Thesis award in the field of wind engineering constituted by Indian Society of Wind Engineering.

**Prof. Srinivasan Arunachalam** till recently, worked as Director, Wind Engineering Application Centre, Jaypee University of Engineering and Technology, Guna in Madhya Pradesh, since 2013. Earlier, he has worked as Chief Scientist and Head, Wind Engineering Lab at CSIR-SERC, Chennai for about 30 years. He obtained his B.E. (Civil) from Madras University, M.S. (Civil) and Ph.D. from IIT, Madras and from IISc, Bangalore respectively. His field of research interest include wind effects on buildings and structures, boundary layer wind tunnel testing, and cyclone disaster mitigation. He is a recipient of CSIR-DAAD and CSIR-UNDP fellowships. He has published over 105 research papers in journals and conferences and about 200 technical and consultancy reports. He is a Fellow of Indian National Academy of Engineering and Institution of Engineers (India). As a team member, he has contributed to Indian Standards on wind loads.

**Dr. Pabbisetty Harikrishna** is currently Chief Scientist and Head of Wind Engineering Laboratory, CSIR—Structural Engineering Research Centre (CSIR-SERC), Chennai. He obtained his B.E. (Civil Engg.) from Andhra University, Waltair, M.E. (Structural Engg.) from Anna University, Chennai, and Ph.D. from Indian Institute of Technology—Madras, Chennai. His major areas of research interests include Wind

Engineering, wind effects on tall buildings, lattice towers, cooling towers, chimneys and bridge decks, Computational Fluid Dynamics (CFD), application of Data Mining/ML algorithms, and small wind turbines. He has published 18 papers in SCI Journals and 11 papers in reputed National Journals. Dr. Harikrishna received UNDP Fellowship in 1994, A. S. ARYA-UOR Disaster Prevention Award in 2000, Dr. Jai Krishna Medal in 2001, Dr. M. Ramaiah Award in 2004, Springer Best Paper Award in 2016. Currently, he is member of various BIS codal committees relevant to wind loads.

# Implementation of a Simple CFD Tornado Simulator in Open-Source Software OpenFOAM



Sumit Verma, R. Panneer Selvam, and Miguel Cid Montoya

**Abstract** Tornadoes have been reported in the USA, Canada, China, and Europe over the past several decades. While not very common, yet there have been sporadic occurrences of tornadoes in India (e.g., West Bengal tornado outbreak, 2021). Although the occurrence of tornadoes and the economic and human losses seem to be a cosmopolitan problem, the research efforts to develop a better understanding of wind loading of structures during tornadoes are limited to select research groups of prestigious universities in the world. In that regard, the authors have previously pursued CFD modeling work on tornadoes using in-house codes. However, there are inherent challenges in customizing in-house codes if it has to be adapted to user-specific cases. Thus, for the wider accessibility of tornado simulation tools to students and early-career researchers, the details of the implementation of a simple CFD tornado simulator model using open-source software OpenFOAM is discussed in this contribution.

**Keywords** Tornado simulation · Computational fluid dynamics · OpenFOAM

## 1 Introduction

Tornadoes are a common occurrence in the US [1] and have also been reported in Canada [2], China [3], and Europe [4]. While not very common, yet there have been sporadic occurrences of tornadoes in India [5]. Thus, the occurrence of tornadoes and the economic and human losses caused by these severe thunderstorms is a

---

S. Verma · M. Cid Montoya  
Texas A&M University-Corpus Christi, Corpus Christi, TX 78412, USA  
e-mail: [sumit.verma@tamucc.edu](mailto:sumit.verma@tamucc.edu)

M. Cid Montoya  
e-mail: [miguel.cidmontoya@tamucc.edu](mailto:miguel.cidmontoya@tamucc.edu)

R. P. Selvam (✉)  
University of Arkansas, Fayetteville, AR 72701, USA  
e-mail: [rps@uark.edu](mailto:rps@uark.edu)

© The Author(s), under exclusive license to Springer Nature Singapore Pte Ltd. 2024  
S. G. Rajasekharan et al. (eds.), *Proceedings of the 9th National Conference on Wind Engineering*, Lecture Notes in Mechanical Engineering,  
[https://doi.org/10.1007/978-981-99-4183-4\\_1](https://doi.org/10.1007/978-981-99-4183-4_1)

cosmopolitan problem and is certainly not confined to a single continent. While the formation of severe convective thunderstorms and tornadoes is beyond our control, the engineering community certainly can contribute to developing a better understanding of the wind loads on structures during tornadic events. But the research efforts to study and better understand the flow characteristics, as well as the imposed wind loads on structures by tornado vortices, are limited to a few prestigious universities in the world (such as Texas Tech University for VorTECH simulator facility, Iowa State University for ISU tornado simulator, Western University for WindEEE dome, Tokyo Polytechnic University to name a few). From a computational perspective, the research on tornado modeling can be traced back to the 1990s by Selvam and his research group [6] at the University of Arkansas. In the recent past few years, more studies based on Computational Fluid Dynamics (CFD) modeling of tornadoes have been carried out [7, 8]. Despite numerous research studies on tornado simulation from both the experimental and computational sides, as mentioned above, the broader fraction of the wind engineering research community still does not have access to the tools and resources necessary to advance the research efforts on tornado simulation and/or wind load quantification on structures due to tornadoes. This is because the access to large-scale experimental tornado simulator facilities is limited only to a few esteemed institutions. On the other hand, the high cost of purchasing a license to operate commercial CFD solvers poses a significant barrier to the research community to advance research effort on tornado modeling and simulation. The authors have pursued tornado modeling along with quantification of wind loads previously using in-house ForTRAN codes [9]. But the inherent challenge with in-house codes is that the users should be able to understand the code base and its control flow to customize and fit it to their own purpose, which is the next step challenge. These challenges can be overcome by leveraging the capabilities of open-source software. This forms the core motivation for this work. Thus, in this contribution, the modeling and simulation of a tornado vortex and its implementation using the open-source software OpenFOAM are discussed. The primary numerical details and some key visualizations, including some experimental comparisons, are covered in this work. In that regard, the geometric idealization of the Texas Tech University tornado simulator is discussed first in Sect. 2. Further details about the application of OpenFOAM for Wind Engineering problems can be obtained from [10].

## 2 Simplified Geometrical Idealization for CFD Simulator

In Fig. 1a, a schematic 3D view of the experimental tornado simulator at Texas Tech University (called VorTECH) is shown, whereas Fig. 1b shows the equivalent CFD model considered for this work. Further details about the geometry of VorTECH simulator can be obtained from [11]. The experimental tornado simulator is octagonal in shape with 8 fans of 1.2192 m (4 ft.) diameter each. The inlet height of experimental tornado simulator is  $h_o = 1$  m, and the updraft radius is  $r_{up} = 2$  m. The aspect ratio of the experimental tornado simulator is thus maintained at aspect ratio ( $a$ ) =  $h_o/$

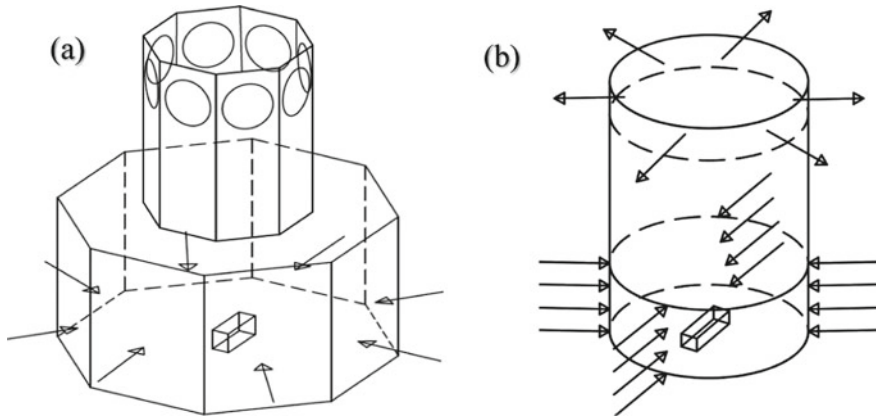


**Fig. 1** Schematic diagram of **a** experimental tornado simulator VorTECH at Texas Tech University and **b** simplified CFD tornado simulator

$r_{up} = 0.5$  (for datasets considered in this work). The total height of the experimental tornado simulator is  $H = 5.96$  m.

To lower high computational demands, some simplifications are applied to the CFD model implemented in this work rather than a full domain geometric modeling of VorTECH facility. Firstly, the octagonal shape of the experimental tornado simulator (with an inscribed circle diameter of 4 m) is approximated with a circular section of a cylinder with the same diameter of 4 m. The inlet height ( $h_o$ ) is kept at 1 m (same as the experimental tornado simulator), and the total height ( $H$ ) is approximated as 6 m. Similarly, the updraft radius ( $r_{up} = 2$  m) for the CFD tornado simulator is kept the same as the experimental tornado simulator. However, the outlet region provided by 8 fans of 1.2192 m diameter each in the experimental tornado simulator is replaced in the CFD tornado simulator by an effective outlet height of 0.743 m (refer Fig. 2). The effective outlet height for the CFD tornado simulator is simply obtained by equating the combined area of the 8 fans of the experimental tornado simulator with the curved surface area of the cylindrical domain at the outlet region as shown in Fig. 1b.

### 3 Mathematical Formulation

#### 3.1 Governing Equations

Flow modeling of the tornado vortex is done using an incompressible Navier–Stokes (NS) equation with LES turbulence model. For sub-grid stress (SGS) modeling, Smagorinsky model is used. The convection term of NS equation is discretized using the central differencing scheme, and the pressure gradient term is approximated by a linear scheme. The solution advances in time using a pure Crank-Nicolson scheme.



The diffusion term (involving the Laplacian operator) is discretized using a central difference scheme. The governing equations for the spatially filtered incompressible Newtonian fluid chosen for this work are given in vectorial form as follows:

$$\nabla \cdot \tilde{\mathbf{u}} = 0 \quad (1)$$

$$\frac{\partial \tilde{\mathbf{u}}}{\partial t} + \nabla \cdot (\tilde{\mathbf{u}}\tilde{\mathbf{u}}) = -\nabla \tilde{p} + (\nu + \nu_{\text{sgs}})\nabla^2 \tilde{\mathbf{u}} \quad (2)$$

$$\nu_{\text{sgs}} = C_k \Delta k^{0.5} \quad (3)$$

In Eq. (2), the term ' $\nu_{\text{sgs}}$ ' is called the turbulent kinematic viscosity and is defined by Eq. (3). Further numerical details can be obtained from [12]. In this work, the non-dimensional form of NS equation is used. The reference values considered for non-dimensionalization of the NS equation are (a) radius ( $r_{\text{up}}$ ) for length scale and (b) radial velocity at inlet height ( $V_{\text{ro}}$ ) for velocity.

### 3.2 Boundary Conditions

A logarithmic velocity profile is used to model the inlet velocities in  $X$  and  $Y$  directions for the tornado simulator, while the vertical velocity component is considered zero throughout the inlet height. The maximum non-dimensional radial velocity is taken as  $V_r(z = h_o) = V_{\text{ro}} = 1$ , and the corresponding tangential component is designated as  $V_{\text{to}}$ . The distribution of radial velocity from the base of tornado simulator up to the inlet height is expressed as a function of elevation and is given as

$$V_r(z) = C_1 \ln\left(\frac{z + z_o}{z_o}\right) = C_1 \ln\left(1 + \frac{z}{z_o}\right) \quad (4)$$

The swirl ratio ( $S$ ) for flow is calculated by Eq. (5).

$$S = \frac{V_{\text{to}}}{2\left(\frac{h_o}{r_{\text{up}}}\right)V_{\text{ro}}} \quad (5)$$

Using the definition of ' $S$ ', the tangential component of velocity is computed as

$$V_t(z) = 2V_r(z)S\left(\frac{h_o}{r_{\text{up}}}\right) \quad (6)$$

Now, the velocity components in the radial and tangential direction defined above are resolved in the  $X$ - and  $Y$ -direction to be provided as the boundary condition for the inlet velocity since the computational domain (cylinder) is based on Cartesian

grid system. In this work, a tornado vortex rotating in anticlockwise direction is assumed. The radial and tangential velocity components are decomposed into their constituent  $x$ -component and  $y$ -component locally with respect to the direction ( $\alpha$ ), as shown in Fig. 3. Here, the angle is always measured in the anticlockwise direction from the local  $X$ -direction up to the direction of radial velocity component at the point of interest ( $P$ ) (refer Fig. 3). For instance, in Fig. 3, the value of angle ' $\alpha$ ' is  $(\pi + \tan^{-1} \frac{y}{x})$  radians for any generic point in the first quadrant in which ' $x$ ' and ' $y$ ' are the  $x$ -coordinate and  $y$ -coordinate of point  $P$ , respectively. For the 1st quadrant, the limits for the quadrant angle ' $\theta$ ' is given by  $(0 \leq \theta \leq \pi/2)$  radians. Now, if the radial and tangential velocity components are decomposed in the local  $X$ -direction and  $Y$ -direction, then the effective velocity component in the  $X$ -direction and  $Y$ -direction are obtained as follows:

$$\begin{aligned}
 X \text{ - dir. : } & V_r \cos(\alpha) + V_t \cos(\alpha - \pi/2); \\
 Y \text{ - dir. : } & V_r \sin(\alpha) + V_t \sin(\alpha - \pi/2).
 \end{aligned}$$

The boundary conditions imposed on the cylindrical domain to develop tornado flow are summarized in Table 1. Further details about the velocity boundary condition applied at the inlet can be obtained from [12]. The roughness parameters considered in the model are  $z_o = 0.00004h_o$  and  $C_1 = 0.0924V_{10}$ . The Reynolds number considered for flow computation is  $5.51 \times 10^5$ , which is calculated at the inlet height ( $h_o$ ) of the tornado simulator. The elevation and plan of the mesh for the cylindrical computational domain are shown in Fig. 4a, b, respectively, and it consists of 540,000 hexahedral cells.

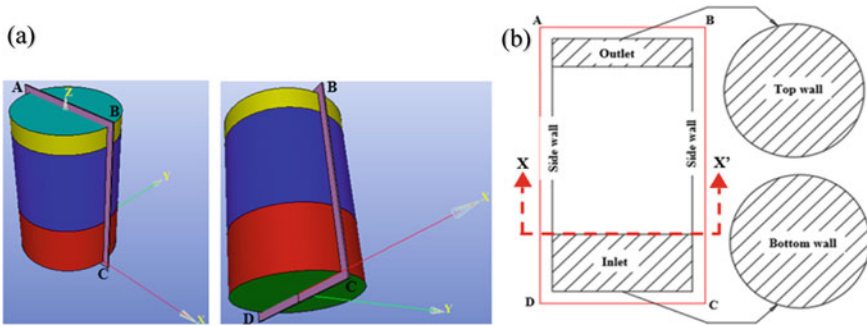


**Fig. 2** a 3D view of cylindrical domain showing different boundary faces and **b** sectional view through plane ABCD showing different boundaries of the computational domain

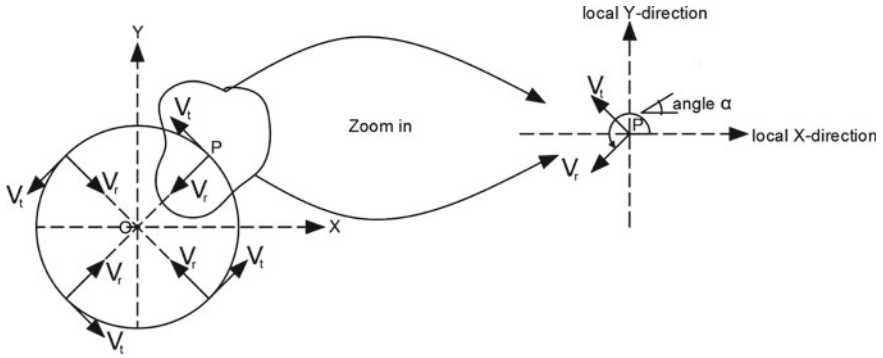


**Fig. 3** Top view for transverse section at  $X - X'$  showing velocity boundary condition at inlet height

**Table 1** Description of boundary faces, types, and boundary conditions for different faces in computational domain

S. No.	Boundary name	BC type	Color coding	BC in mathematical form
1	Inlet	Patch	Red	$\partial p / \partial n = 0$ ; For velocity refer [12]
2	Bottom wall	Wall	Green	$u = v = w = 0$ ; $\partial p / \partial n = 0$
3	Side wall	Wall	Blue	$u = v = w = 0$ ; $\partial p / \partial n = 0$
4	Outlet	Patch	Yellow	$p = 0$ ; $\partial u / \partial n = \partial v / \partial n = \partial w / \partial n = 0$
5	Top wall	Wall	Cyan	$u = v = w = 0$ ; $\partial p / \partial n = 0$

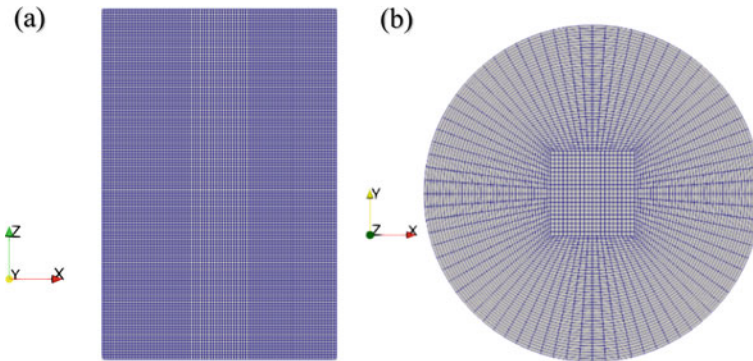


**Fig. 4** Mesh for the computational domain **a** vertical section through the diametric axis showing elevation and **b** horizontal section showing plan of the domain

## 4 Results and Experimental Comparison

Since the Reynolds number of the flow is very high at  $Re = 5.51 \times 10^5$ , thus, the flow is in a turbulent state, and so the flow properties change from one time instant to another. Since turbulent flows are commonly described in terms of flow statistics, an attempt is made to track the pressure and velocity close to the ground surface at four different points, viz. probe '0,' '1,' '2,' and '3.' The coordinates of each of the probes is shown in Fig. 5. In Fig. 5a, it can be observed that the pressure at probes 1, 2, and 3 have attained a relatively steady state as the perturbation in the magnitude is very low. The pressure at location of probe 0, however, shows a relatively larger amplitude of perturbation compared to the other probes. Similarly, the temporal variation of velocity components at the location of probe 0 is shown in Fig. 5b, which on account of low perturbations, and periodicity indicates that the flow has attained a statistically steady state. The instantaneous and the mean tangential velocity profile for  $S = 0.36$  and  $S = 0.83$  is included in Fig. 6a, whereas the corresponding pressure profiles are shown in Fig. 6b. In addition, the experimental pressure profile for  $S = 0.83$  is also included in Fig. 6b. Using normalized root mean square as the error estimate, the deviation between the experimental TTU profile and the mean pressure profile at  $S = 0.83$  is found to be about 11%. A more refined mesh would be helpful to minimize the error furthermore.

The experimental pressure profile for  $S = 0.83$  in Fig. 6b is based on the datasets from Texas Tech University (Tang, Z., Zuo, D., private communication, August 14, 2021). In Fig. 7, the mean flow field for  $S = 0.36$  and  $S = 0.83$  is compared to demonstrate the evolution of vortex in the simulator. At  $S = 0.36$ , the vortex breakdown aloft of the simulator can be observed (shown in Fig. 7a by downward pointing vectors) indicating the phase of vortex approaching touchdown, whereas the flow at  $S = 0.83$  indicates a vortex beyond touchdown with the downdraft component touching the base of simulator. These observations are in close agreement with experimental VorTECH simulator datasets.

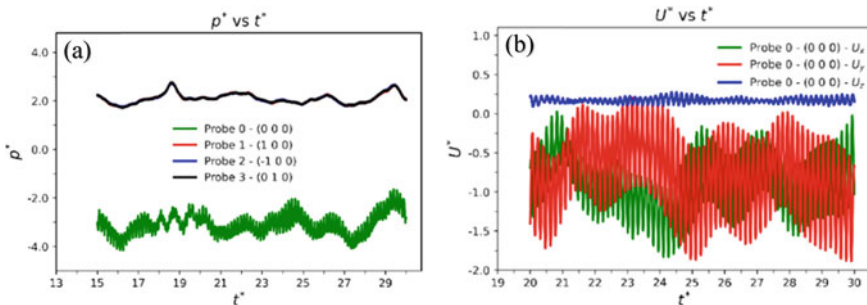


**Fig. 5** Time series plot of **a** non-dimensional pressure and **b** non-dimensional velocity close to the bottom center of CFD simulator with respect to non-dimensional time ( $t^*$ ) for  $S = 0.36$

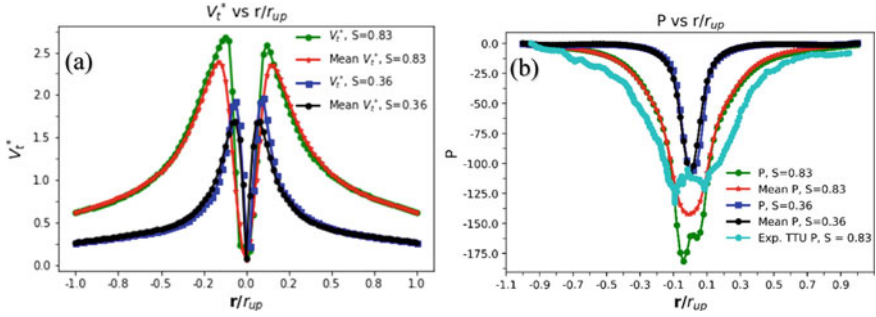


**Fig. 6** Mean profiles at the bottom of tornado simulator **a** tangential velocity profile at  $z/r_{up} = 0.05$  and **b** pressure profile at  $z/r_{up} = 0.0$  for  $S = 0.36$  and  $S = 0.83$

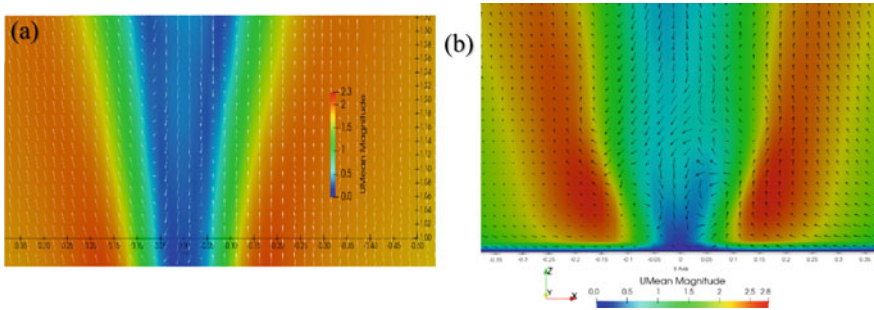


**Fig. 7** Contour plot of mean velocity magnitude with velocity vectors in the background through the diametric  $XZ$ -plane of CFD tornado simulator **a**  $S = 0.36$ , **b**  $S = 0.83$

## 5 Conclusion

The key numerical implementation details of a simple tornado simulator using open-source software OpenFOAM is discussed in this work. The computed flow field is compared with experimental measurements both qualitatively and quantitatively. Results show that the flow field for  $S = 0.36$  indicates the state of vortex breakdown aloft approaching the stage of touchdown, whereas that for  $S = 0.83$ , a vortex in the post-touchdown phase is observed. On a qualitative basis, these observations from the CFD simulator model agree very well with the observations of the experimental TTU tornado simulator, in which a double-celled tornado vortex is obtained for  $S = 0.83$ . On a quantitative basis, the deviation between the mean pressure profile and the experimental TTU pressure profile is found to be around 11%, which can be further minimized using a refined grid. Thus, it is concluded that the model can provide a reasonable prediction of the evolution of the vortex as well as the pressure field, as indicated by the qualitative and quantitative analysis of the datasets obtained from CFD simulation.

**Acknowledgements** The first and the second author acknowledge the support received from National Science Foundation (NSF), USA, under award no. CMMI-1762999.

## References

1. Changnon SA (2009) Tornado losses in the United States. *Nat Hazards Rev* 10(4):145–150. [https://doi.org/10.1061/\(ASCE\)1527-6988\(2009\)10:4\(145\)](https://doi.org/10.1061/(ASCE)1527-6988(2009)10:4(145))
2. Sills DML, Kopp GA, Elliott L et al (2020) The Northern Tornadoes project: uncovering Canada’s true tornado climatology. *Bull Am Meteor Soc* 101(12):E2113–E2132. <https://doi.org/10.1175/BAMS-D-20-0012.1>
3. Yao Y, Yu X, Zhang Y et al (2015) Climate analysis of tornadoes in China. *J Meteorol Res* 29:359–369. <https://doi.org/10.1007/s13351-015-4983-0>
4. Grieser J, Haines P (2020) Tornado risk climatology in Europe. *Atmosphere* 11(7):768. <https://doi.org/10.3390/atmos11070768>
5. Akter N, Rafiuddin M (2022) Outbreak of a Tornado with tropical cyclone Yaas (2021) formed over the Bay of Bengal. *Asia-Pacific J Atmospheric Sci*. ISBN/ISSN: 1976-7951. <https://doi.org/10.1007/s13143-022-00302-4>
6. Selvam RP, Millett PC (2003) Computer modeling of tornado forces on buildings. *Wind Struct* 6:209–220. <https://doi.org/10.12989/was.2003.6.3.209>
7. Liu Z, Ishihara T (2015) Numerical study of turbulent flow fields and the similarity of tornado vortices using large-eddy simulations. *J Wind Eng Ind Aerodyn* 145:42–60. <https://doi.org/10.1016/j.jweia.2015.05.008>
8. Yuan F, Yan G, Honerkamp R, Kakkattukuzhy MI, Zhao M, Mao X (2019) Numerical simulation of laboratory tornado simulator that can produce translating tornado-like wind flow. *J Wind Eng Industr Aerodyn* 190:200–217. <https://doi.org/10.1016/j.jweia.2019.05.001>
9. Verma S, Selvam RP, Tang Z, Zuo D (2022) Comparison of Tornado-induced pressures on building from CFD model with TTU experimental measurements. *J Wind Eng Ind Aerodyn* 228:105076. <https://doi.org/10.1016/j.jweia.2022.105076>
10. Selvam RP (2022) *Computational fluid dynamics for wind engineering*. Wiley
11. Tang Z, Zuo D, James D, Eguchi Y, Hattori Y (2018) Effects of aspect ratio on laboratory simulation of tornado-like vortices. *Wind Struct* 27(2):111–121. <https://doi.org/10.12989/was.2018.27.2.111>
12. Verma S (2022) Validation of CFD Tornado pressure on building and wind field with TTU vortex chamber measurements, Ph.D. Dissertation, University of Arkansas, USA. <https://scholarworks.uark.edu/etd/4516/>

# Construction and Calibration of a Low-Speed Variable Velocity Profile Wind Tunnel



Kalyani Panigrahi , Rohan Bhattacharya , Garima Singh ,  
K. Supradeepan , Sabareesh Geetha Rajasekharan ,  
and P. S. Gurugubelli 

**Abstract** Wind tunnel experimentations have played a vital role in determining the aerodynamic loads for the design of aircrafts, tall buildings, bridges, etc. With the advent of unmanned and autonomous flying devices, the role of wind tunnel testing becomes even more critical. The role will now not only include determining the aerodynamic loads but also testing the autonomous capabilities and the ability of the autonomous flying device to react to the changes in wind speeds and directions. The objective of the current work will be is to construct and calibrate one such low-speed wind tunnel that will have capability to generate different wind velocity profiles along with gust. The test section of the wind tunnel will of a cross-sectional size  $1.2\text{ m} \times 1.2\text{ m}$  and  $2.4\text{ m}$  long. The wind flow through the test section will be powered by a grid of  $10 \times 10$  DC fans, each having a capacity of 250 CFM.

**Keywords** Low-speed wind tunnel · Turbulence intensity · Variable velocity profile

## 1 Introduction

To investigate the interaction between air and aerial bodies, experimental facilities known as wind tunnels are put into use to determine the aerodynamic forces and corresponding aeroelastic responses. In a wind tunnel, air is passed over the body of interest mounted on multi-axis load-cells to simulate the aerodynamic effects during a flight. In addition to aerodynamic forces, wind tunnels are also primarily used for visualizing the fluid flow over an aerial body. There are several ways to visualize the airflow, one of the most common methods is to introduce smoke or dye in the flow field and observe how it moves around the object. The air flow over the body

---

K. Panigrahi (✉) · R. Bhattacharya · G. Singh · K. Supradeepan · S. G. Rajasekharan · P. S. Gurugubelli  
Bits-Pilani Hyderabad, Secunderabad, Telangana 500078, India  
e-mail: [p20190445@hyderabad.bits-pilani.ac.in](mailto:p20190445@hyderabad.bits-pilani.ac.in)

© The Author(s), under exclusive license to Springer Nature Singapore Pte Ltd. 2024  
S. G. Rajasekharan et al. (eds.), *Proceedings of the 9th National Conference on Wind Engineering*, Lecture Notes in Mechanical Engineering,  
[https://doi.org/10.1007/978-981-99-4183-4\\_2](https://doi.org/10.1007/978-981-99-4183-4_2)

is characterized by quantifying the variation of the air pressure along the body with the aid of a series of pressure taps connected to a multi-channel pressure scanner. Just like any other experimental facility, wind tunnels also come in various sizes and types depending on the nature of the wind speed profile, wind speeds, scale of the body that needs to be investigated, desired turbulence intensity, and the operational efficiency based on the power consumption.

Unsteady flows are part of most aerodynamic applications and are known to play a significant role in understanding the aeroelastic stability of wing structures, for example wind-aileron stability and helicopter blade flutter. It is also essential in estimating the time-dependent loads acting on the slender wing structures of an aircraft performing complex maneuvers, since the peak unsteady aerodynamic loads during the maneuvering will be distinctly different from the loads acting on the wing during cruise flight. As a result low-speed unsteady aerodynamics has recently attracted increased attention. Additionally, unsteady aerodynamics also play a critical role in wind turbine for example the blades of a horizontal-axis wind turbine are subjected to unsteady flows due to gusts and yaw that would result in dynamic stall which are challenging to model. Similarly, vertical-axis wind turbine blades are particularly prone to dynamic stall due to their innately unstable fluctuations in velocity direction and magnitude. MAVs, on the other hand, are incredibly susceptible to abrupt load changes from gusts because of their slow flying speeds, which can significantly affect their aerodynamic behavior. Thus, unsteady low-speed wind tunnels are once again getting prominence due to these issues.

In a recent paper, the theory of unsteady low-speed wind tunnels with blowdown configuration was presented, wherein it was found that by linearizing the governing equations, the wind tunnel frequency bandwidth is proportional to the mean tunnel velocity and inversely related to the test-section length [1]. In another work, an Unsteady Aerodynamics Experiment (UAE) was designed to get precise quantitative measurements of the aerodynamics and structural properties of a wind turbine that was both geometrically and dynamically typical of full-scale devices [2]. Similar to this, a unique low-speed wind tunnel creating erratic “gust” flows was constructed. To compare results with predictions from thin aero foil theory, this tunnel was suitable for testing individual aero foils and aero foils in cascade in non-convective gusts [3].

More recently two novel test methodologies—a forced vibration test technique and a hybrid aero elastic-force balance wind tunnel test methodology—are presented in [4] to determine the unsteady aerodynamic loads acting on a bluff body.

Recent researches also show designing and construction of Fan Array Wind Tunnels (FAWT). An array of  $10 \times 10$  fans was considered by [5], to study the flapping dynamics of an inverted flag and found that due to unsteady fluid force, there is an improvement in the conversion of fluid kinetic energy into elastic strain energy. Another team of researchers [6] focused on developing unconventional flow conditions such as turbulence and gust inside a multi-fan wind tunnel, by simulating these flow conditions using iterative-based methods. In another work, the (Cross Axis Wind Turbine) CAWT’s static and dynamic performances in steady/unsteady wind conditions at different Reynolds numbers are tested [7]. An investigation was



conducted on the impact of mismatching turbulence spectra on the unsteady wind loads in wind tunnel modeling of small-scale structures [8].

To predict and understand the unsteady flow dynamics in a new light certain mathematical models were also designed such as a one-dimensional, incompressible control volume analysis was used to create a simple predictive mathematical model that successfully captured the unstable operation of the open-return wind tunnel facility and can be utilized to deterministically create louver motions that result in innovative, erratic test section speed profiles by taking into account the dynamic reaction of the wind tunnel [9]. Another study related to the louver motions involved an experimentally proven method-of-characteristics modeling technique used to investigate the dynamic behavior of a low-speed closed-circuit wind tunnel in response to dynamic louver excitation [10].

The objective of this work includes the construction of a low-speed wind tunnel that have the capability to actively control the velocity profile of the air inside the test section using a framework of 100 DC fans and calibrating the tunnel by studying various parameters such as mean velocity and turbulence intensity (TI) of flow at various locations inside the 2.4-m-long tunnel, thereby evaluating the flow characteristics inside the tunnel.

## 2 Experimental Setup and Methodology

The variable velocity profile wind tunnel facility based on FAWT concept is constructed using 100 Nos. of DC powered fans that are arranged in the form of a grided array consisting of 10 rows and 10 columns (Fig. 1). The fans used here are Hicool DC Compact Fans operating at 0.9 A at 48 V, having a maximum input power of 43.2 W. Each fan covers an area of 14400 mm<sup>2</sup>. The electrical connections are made such that each row of fans is regulated by two switched mode power supply (SMPS) in an alternate arrangement.

The test section is square shaped having an area of  $1.2 \times 1.2$  m<sup>2</sup> and 2.4 m in length. The row of fans starting from the bottom is labeled as Row 1 with the topmost row of fans being labeled as Row 10. The electrical configuration and layout are particularly nexus, as each fan of each row are made to be individually controlled, also at the same time, it should be flexible enough to detect which of the fan is not in proper working condition while operating a set of fans at the same time for creating different patterns of velocity profiles inside the tunnel.

## 3 Calibration Process-Performance Characterization

To investigate the flow characteristics inside the tunnel, certain parameters evaluating the performance of the wind tunnel is considered. Five different locations located at different distances from the fan framework, along the centerline of the tunnel

are considered. The TI and mean velocities along the length of the tunnel are estimated using a fiber-probe Hot-Wire Anemometer (HWA). The HWA is a Constant Temperature Type Anemometer (CTA) (Made-Dantec Dynamics) which consists of a heated fiber-probe, maintaining a constant temperature while the air passes through it, thereby generating a certain voltage. These voltages can be co-related to wind velocities inside the tunnel, further calculating the mean velocities and turbulent fluctuations at different locations of the tunnel. The fiber-probe is connected to a 4-m-long BNC cable and a Dantec Dynamics adaptor which fulfills the power requirements of the probe. The adaptor is connected to a NI-9215 C-series 4 channel analog input module, having a sampling rate of 100 ks/s/channel. This NI module is used for data acquisition.

The locations chosen are at a distance of 75 cm, 100 cm, 125 cm, 150 cm, 175 cm from the fans, respectively, the HWA is placed at each of these positions, and the mean velocity and TI % at each of these points is evaluated. At each point, the duty cycle is varied from 10 to 100% keeping the frequency of the fan constant, the mean velocity and TI is calculated based on the velocity values obtained at various distances. Each run is repeated 5 times at each location to ensure repeatability.

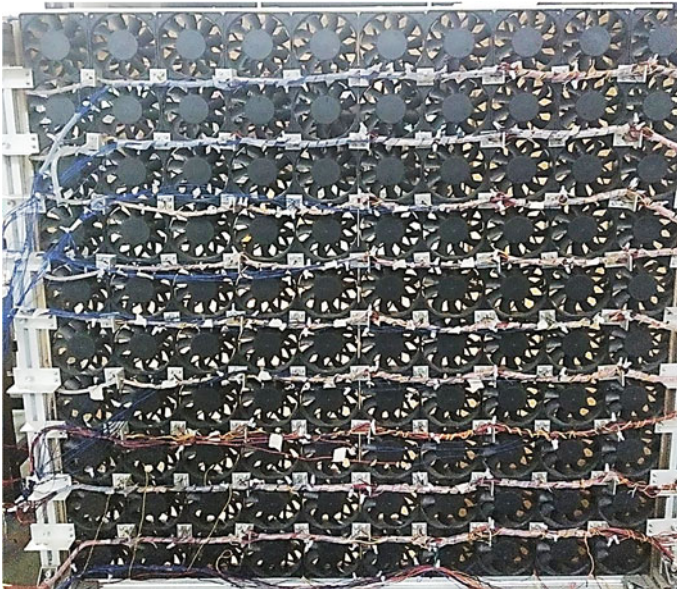


**Fig. 1** Front view of the 10x10 DC fan array grid

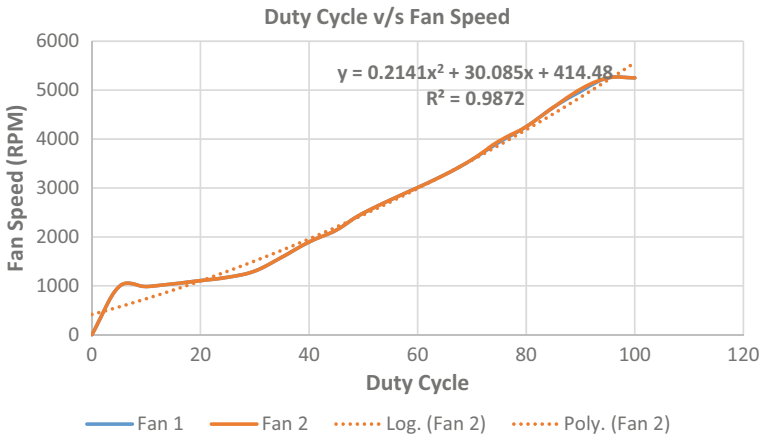


Fig. 2 Graph depicting the duty cycle versus speed of fans

## 4 Results and Discussions

### 4.1 Initial Testing of Modules and Fans

The speed of the fan can be controlled by either varying the duty cycle or by varying the frequency in the PWM circuit. Therefore, to establish the relationship between the duty cycle and the speed of the fan, the duty cycle of a single fan was varied from 0 to 100%, and the corresponding speed is measured by utilizing a stroboscope. Figure 2 depicts the varying fan speed, while the duty cycle of the fans is regulated and controlled by an Arduino board. As can be seen from the figure, there exists an almost linear relationship between the two parameters. As the duty cycle is increased, the speed of the fan (measured in RPM) also increases.

### 4.2 Turbulence Intensity and Mean Velocity Calculations

The measure of turbulence characteristics pertaining to the flow conditions inside the tunnel can be quantitatively estimated by calculating the turbulence intensity (TI) at various locations inside the tunnel. The TI presents a numerical estimation of the fluctuating components of the velocity at various flow conditions with the sensor capturing the fluctuations positioned at different coordinates inside the tunnel. A Hot-Wire Anemometer (HWA) is used to capture the turbulent fluctuations inside the tunnel. An NI-DAQ device is connected to the HWA that is used for data acquisition. The data acquired is used to calculate the mean velocities at each of these locations inside the tunnel. The HWA is placed various distances from the fan framework. A total of 5 distances is considered along the central axis of the tunnel ranging from

75 to 175 cm. Figure 3 represents the variation of the mean velocity taken at a single point with the sensor placed at a specific distance from the framework of the 100 DC fans with the duty cycle varying from 10 to 100% keeping the frequency of fan constant at 25 kHz. The above figure shows similar trends for the mean velocities measured at all 5 distances. Initially, it increases as the duty cycle is increased from 10 to 20%, with a slight decrease as the duty cycle is increased to 30%, as the duty cycle is further increased the values shows an upward trend with a gradual increase in the mean velocity. Beyond the 70% duty cycle, the values tend to converge onto one another, and an overlapping of the graphs can be observed which indicates that the mean velocities lies at a very close range to each other pertaining to various distances from the fan framework, signifying that the distance from the fans does not affect the mean velocities to a greater extent beyond the 70% duty cycle.

Figure 4 depicts the change in the turbulent fluctuation denoted by the TI % as the duty cycle increases while placing the sensor along the central axis of the tunnel, at 5 different distances from the framework of the fans. From the figure, it can be clearly observed that the TI follows a similar trend at each of the locations. Initially, at lower duty cycles, the graphs overlap over each other displaying a close range of TI varying from 30 to 35%. As the duty cycle is further increased from 20 to 50%, a gradual decrease in the TI can be observed; as the cycle progresses beyond 50%, the TI is decreasing more showing the lowest TI of 5.567%, also it is observed that as the distances from the fans increases, the lowest TI along higher duty cycles also keeps on decreasing, signifying the fact that the farther the position of the sensor from the fans, the lower is the TI.

The trends observed here are in accordance with a recent work performed by Dougherty [11], which involved the construction of a Fan Array Wind Tunnel, and similar tests were performed to analyze the effect of geometry on the developing

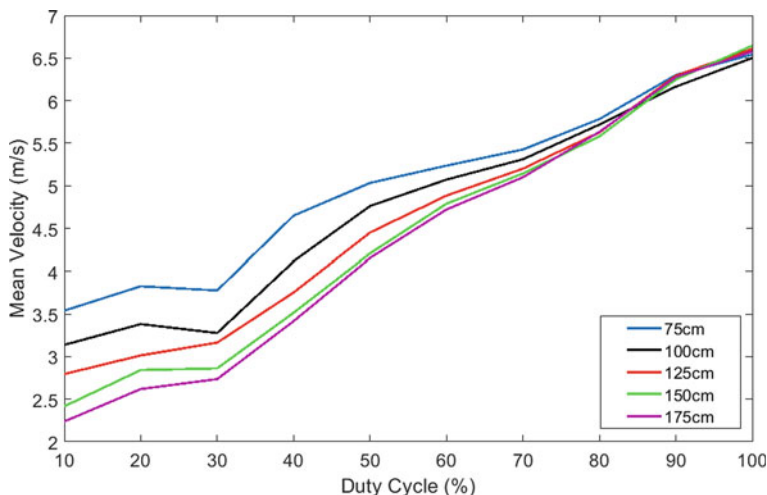
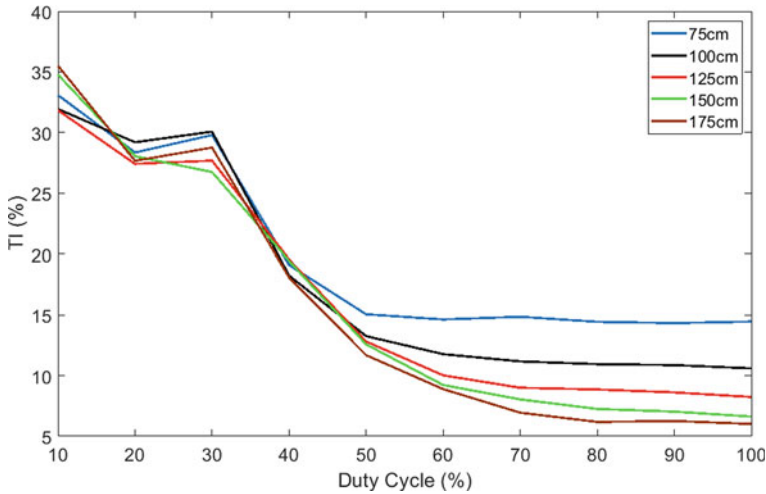


Fig. 3 Variation of mean velocity w.r.t. duty cycle at various distances from the fan framework



**Fig. 4** TI variation along the duty cycles at different distances from the fan framework

flow conditions inside the tunnel. Each array is comprised of  $11 \times 22$  fans; 4 arrays of the aforementioned dimension were combined in various configurations and the flow conditions inside the tunnel were studied. They studied the measured values of turbulence intensity (%) and the non-dimensional free stream velocity, at different measurement locations inside the tunnel.

## References

- Greenblatt D (2016) Unsteady low-speed wind tunnels. *J AIAA* 54(6):1817–1830
- Hand MM, Simms DA, Fingersh LJ, Jager DW, Cotrell JR, Schreck S, Larwood SM (2001) Unsteady aerodynamics experiment phase VI: wind tunnel test configurations and available data campaigns. United States
- Horlock J (1974) An unsteady flow wind tunnel. *J Aeronaut Q* 25(2):81–90
- Chen Z, Xu Y, Huang H, Tse KT (2020) Wind tunnel measurement systems for unsteady aerodynamic forces on bluff bodies: review and new perspective. *J Sens* 20
- Kim D, Cossé J, Cerdeira CH, Gharib M (2013) Flapping dynamics of an inverted flag. *J Fluid Mech* 736:R1. <https://doi.org/10.1017/jfm.2013.555>
- Cui W, Zhao L, Cao S, Ge Y (2021) Generating unconventional wind flow in an actively controlled multi-fan wind tunnel. *Wind Struct* 33(2):115–122
- Wang WC, Wang JJ, Chong WT (2019) The effects of unsteady wind on the performances of a newly developed cross-axis wind turbine. *J Renew Energy* 131:644–659
- Jafari A, Ghanadi F, Emes MJ, Arjomandi M, Cazzolato BS (2019) Measurement of unsteady wind loads in a wind tunnel: Scaling of turbulence spectra. *J Wind Eng Industr Aerodyn* 193
- Farnsworth J, Sinner D, Gloutak D et al (2020) Design and qualification of an unsteady low-speed wind tunnel with an upstream louver system. *Exp Fluids* 61(181)
- Rennie RM, Catron B, Feroz MZ, Williams D, He X (2019) Dynamic behavior and gust simulation in an unsteady flow wind tunnel. *J AIAA* 57(4):1423–1433

11. Dougherty C, Veismann M, Stefan-Zavala A, Renn P, Gharib M. The design and characterization of fan array wind tunnels. Appendix A, [thesis.library.caltech.edu](https://thesis.library.caltech.edu)

# Aerodynamic Characteristics of an Inclined Square Cylinder with Corner Fins



D. Amith, C. Sarath Mohan, C. M. Hariprasad, and R. Ajith Kumar

**Abstract** Flow around a square cylinder with corner fins was studied to investigate the aerodynamic characteristics of the same at different angles of attack. This study simulates flow around typical building structures employed in practical situations. Flow was studied in a flow visualization water channel at a Reynolds number of 2100 with blockage ratio less than 10%. In this study, vortex formation length and vortex shedding frequency are primarily measured for various cases. From these two parameters, other aerodynamic parameters such as coefficient of base pressure, coefficient of drag, circulation content of a shed vortex, and total circulation shed at the separation point are deduced. It is found that corner fin considerably modifies the flow field of a square cylinder. Furthermore, body angle of inclination brings additional changes in the flow structures around it and in the associated aerodynamic characteristics.

**Keywords** Square cylinder · Corner fins · Angle of inclination · Aerodynamic characteristics

## 1 Introduction

Wind-induced vibration is a major factor influencing the stability of high-rise buildings, and it is therefore considered in structural designs. Bluff bodies with different aerodynamic modifications have been studied over the past many years because of its practical importance in increasing structural stability. Several studies have been done so far focusing on aerodynamic modifications to reduce wind-induced vibrations to ensure structural safety. Studies conducted by [1, 9, 19, 22, 23, 26] reveal

---

D. Amith · C. Sarath Mohan · C. M. Hariprasad · R. Ajith Kumar (✉)  
Department of Mechanical Engineering, Amrita Vishwa Vidyapeetham Amritapuri, Clappana,  
India  
e-mail: [amritanjali.ajith@gmail.com](mailto:amritanjali.ajith@gmail.com)

D. Amith  
e-mail: [amith.dinesh469@gmail.com](mailto:amith.dinesh469@gmail.com)

© The Author(s), under exclusive license to Springer Nature Singapore Pte Ltd. 2024  
S. G. Rajasekharan et al. (eds.), *Proceedings of the 9th National Conference on Wind Engineering*, Lecture Notes in Mechanical Engineering,  
[https://doi.org/10.1007/978-981-99-4183-4\\_3](https://doi.org/10.1007/978-981-99-4183-4_3)

insightful results on flow past a square cylinder. Different studies have been done on sharp-edged structures (square and rectangular cross sections) with different corner modifications. The slotted corners, chamfered corners, and combinations thereof cause significant modifications in both the along-wind and crosswind responses [15]. Kawai [13] has shown that aeroelastic instability can be prevented by using a small recession and corner cut on square sections. Not only the corner modifications, but also the aerodynamic characteristics of a square section cylinder significantly vary at different angles of attack [25]. Along with Strouhal number and drag variations, the near wake structures too undergo notable changes due to different corner modifications. This was typically observed in the studies conducted by [3, 8, 19]. Du et al. [10] compared modified square cylinders with sharp/round corners and straight/concave/convex sides. Their study shows that aerodynamic characteristics and flow regimes vary with these modifications. The influence of dissimilar leading edges in stationary and oscillating square cylinders on their flow structures have been studied by [2, 4]. Kwok and Bailey [16] identified that vented fins or small fins attached to a square structure shows an increase in the along-wind response. Wang et al. [24] found that corner fins (fin angle  $45^\circ$  at flow angle of inclination  $0^\circ$ ) have a significant impact on aerodynamic characteristics. The introduction of fins in long bridges and tall buildings has shown to reduce the wind-induced vibrations of the structure, yet there are also studies where the vibration is enhanced using minor modification for energy harvesting [11].

It is evident from the existing literatures that there is scope for more investigations on square section cylinders with corners fitted with fins. Realizing this potential research gap, in this investigation, square cylinder is modified with leading-edge fins of  $l/b = 0.5$  at an angle of  $30^\circ$  (Fig. 2). The influence of this corner modification on the aerodynamic characteristics at various angles of inclination, viz.  $0^\circ$ ,  $30^\circ$ ,  $60^\circ$ , and  $90^\circ$ , is examined in this paper.

## 2 Experimental Setup

All the experiments were conducted in recirculating flow visualization water channel. This is essentially the same as that used by [4, 8]. Therefore, for details, authors are referred to [4, 8].

The model used here is a square section cylinder with leading-edge fins at an angle of  $30^\circ$  (Fig. 1). The square section has a dimension of  $20 \times 20$  mm with a fin length of 10 mm at an angle  $\alpha = 30^\circ$ . Reynolds number (based on  $D$ ) for this study is 2100. The velocity of flow has been adjusted to attain  $Re = 2100$  for all angles of inclination. The flow direction in the snapshots provided here is from left to right. Flow visualization videos were taken using a high-definition camera (Sony alpha 6) at 50 frames per second.



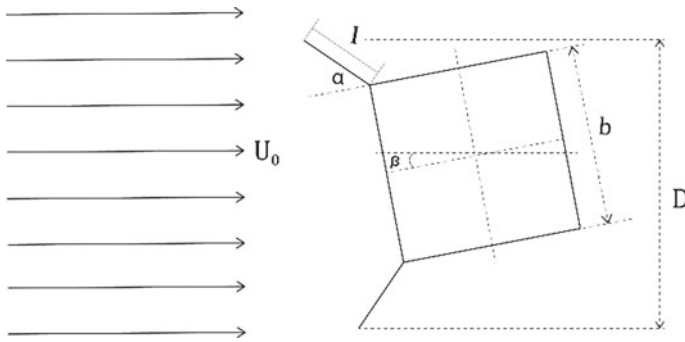
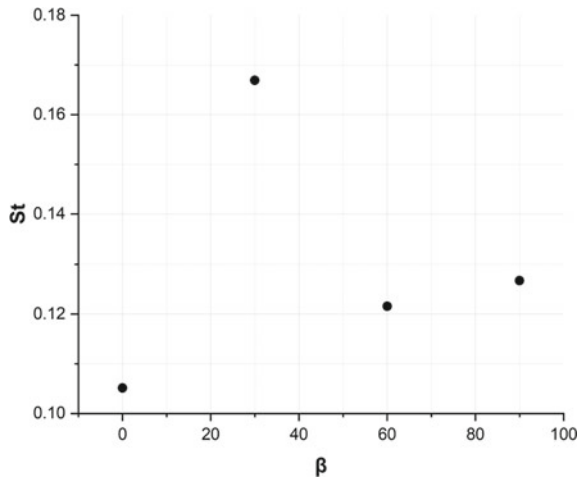


Fig. 1 Experimental model

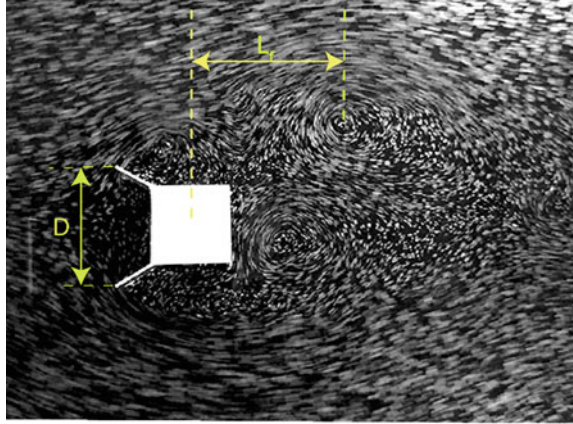
Fig. 2 Variation of Strouhal number with angle ( $\beta$ )



### 3 Results and Discussion

In this section, the results obtained from the experiments conducted on the square cylinders with leading-edge fin at an angle of  $30^\circ$  for four different angles of incidence, viz.  $0^\circ$ ,  $30^\circ$ ,  $60^\circ$ , and  $90^\circ$  are presented. It also discusses their aerodynamic characteristics such as Strouhal number, coefficient of base pressure, coefficient of drag and circulations. The flow field of the models was analyzed from videos captured from the water channel. The results have been compared with aerodynamic characteristics of a square cylinder without corner modification at  $0^\circ$  angle of inclination for the same Reynolds number.

**Fig. 3** Measurement of vortex formation length



### 3.1 Strouhal Number

The vortex shedding frequency ( $f_0$ ) of the models was calculated at  $Re = 2100$ . Initially, the time taken for shedding 10 vortices from the upper shear layer as well as lower shear layer was observed, from which the Strouhal number was calculated as

$$St = \frac{f_0 \cdot D}{U_0} \quad (1)$$

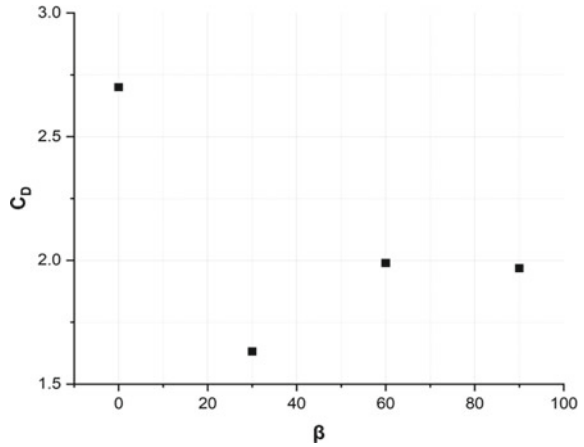
where  $U_0$  is the free stream velocity. The calculated values of the Strouhal number are presented here.

Figure 2 shows the variation of Strouhal number against different angles of inclination ( $\beta$ ) of the models, i.e., 0, 30, 60, and 90°. As seen in Fig. 2, the Strouhal number versus  $\beta$  does not follow a linear trend. A sudden increase in the value of the Strouhal number has been observed for  $\beta = 30^\circ$ , followed by a decrease at  $\beta = 60^\circ$ , and then a subsequent slight increase at  $\beta = 90^\circ$ .

### 3.2 Vortex Formation Length and Coefficient of Drag

The vortex formation length ( $L_f$ ) has been measured from the center of the model to the centerline of the completely formed vortex following [14]. It is then non-dimensionalized with respect to the characteristic dimension ( $D$ ) of the respective geometry. Non-dimensionalized vortex formation length ( $l_f$ ) has been estimated for all the different configurations. A typical measure of vortex formation length is shown in Fig. 3.

**Fig. 4** Variation of coefficient of drag with angle ( $\beta$ )



The base pressure coefficient ( $C_{pb}$ ) is calculated from vortex formation length and empirical constant  $C$  (Eq. 2), where  $C$  varies from 1.6 to 1.8 in the Reynolds number range 1000–9000. In this experiment for  $Re = 2100$ , it is found that  $C = 1.627$  through interpolation.

$$l_f = \frac{C}{-C_{pb}} \quad (2)$$

The coefficient of drag ( $C_D$ ) has been found using the mathematical relation proposed by [5],

$$C_D \cdot St = (0.4777 \cdot K) - 0.45167 \quad (3)$$

$$K = \sqrt{1 - C_{pb}} \quad (4)$$

The  $C_D$  values with respect to different angle of inclination ( $\beta$ ) is plotted in Fig. 4. As Fig. 4 shows,  $C_D$  trend undergoes a ‘dip’ at  $\beta = 30^\circ$  further to which it increases.

### 3.3 Vortex Size

The vortex size is measured from the photographs taken of the fully formed vortices. Most of the vortices appeared nearly elliptical in shape. The vortex size is measured as the average of the major and minor axes of the vortices. It is then non-dimensionalized with respect to the characteristic dimension ( $D$ ). Measurement of vortex size is shown in Fig. 5.

**Fig. 5** Measurement of vortex size

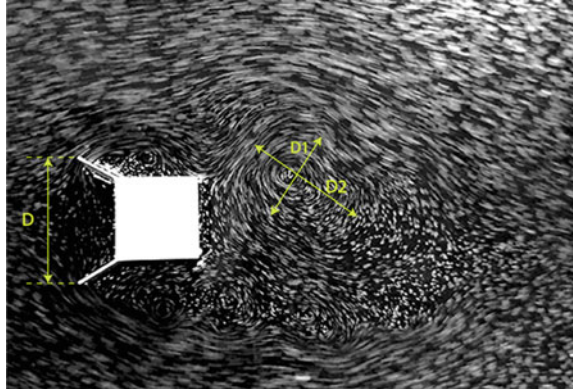
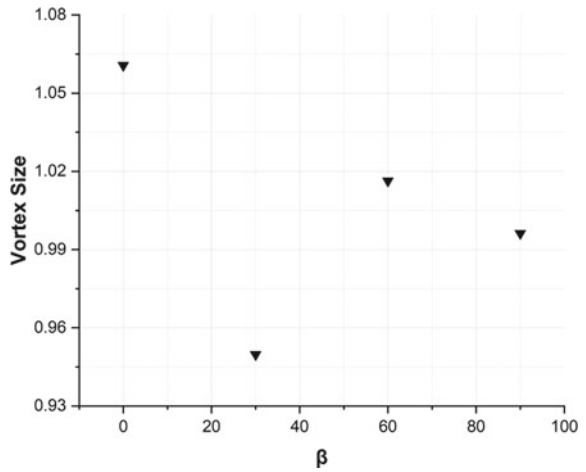


**Fig. 6** Variation of vortex size with angle ( $\beta$ )



The vortex size gives us an idea of the circulation contained in vortices. Figure 6 shows how the vortex size varies with respect to  $\beta$ . It is observed that at  $\beta = 0^\circ$  vortex size attains the maximum value which corresponds to the minimum vortex length.

### 3.4 Total Circulation Shed and Circulation Contained in Vortex

The total circulation at the separation point can be measured using the relation proposed by [21] as follows:

$$\frac{\Gamma_s}{U_0 \cdot D} = \frac{0.5 \cdot U_S^2}{St \cdot U_0^2} \tag{5}$$

where  $\Gamma_s$  is the total circulation shed and  $U_s$  is the flow velocity just outside the boundary layer at the separation point.

$U_s/U_0$  is given by Eq. (6).

$$\frac{U_s^2}{U_0^2} = 1 - C_{pb} = K^2 \tag{6}$$

Utilizing Eqs. (5) and (6), total circulation shed is calculated for different cases. The plot of total circulation shed with respect to  $\beta$  is shown in Fig. 7. It shows a reduction in  $\Gamma_s$  at  $\beta = 30^\circ$  and a slight increase for  $\beta = 60^\circ$ . It is interesting to note that  $\Gamma_s$  nearly follows the trend of vortex size (Fig. 7).

The ratio of the coefficient of drag ( $C_D$ ) to total circulation shed ( $\Gamma_s$ ) is found for all cases and the values are found to collapse at about 0.235 (Table 1). This complies with the observation of [12].

The circulation contained in vortex ( $\Gamma_v$ ) is calculated using the relation [6, 18]:

$$\frac{\Gamma_v}{U_0 \cdot D} = \frac{2 \cdot U_c \cdot a \cdot \coth(\frac{\pi \cdot b}{a})}{U_0 \cdot D} \tag{7}$$

**Fig. 7** Variation of total circulation at separation point with angle ( $\beta$ )

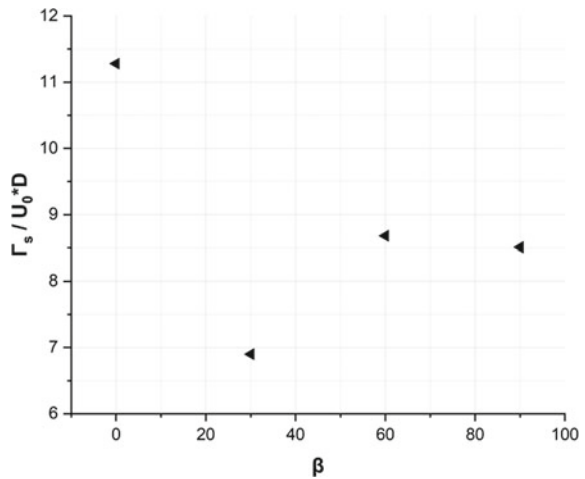


**Table 1** Strouhal number, drag, and circulation values of the model

Model	St	$C_D$	$\Gamma_s / U_0 \cdot D$	$\Gamma_v / U_0 \cdot D$	$C_D / \Gamma_s$	$\Gamma_v / \Gamma_s$
$\beta = 0^\circ$	0.11	2.7	11.28	4.68	0.239	0.415
$\beta = 30^\circ$	0.17	1.63	6.90	2.92	0.235	0.422
$\beta = 60^\circ$	0.12	1.99	8.68	4.74	0.228	0.545
$\beta = 90^\circ$	0.13	1.97	8.51	4.35	0.230	0.511
Square	0.13	2.19	9.17	3.77	0.238	0.411

where  $U_c$  is the velocity of the vortices relative to the free stream, ' $b$ ' is the lateral spacing between the rows of vortices, ' $a$ ' is the longitudinal spacing between consecutive vortices in a row, and ' $b/a$ ' is the vortex spacing ratio.

' $b$ ' can be estimated from the relation proposed by [5] given in Eq. (8).

$$0.181 = \frac{St \cdot b}{K \cdot D}. \quad (8)$$

Here,  $St$ ,  $K$ , and  $D$  being known parameters, ' $b$ ' can be estimated.

$U_c/U_0$  is given by Eq. (9) [18].

$$\frac{U_c}{U_0} = 1 - \frac{St \cdot a}{D} \quad (9)$$

Here, ' $a$ ' is unknown.

In order to find the value of ' $a$ ,' we can consider the equation for  $C_D$  in case of idealized two parallel rows of staggered vortices [18, 20].

$$C_D \cdot St = \frac{4}{\pi} \left(1 - \frac{U_c}{U_0}\right) \left(\frac{U_c^2}{U_0^2}\right) \left[ \coth^2\left(\frac{\pi b}{a}\right) + \left(\frac{U_0}{U_c} - 2\right) \left(\frac{\pi b}{a}\right) \coth\left(\frac{\pi b}{a}\right) \right] \quad (10)$$

where  $U_c/U_0$  is replaced by the term  $(1 - \frac{St \cdot a}{D})$ .

The modified equation is as follows:

$$C_D \cdot St = \frac{4}{\pi} \left(\frac{St \cdot a}{D}\right) \left(1 - \frac{St \cdot a}{D}\right)^2 \left[ \coth^2\left(\frac{\pi b}{a}\right) + \left(\frac{1}{1 - \frac{St \cdot a}{D}} - 2\right) \left(\frac{\pi b}{a}\right) \coth\left(\frac{\pi b}{a}\right) \right] \quad (11)$$

Here, all the parameters are known except ' $a$ ', which is estimated by iteration using the Secant method.

After finding all these parameters, circulation contained in a vortex ( $\Gamma_v$ ) is found from Eq. (7).

As seen in Fig. 8, vortex spacing reduces linearly with increase in  $\beta$  till  $\beta = 60^\circ$  further to which it remains nearly constant. It could be seen that vortex circulation ( $\Gamma_v$ ) versus  $\beta$  follows nearly the same trend as that of  $\Gamma_s$  and vortex size (Fig. 9). The ratio of ( $\Gamma_v$ )/( $\Gamma_s$ ) has been evaluated for all cases and found to be in the range of 0.4150–0.5459 as Table 1 shows. This indicates that about 45–58% of the vorticity generated at the separation point get lost during vortex formation. Table 1 presents a comprehensive list of aerodynamic parameter values for different cases.

Results presented above reveals that for a square cylinder fitted leading-edge fins, inclination of the body brings changes in the aerodynamic characteristics such as Strouhal number, base pressure coefficient, coefficient of drag, vortex formation length, vortex size, and the circulations. It is to be specifically noted that  $C_D$  registers its minimum value at  $\beta = 30^\circ$  which also corresponds to minima of vortex size

**Fig. 8** Variation of vortex spacing ratio with angle ( $\beta$ )

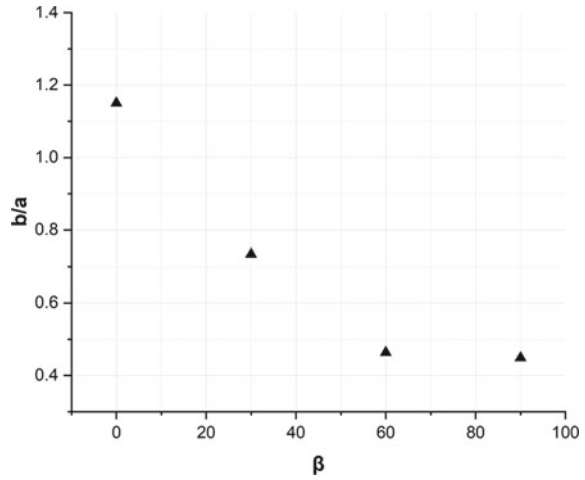
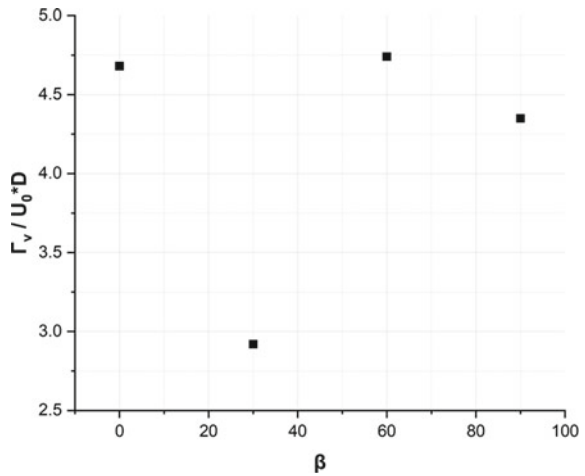


**Fig. 9** Variation of circulation contained in vortex with angle ( $\beta$ )



and shed circulation and vortex circulation. As expected, Strouhal number attains its maximum value at this body inclination. Current results comply with the observation of [17] that vortex size is proportional to the vortex circulation content. Current results indicates that about 45–58% of the generated vorticity get lost during the process of vortex formation. This could be due to the vorticity cancelation in the wake and turbulent mixing of flow at the cylinder base region where forming vortices from upper and lower shear layers interact [7]. Body inclination can be equivalently viewed as flow angle of incidence when wind blows over building structures. Therefore, the present study reveals that the aerodynamic characteristics of such structures including the forces acting on them change when the flow incidence angle changes. Practical precautions should be taken to reduce the flow-induced forces acting on

structures. The current study is being extended to deduce the effect of fin length and fin angle. Results of this study are taken at a single subcritical Reynolds number value of 2100 and at a single value of fin angle, viz.  $30^\circ$ . Also, the aerodynamic parameters estimated are based on empirical relations proposed by earlier investigators. Hence, they are approximate values. Though approximate, authors believe that this investigation could bring out the influence of body inclination to the flow on a comparative scale. These could be considered as the limitations of the current study. More detailed investigations are planned in the future to overcome the said limitations.

## 4 Conclusion

In this study, a square section cylinder with leading-edge fins fixed at  $30^\circ$  angle facing free stream is examined at various angles of inclination and their influence on global aerodynamic parameters have been discussed.

Results show that at  $\beta = 0^\circ$ , the body experience the maximum coefficient of drag. Furthermore,  $C_D$  registers its minimum value at  $\beta = 30^\circ$  which also corresponds to minima of vortex size, shed circulation, and vortex circulation. The  $C_D$  shows an enhancement of 22.9% in comparison with square cylinder. The maximum value of Strouhal number is observed at this body inclination ( $\beta = 30^\circ$ ), and the minimum value is at  $\beta = 0^\circ$ . In this case, there is an enhancement of 37% in the Strouhal number value. Strouhal number also shows an enhancement of 28.09% compared to a square cylinder. The minimum vortex size occurs at  $\beta = 30^\circ$  and the maximum at  $\beta = 60^\circ$  resulting in an enhancement of 11.67%. Vortex size also shows 43.9% enhancement compared to a square cylinder. The ratio of drag force to shed circulation is nearly invariant and found to collapse to value of about 0.23 and ratio between ( $\Gamma_v$ ) and ( $\Gamma_s$ ) is found to be in a range of 0.415–0.545. Vortex spacing reduces with body inclination which indicates that the upper and lower vortex rows become closer for a given longitudinal spacing.

The present study shows that aerodynamic characteristics have undergone notable changes which indicate the influence of body inclination on the flow structures. Results of this study are thought to have practical relevance in engineering applications such as construction of bridges, towers, tall buildings, and energy harvesters.

## References

1. Ajith Kumar R, Gowda BHL (2006) Flow-induced vibration of a square cylinder without and with interference. *J Fluids Struct* 22(3):345–369
2. Ajith Kumar R, Sohn CH, Gowda BHL (2009) Influence of corner radius on the near wake structure of a transversely oscillating square cylinder. *J Mech Sci Technol* 23:2390–2416



3. Ajith Kumar R, Sohn CH, Gowda BHL (2015) A PIV study of the near wake flow features of a square cylinder: influence of corner radius. *J Mech Sci Technol* 29:527–541
4. Ajith Kumar R, Arunkumar K, Hariprasad CM (2015) Effect of dissimilar leading edges on the flow structures around a square cylinder. *J Pressure Vessel Technol* 137:6
5. Bearman PW (1967) On vortex street wakes. *J Fluid Mech* 28(4):625–641
6. Bearman PW, Obasaju ED (1982) An experimental study of pressure fluctuations on fixed and oscillating square-section cylinders. *J Fluid Mech* 119:297–321
7. Cantwell B, Coles D (1983) An experimental study of entrainment and transport in the turbulent near wake of a circular cylinder. *J Fluid Mech* 136:321–374
8. Chakkalaparambil Many H, Yashwanth N, Bhardwaj H, Kumar RA, Gowda BHL (2014) Effect of corner cut on the near wake flow structures of a square cylinder. In: *Engineering systems design and analysis*, vol 45844. American Society of Mechanical Engineers, p V002T11A017
9. Gowda BHL, Ajith Kumar R (2006) Flow-induced oscillations of a square section cylinder due to interference effects. *J Sound Vib* 297:842–864
10. Du X, Shi D, Dong H, Liu Y (2021) Flow around square-like cylinders with corner and side modifications. *J Wind Eng Ind Aerodyn* 215:104686
11. Hu G, Tse KT, Kwok KCS (2016) Enhanced performance of wind energy harvester by aerodynamic treatment of a square prism. *Appl Phys Lett* 108(12):123901
12. Hu JC, Zhou Y, Dalton C (2006) Effects of the corner radius on the near wake of a square prism. *Exp Fluids* 40:106–118
13. Kawai H (1998) Effect of corner modifications on aeroelastic instabilities of tall buildings. *J Wind Eng Ind Aerodyn* 74:719–729
14. Krishnamoorthy S, Price SJ, Paidoussis MP (2001) Cross-flow past an oscillating circular cylinder: Synchronization phenomena in the near wake. *J Fluids Struct* 15(7):955–980
15. Kwok KCS, Wilhelm PA, Wilkie BG (1988) Effect of edge configuration on wind-induced response of tall buildings. *Eng Struct* 10(2):135–140
16. Kwok KC, Bailey PA (1987) Aerodynamic devices for tall buildings and structures. *J Eng Mech* 113(3):349–365
17. Luo SC (1992) Vortex wake of a transversely oscillating square cylinder: a flow visualization analysis. *J Wind Eng Ind Aerodyn* 45(1):97–119
18. Luo SC, Yazdani MG, Chew YT, Lee TS (1994) Effects of incidence and afterbody shape on flow past bluff cylinders. *J Wind Eng Ind Aerodyn* 53(3):375–399
19. Nawaz MA, Abubaker M, Kumar RA, Sohn CH (2022) Drag reduction for flow past a square cylinder through corner chamfering. *J Mech Sci Technol*: 1–10
20. Obasaju ED (1983) An investigation of the effects of incidence on the flow around a square section cylinder. *Aeronaut Q* 34(4):243–259
21. Roshko A (1954) On the drag and shedding frequency of two-dimensional bluff bodies (No. NACA-TN-3169)
22. Saha AK, Muralidhar K, Biswas G (2000) Experimental study of flow past a square cylinder at high Reynolds numbers. *Exp Fluids* 29(6):553–563
23. Van Oudheusden BW, Scarano F, Van Hinsberg NP, Roosenboom EWM (2008) Quantitative visualization of the flow around a square-section cylinder at incidence. *J Wind Eng Ind Aerodyn* 96(6–7):913–922
24. Wang Q, Jiang Q, Hu G, Chen X, Li C, Xiao Y (2021) Aerodynamic characteristics of a square cylinder with corner fins. *Adv Bridge Eng* 2(1):1–20
25. Yamagishi Y, Kimura S, Oki M, Hatayama C (2009) Effect of corner cutoffs on flow characteristics around a square cylinder. In: *10th international conference on fluid control, measurements, and visualization*, Aug 2009
26. Yoon DH, Yang KS, Choi CB (2010) Flow past a square cylinder with an angle of incidence. *Phys Fluids* 22(4):043603

# Effect of Unusual Terrain on Local Wind Characteristics



N. Shafeek, K. Anjana, G. Tom, K. Vivek, A. Cini, P. S. Rahul,  
and K. Suresh Kumar

**Abstract** In the lowest layer of the atmosphere, the wind is slowed down by the drag effect of the numerous features on the earth's surface such as vegetation, ground roughness, and human construction. Within this layer, wind speed generally increases with height until the top of the layer is reached, where surface drag is no longer a factor. However, mountains and valleys in the vicinity of a study site can have a significant impact on wind patterns, deviating from the typical wind characteristics seen in flat, open, suburban, or urban areas. This paper details the methodology of accounting for the wind characteristics at a site surrounded by unusual terrain in the wind tunnel.

**Keywords** Terrain effects · Topographical study · Wind engineering · Wind tunnel

## 1 Introduction

In wind tunnel tests, to measure wind-induced pressures and responses on a building model, it is important to replicate the full-scale equivalent mean wind speed profile, turbulence intensity profile, and the length scale of turbulence within the simulated atmospheric boundary layer inside the wind tunnel. A scaled test model is mounted near the center of the turntable in the test section. All major features and structures within a minimum full-scale radius of about 500 m covered by the turntable are also modeled in detail; this is to assure that their effect on the wind flows around the study site is captured accurately. Upstream of the turntable, the terrain roughness

---

N. Shafeek · K. Anjana (✉) · G. Tom · K. Vivek · A. Cini · P. S. Rahul  
RWDI Consulting Engineers India Pvt. Ltd., Thiruvananthapuram, India  
e-mail: [anjana.krishnan@rwdi.com](mailto:anjana.krishnan@rwdi.com)

N. Shafeek  
e-mail: [shafeek.nizarudeen@rwdi.com](mailto:shafeek.nizarudeen@rwdi.com)

K. Suresh Kumar  
RWDI Group Inc., Milton Keynes, UK

is modeled by generalized roughness distributed over the floor of the wind tunnel's working section. In addition, specially designed turbulence generators (spires) are installed at the start of the working section of the wind tunnel. By varying the floor roughness and turbulence generators, the effects of various types of typical terrain roughness upwind of the turntable can be reproduced at the model scale. A detailed explanation of these techniques is provided by Irwin [7]. The ESDU methodology [2, 3] of ascertaining profiles for each direction is used for characterizing the oncoming turbulence and speed for each angle. However, this approach does not apply to buildings or structures that are built amid a wide variety of topographic features such as mountains, rivers, ridges, escarpments, etc. These topographic features are capable of modifying the wind profile, and this needs to be accounted for in the wind tunnel test. These local topographical features can accelerate or decelerate wind speed and turbulence depending on the situation. In reality, topographical features are complex and consist of various features similar to a rolling hill scenario. These are important for structures like bridges, tall buildings, long-span roofs, and other wind-sensitive structures where aerodynamic stability and wind-induced responses are dependent on the turbulence characteristics and wind speed at the site.

Many studies have been carried out to determine topographic multipliers for use in such scenarios. Studies on the same had started way back in the 1980s [8]. Glanville and Kwok [5] studied the measurement of topographic multipliers and flow separation in model scale and Holmes et al. [6] studied the measurement of topographic multipliers and flow separation in full scale for steep escarpments. Suresh Kumar et al. [10] studied the wind characteristics at a rough mountainous terrain to assist a bridge design. Burlando et al. [1] used numerical simulations to arrive at a parameter called altitude coefficient that provides the ratio between the mean wind velocity in complex topography and the corresponding value at sea level. Tha and Khin [11] performed numerical simulations for generating wind profiles for complex terrains. Tse et al. [12] describe how the topography-induced pitch and yaw angles affect the wind loading on structures using a series of wind tunnel tests and CFD simulations. Studies have also demonstrated the use of neural networks for the development of a global BLWT data atlas to inform the development of methods to predict topographic wind speedup for a diverse range of topography and surface roughness conditions [4, 9].

To determine the site-specific wind characteristics, especially in the absence of full-scale measurements, the effects of such topography can only be effectively determined through topographical model studies or numerical simulations in the case of complex topography.

The purpose of this paper is to examine the usefulness of wind tunnel studies in determining site-specific wind conditions for a project. This paper presents the methodology of a topographical study and provides case studies conducted at RWDI. The main goals of the topographical study are to gather data on changes in average wind speed, flow direction, and turbulence intensity at the project location and apply the same during the testing of the structure.

## 2 Topographical Modeling

Typical wind tunnel studies of structures are carried out at 1:200–1:500 scale models. This would hardly cover less than a 0.5 km radius of the topography around the site in the traditional sizes of the boundary layer wind tunnels, and this will not capture the effects of rolling hills/mountains for many kilometers. To account for this, a small-scale model of 1:2500–1:5000 of the project site as well as all major topographical features within a radius of 3.6–10 km radius shall be selected and tested in a boundary layer wind tunnel. The radius chosen for the topography disk is based on the size of the wind tunnel turntable as well as the extent of the topography required to be modeled in the turntable. For a 1.2 m radius turntable, the extent of topography that can be modeled in a 1:3000 scale can be 3.6 km. However, when the radius and scale increases, larger extents can be covered on the disk.

The contour model of the study site is constructed using a Computer Numerical Control (CNC) machine based on GIS information. Special care is taken to elevate and contour the approach to maintain a smooth transition to the model. The objective of the topographical study and subsequent wind simulation for the actual wind tunnel test for a structure on a larger scale of 1:200–1:500 is to ensure that the effects of the far-field topography, which could not be physically modeled in the larger-scale wind tunnel test, are captured. Since the buildings within a 0.5 km radius are present for the subsequent 1:200–1:500 scale wind tunnel tests, their impact on the local flows would be accounted for directly. Wind direction is defined as the direction from which the wind blows, measured clockwise from true north.

Initially, a topographic study at a scale ranging between 2500 and 5000 is carried out to determine the mean wind and turbulence profiles along the height at the study site. For this wind tunnel test, beyond the modeled disk, the approaching profile is determined using the ESDU method for every 20° angle of attack. This profile is used for measuring the turbulence intensity and mean wind velocity including the mountains and other topographic features in the disk. Thereafter, equivalent profiles are generated at a larger scale for the actual testing of the building, to achieve similar turbulence intensity and mean velocity as if the wind was passing through those mountains and other features.

In the topography test, measurements of the wind speed and turbulence intensity are taken at several heights ranging from 50 to 2500 m above grade. The height of interest also includes the roof height of the model, the deck height of the bridge, the top of the pylon, etc. Further, in the case of bridges, measurements are also carried out at mid-span and quarter spans of the deck as well as below the deck. The measurements are made for the full compass range nominally at 20° increments. Additional measurements are conducted at 10° increments where significant upwind topography changes occur, to capture these effects in detail. Measurements of the three components of mean wind speed and turbulence intensity are obtained using a cobra probe. This device is specifically designed for measuring wind speed and turbulence intensity.

The mean wind speeds at height  $z$  ( $U_z$ ) are normalized by the free stream velocity ( $U_g$ ), which is measured at a nominal height beyond 1000 m above grade where the effect of topography ceases to influence. The ratio of the mean speed at height  $z$  ( $U_z$ ) to the mean speed at 600 m over open terrain could then be calculated using Eq. (1).

$$\frac{U_z}{U_{600m_{open}}} = \frac{U_z}{U_g} \cdot \frac{U_g}{U_{600m_{open}}} \quad (1)$$

$U_g/U_{600m_{open}}$  can be obtained from the wind tunnel test as well if there is any flat plateau in the disk itself, otherwise, standards shall be used. Wind speed and turbulence intensities are checked at heights of interest above grade (in general—the roof height of the study building) to ensure that the wind characteristics in the large-scale wind tunnel test would be representative of the wind characteristics over the site as recorded on the topographical model. As discussed earlier, the immediate modeled surroundings as a part of large-scale test are not included in the topographical wind profile measurements. Surroundings beyond the limits of the model are simulated by spires and generalized roughness elements on the wind tunnel floor. The application of the velocity scaling factors described below accounts for, on a direction-by-direction basis, any remaining mismatch between the “target” flow parameters obtained from the topography study and the modeled flow properties at the large scale required for the wind tunnel test of the structure.

During the large-scale wind tunnel tests (for example 1:300), the reference wind speed is measured at an equivalent height which is the practical maximum height for the wind tunnel. The results of the tests are required, however, to be in terms of the 600 m above sea level velocity over open terrain,  $U_{600m_{open}}$ . Therefore, a velocity scaling factor,  $F$ , is needed to convert the reference velocity,  $U_{ref}$ , measured over the proposed development to the appropriate value over open terrain. This factor,  $F$ , is based on the concept of matching peak gust velocities between the two scale models at the matching heights, which leads to the following Eq. (2), where the small-scale test is assumed to be 1:3000 scale model:

$$U_{ref} = F \cdot U_{600m_{open}} \quad (2)$$

$$F = \left\{ \frac{U_z[1 + g \cdot I_z(z)]}{U_{600m_{open}}} \right\}_{1:3000} \cdot \left\{ \frac{U_{ref}}{U_z[1 + g \cdot I_z(z)]} \right\}_{1:300}$$

where

- $z$  the height of interest above the grade.
- $U_z$  the mean wind speed measured at the height of interest.
- $I_z(z)$  the turbulence intensity at the height of interest.
- $U_{600m_{open}}$  the mean wind speed specified at 600 m above sea level over open terrain.
- $U_{ref}$  the mean wind speed measured at the reference height in the wind tunnel.

$g$  the peak factor, defined as the ratio of the peak velocity fluctuation to the r.m.s. velocity.

Velocity scaling factors ( $F$ ) are then calculated for all wind directions for the matching heights. In addition, the final velocity scaling factors are adjusted to smooth the variations in wind direction to establish more realistic values. These values are evaluated from the mean velocity and turbulence measurements on the large-scale wind tunnel test and small-scale topography test. The actual wind tunnel test is then carried out using these factors and modified profiles and results are obtained for the study model.

### 3 Case Study 1

The location of the project is depicted in Fig. 1. As can be seen from the figure, the study site is surrounded by a complex topography including mountains, valleys, water bodies, and tall buildings.

A 1:3000 scale model including all major topographical features within a radius of at least 3.6 km from the site was tested in RWDI's 2.4 m × 1.8 m boundary layer wind tunnel. The topographical model represented in detail the influence of the major topographical features within 3.6 km of the project location. For the wind tunnel test, the influence of the terrain beyond the detailed model was represented using roughness on the wind tunnel floor and spires. Figure 2 shows the photograph



Fig. 1 Location of the study building

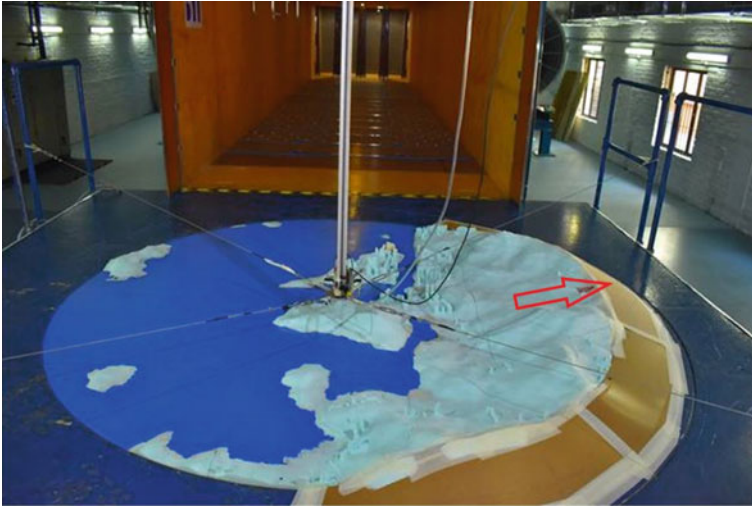


**Fig. 2** Topographic model at 1:3000 scale



**Fig. 3** Wind tunnel test at 1:300 scale

of the 1:3000 scale topography model in the boundary layer wind tunnel covering 3.6 km. The 1:300 scale test with the study building (in red) and immediate surrounds for a radius of 365 m is depicted in Fig. 3. Figure 3 also shows a series of tall pink color cubes at the entrance of the tunnel mouth, which have been used to generate the wind flow characteristics required at the 1:300 scale equivalent to the measurements made at 1:3000.



For winds from the southwest and west as shown in Fig. 2, the model was relatively flat, making the wind tunnel measurements for those directions more affected by the upwind profile than measurements taken for other directions where the local topography would have had a greater impact.

The wind speed and turbulence intensities are measured and checked to ensure that the wind characteristics at the 1:300 scale model would be representative of the wind characteristics over the site as recorded on the 1:3000 scale topographical model. Surroundings beyond the limits of the model are simulated by non-traditional combination of spires and generalized roughness elements on the wind tunnel floor to achieve the desired wind characteristics seen in the topographical study. During the 1:300 scale studies, the reference wind speed is measured at an equivalent height of 366 m above grade in site terrain. Therefore, a velocity scaling factor,  $F$ , was needed to convert the 366 m reference velocity,  $U_{ref}$ , measured over the study site to the appropriate value over open terrain at 600 m, using Eq. (2).

Figures 4 and 5 show a reasonably good comparison of the normalized mean wind speed and turbulence intensities respectively at 74 m height between the 1:3000 and 1:300 scale wind tunnel test. The mean wind speed is normalized by reference height wind speeds. Remaining mismatch between the two tests has been accounted using factors during the analysis. As can be clearly seen from Figs. 4 and 5 the mean wind speed is reduced when wind is coming over the mountains (clockwise from west through east), but induced turbulence is quite high. In open directions (clockwise from east through west), mean speed is high, and turbulence is low.

During the analysis stage of the wind tunnel results, in the mathematical model of the wind climate, the wind speeds recorded at the nearby meteorological station are scaled up to those at the gradient height according to the local topography in the area. These wind speeds at the gradient height are not expected to change from location to location and are considered applicable to the current study. The mathematical model is then combined with the wind tunnel data to predict the frequency of occurrence of full-scale wind speeds.

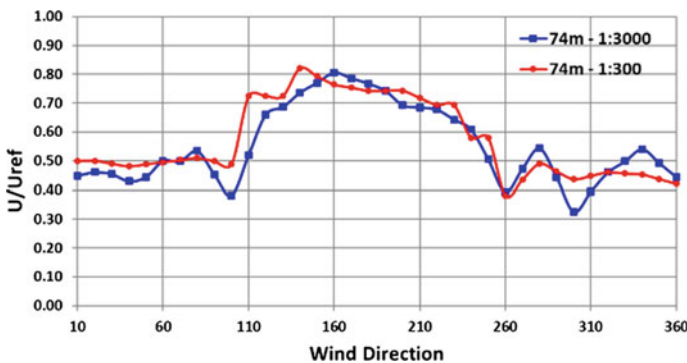


Fig. 4 Normalized mean wind speed



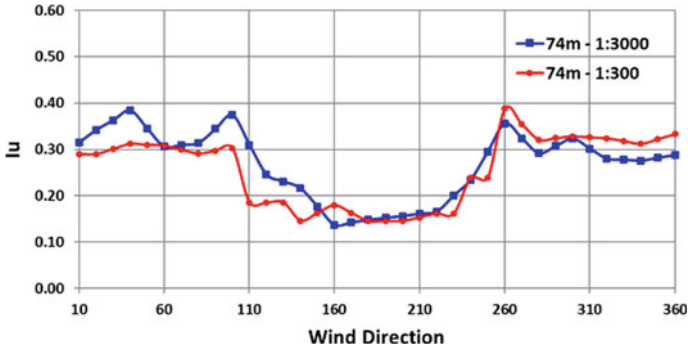


Fig. 5 Turbulence intensity

### 4 Case Study 2

The location of the project is depicted in Fig. 6. It stands on a valley beneath a mountain and is surrounded by tall buildings.

A 1:3000 scale model including all major topographical features within a radius of at least 7.3 km from the site was tested in RWDI’s 5.0 m × 3.0 m boundary layer wind tunnel. The mountains and valleys, particularly to the south and southwest, can produce various effects on the wind velocity and turbulence intensity at the site. Figure 7 shows the photograph of the topography model in the boundary layer wind tunnel. The 1:300 scale test with the study building (in red) and immediate



Fig. 6 Site location of the study building



**Fig. 7** 1:3000 scale topography model



**Fig. 8** Wind tunnel test at a large scale of 1:300

surroundings for a radius of 365 m are depicted in Fig. 8. The figure also shows a few horizontal wooden plates that are used to modify the wind profile to match the characteristics obtained from the topography test.

Before testing, measurements were made of the wind profile, without buildings and large-scale topography upwind, to confirm that the approach open terrain wind

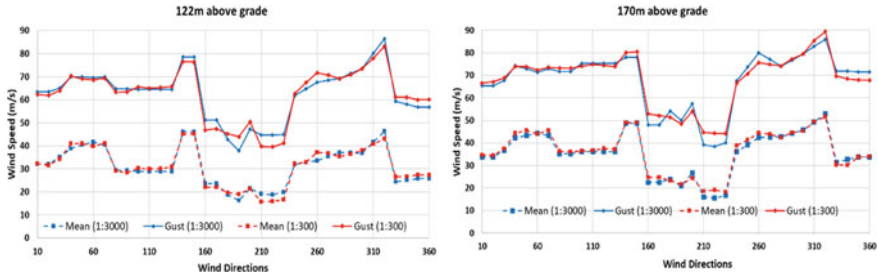


**Fig. 9** Comparison of simulated wind speed at 1:3000 and 1:300 scale models

profile would be appropriate. This profile was then compared to the approach profile specified in the Code of Practice.

Measurements of the wind speed and turbulence intensity were taken at several heights ranging from 50 to 1500 m above grade. For the development and scaling of the 1:300 flow profiles measurements, nominal heights of 122 m and 170 m above site grade were of the most interest as the “matching heights” based on the roof height of the study building.

During the 1:300 scale studies, the reference wind speed was measured at an equivalent height of 457 m above site grade in site terrain. This height was the practical maximum for the wind tunnel. The results of the tests were required, however, to be in terms of the 600 m above sea level velocity over open terrain,  $U_{600m\_open}$ . Therefore, a velocity scaling factor,  $F$ , was needed to convert the 457 m reference velocity,  $U_{ref}$ , measured over the proposed development to the appropriate value over open terrain. Figure 9 shows a comparison of the peak gust speeds at both matching heights, based on the scaling factors.

Figure 9 shows that mean and peak gust measured at 1:300 and 1:3000 is in good agreement with each other. From Fig. 9 (clockwise from southeast to southwest), it is seen there is a significant reduction in wind speed due to the sheltering from the immediate mountainous terrain as is expected.

## 5 Conclusions

Codes recommend topographic factors which are evaluated under idealized terrains and fail to accurately predict the impact of complex topographic features such as a combination of hills, valleys, cliffs, escarpments, or ridges which can significantly affect wind flow characteristics. Numerical simulations or wind tunnel tests are quintessential in calculating the actual aerodynamics at the location. The paper reiterates the importance of conducting a topography study to accurately capture the impact of local terrain on the wind flows at the site. This study is suggested for structures in unusual terrain conditions to ensure that the site-specific wind characteristics are aptly captured in the wind tunnel test. The methodology of conducting

a topography study in the wind tunnel and its application in the wind tunnel test is presented through two case studies. These case studies have also demonstrated that the results of a small-scale topography study can be translated to a large-scale wind tunnel study in good agreement.

## References

1. Burlando M, Pizzoa M, Repetto M, Solari G (2013) Design wind speed in complex topography. In: 12th Americas conference on wind engineering 2013: wind effects on structures, communities, and energy generation, ACWE 2013, Seattle, WA, United States, 16 June 2013–20 June 2013
2. ESDU (1982) Strong winds in the atmospheric boundary layer. Part 1: mean hourly speeds, item 82026, Issued September 1982 with Amendments A and B April 1993. Engineering Sciences Data Unit, ESDU International, 27 Corsham Street, London N16UA
3. ESDU (1983) Strong winds in the atmospheric boundary layer. Part 2: discrete gust speeds, item 83045, Issued November 1983 with Amendments to 1993. Engineering Sciences Data Unit, ESDU International, 27 Corsham Street, London N16UA
4. Girma B, Stathopoulos T, Bedard C (2003) Numerical evaluation and neural net predictions of wind flow over complex terrain. In: Proceedings of the eleventh international conference on wind engineering, Lubbock, Texas, June 2003
5. Glanville MJ, Kwok KCS (1997) Measurements of topographic multipliers and flow separation from a steep escarpment. Part I. Model-scale measurement. *J Wind Eng Industr Aerodyn* 61–71:893–902
6. Holmes JD, Banks RW, Paevere P (1997) Measurements of topographic multipliers and flow separation from a steep escarpment. Part I. Full scale measurement. *J Wind Eng Industr Aerodyn* 61–71:885–892
7. Irwin PA (1979) Design and use of spires for natural wind simulation. National Research Council of Canada, N.A.E. Report LTR-LA-233
8. Meroney RN (1980) Wind tunnel simulation of the flow over hills and complex terrain. *J Industr Aerodyn* 5:297–321
9. Santiago-Hernández JX, Román Santiago A, Catarelli RA, Phillips BM, Aponte-Bermúdez LD, Masters FJ (2022) Predicting topographic effect multipliers in complex terrain with shallow neural networks. *Front Built Environ*. <https://doi.org/10.3389/fbuil.2022.762054>
10. Suresh Kumar K, Garber J, Yakymyk W, Hunter M, Irwin PA (2006) A wind tunnel investigation of topographical effects on wind flows at the Anji Khad arch bridge site in India. In: Third national conference on wind engineering, Kolkata, India, 5–7 Jan 2006
11. Tha ZSK, Khin AM (2018) Numerical simulation of wind flow over complex terrain of Yangon City. *Int J Adv Sci Res Eng (IJASRE)* 4(4):62–69
12. Tse KT, Weerasuriya AU, Gang H (2020) Integrating topography-modified wind flows into structural and environmental wind engineering applications. *J Wind Eng Industr Aerodyn* 204

# Vibrational Characteristics of the LEP Vertical-Axis Wind Turbine Shaft for Various Solidity Ratios



E. Karthik Vel, G. Vinayagamurthy, Gao Liang, and S. Nadaraja Pillai

**Abstract** Vertical-axis wind turbines are more advantageous than their horizontal-axis counterparts when placed in an array. They have the maximum capability to harvest the abundantly available source of wind energy. The presence of VAWT in the region of the onset of the atmospheric boundary layer, i.e. the earth's surface, and in offshore places where continuous unsteady airflow is encountered, has severe structural impacts in the form of vibrations that lead to system failure. To put a restraint on the problems caused, in this study, the leading-edge protuberance blades (LEP) are introduced on the VAWT instead of the previously available straight blades and are tested in the axial wind blower present in the Turbulence and Flow Control Laboratory at SASTRA Deemed University. It is to understand the diversification of the vibrational characteristics measured on the main shaft of the VAWT with the help of the triaxial accelerometer connected to a versatile data acquisition system. The results revealed that the LEP suppresses the evolution of the dynamic stall vortices considerably at low tip speed ratios, which in turn reduces the vibration on the turbine shaft, leading to the prevention of catastrophic failure of the system with the corresponding increase in turbine efficiency.

**Keywords** Leading-edge protuberance · VAWT · Dynamic stall · Wind loads · Vibration

---

E. K. Vel · S. Nadaraja Pillai (✉)

Turbulence and Flow Control Laboratory, SASTRA Deemed University, Thanjavur, Tamil Nadu, India

e-mail: [nadarajapillai@mech.sastra.edu](mailto:nadarajapillai@mech.sastra.edu)

G. Vinayagamurthy

Department of Mechanical Engineering, Vellore Institute of Technology, Chennai, Tamil Nadu, India

G. Liang

School of Civil Engineering and Architecture, Xi'an University of Technology, Xi'an 710048, China

## Nomenclature

LEP	Leading edge protuberance
VAWT	Vertical axis wind turbine
VIV	Vortex-induced vibration
$\lambda$	Tip speed ratio
$\sigma$	Solidity ratio
$L$	Length of the blade $m$
$D$	Rotor diameter $m$

## 1 Introduction

The wind energy sector seems to be one of the glaring renewable energy harvesting sectors, with almost 12% annual growth and a positive upward trend. The fight for reducing carbon emissions due to global warming has put forward an increase in the rate of installation of wind turbines at around 1.4 times more than the current installation rate [1]. The horizontal-axis wind turbines, though they seem to have high individual efficiency, when placed on a wind farm require serious design consideration for the placement of the turbines to have maximum efficiency. Instead, vertical-axis wind turbines (VAWT) have been found to perform better in groups by harnessing the maximum possible wind energy close to the earth's surface and utilising the maximum turbulence wind energy due to the earth's surface boundary layer [2, 3]. There has been a recent shift from considering the power production per unit turbine to the power produced per unit area, which has led to the witnessing of almost 10 times more power per unit area for the VAWT than the array of widely spaced HAWT.

The vertical-axis wind turbine (VAWT) is known for its operation under extremely indeterministic airflow conditions due to its position very close to the Earth's surface [4]. There is a nonlinear generation of a fluctuating flow field that is more predominantly encountered by the vertical-axis wind turbine, which is generally considered to be a small-scale wind turbine [5, 6]. Although the fluctuating wind is the potential source for the harvesting power for a VAWT compared with its horizontal counterpart, there is wind-induced vibration that is caused by the above phenomena such as vortex-induced vibration (VIV), galloping, buffeting, etc. [7]. Galloping can affect the performance of a VAWT in several ways, including the dynamic stall effects on the lift-type vertical-axis wind turbine [8–10]. In a vertical-axis wind turbine (VAWT), buffeting can occur when the turbine is subjected to strong gusts of wind or other turbulence. The airfoil at larger angles of attack induces vortex-induced vibration, which introduces a lock-in phenomenon where the vortex-shedding frequency will jump to the natural frequency of the structure, which causes limited cycle oscillations [11]. The modification of the geometric profile of the wind turbine blade is found to be an efficient way to tackle such situations, particularly at points where there is a requirement for improvement with regard to aerodynamics. There was



much research performed on the modification of the airfoil surface for variation in aerodynamic characteristics [12–14].

The dynamic stall due to the instantaneous aerodynamic load was delayed, resulting in suppressing the fluctuations occurring in the base airfoil [15]. The LEP results in the formation of a secondary vortex, which weakens the leading-edge vortex, thereby increasing the coefficient of lift in both static and dynamic conditions [16, 17]. The dynamic stall vortex is stronger in the case of modified blades, which have varying flow dynamics across the span, whereas the base model has faster convection of the dynamic stall vortices [18].

In this study, the investigation of the effects of wind-induced vibrations on the VAWT with straight and LEP blades for various pitch angles, solidity ratio, and wind conditions is analysed for the reduction in fluctuations caused by aerodynamic loads.

## 2 Experimental Methodology

For the investigation, the NREL S1046 airfoil is used, which is considered a high-performance airfoil developed by the National Renewable Energy Laboratory (NREL) for use in wind turbine blades with a high lift-to-drag ratio, low stall speed, and improved power output [19]. The conceptual diagram of the VAWT support is shown in Fig. 1, with the position of the triaxial accelerometer placed on the rigid mast supporting the shaft connected with different blades. Table 1 describes the properties of the three models used for our investigation.

The tip speed ratio ( $\lambda$ ) Eq. (1) is defined as the ratio of the tip speed of the blade and the wind speed of the blade.

$$\lambda = \frac{\omega R}{V_\infty} \tag{1}$$

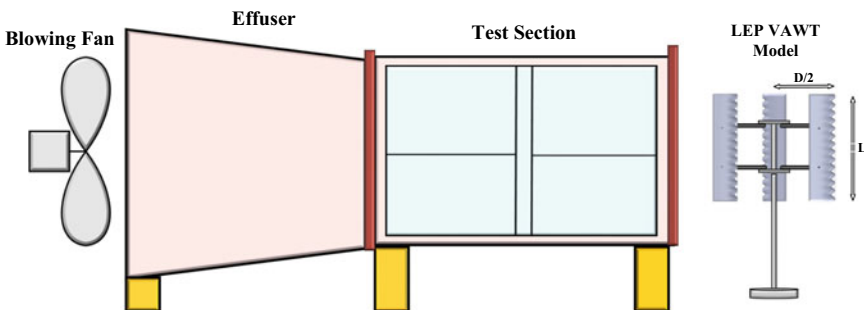


**Fig. 1** Conceptual diagram of the experimental setup used for the investigation with the axial blower

**Table 1** Model description used for the experimental investigation

Blade description	Model	No. of blades ( $N$ )	Solidity ratio ( $\sigma$ )
Straight blade (Chord $C = 14$ cm)	Model 1	4	0.68
LEP blade ( $A = 14\% C$ , $W = 36\% C$ )	Model 2	3	0.68
LEP blade ( $A = 14\% C$ , $W = 36\% C$ )	Model 3	4	0.47

Solidity ratio ( $\sigma$ ) Eq. (2) is defined as the ratio of the total blade area to the swept area of the rotor, which is tabulated in Table 1 for all the models tested.

$$\sigma = \frac{NC}{D} \quad (2)$$

### 3 Results and Discussion

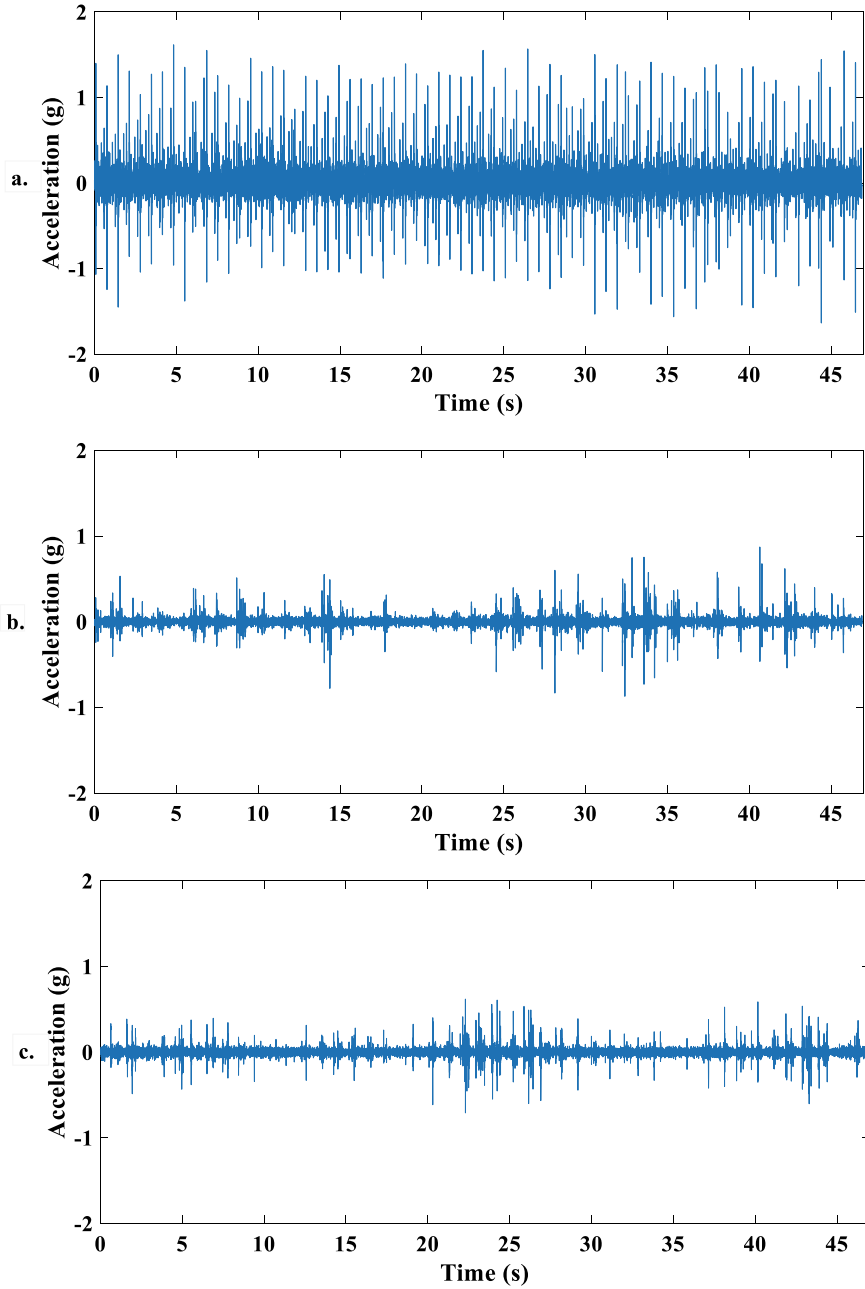
Figure 2a shows the raw acceleration data of the straight blade vertical-axis wind turbine for the crosswind of 13 m/s at the pitch angle of  $0^\circ$ , and Fig. 2b shows the corresponding acceleration data for the VAWT with leading-edge protuberance blades. The addition of a leading-edge protuberance to the vertical-axis wind turbine has reduced the acceleration values on the shaft of the wind turbine blade at similar wind conditions. Thus, the vibration induced on the vertical-axis wind turbine shaft due to variable wind conditions has a detrimental dependence on the geometry of the blades used in the VAWT system.

Figure 3a describes the variation of the tip speed for various incoming flow velocities at five different pitch angles. The tip speed was higher for the setup with a  $0^\circ$  pitch angle, but with the increase in the pitch angles from  $0^\circ$  to  $5^\circ$ , there is a drastic decrease in the tip speed, which further decreases with the increase in the pitch angle. The decrease in tip speeds is visible clearly at higher incoming flow velocities, thereby conforming with the phenomenon of dynamic stall.

For the investigation carried out for LEP blades, the tip speed seems to be much less at pre-stall angles when compared with the case of straight blades, but conversely, at the post-stall regions of  $15^\circ$  and  $20^\circ$ , the tip speed remains the same. The configuration with LEP blades has suppressed the sudden decrease in the tip speeds with the increase in the pitch angles, thereby providing evidence for the suppression of the dynamic stall phenomenon.

This helps us understand the enhanced aerodynamic stall behaviour of the LEP wind turbine blades, which maintained a constant tip speed for various wind conditions and suppressed the vibrational effects on the wind turbine shaft that were earlier caused by the straight blades.





**Fig. 2** Acceleration data obtained on the shaft of the vertical-axis wind turbine **a** model 1, **b** model 2, and **c** model 3

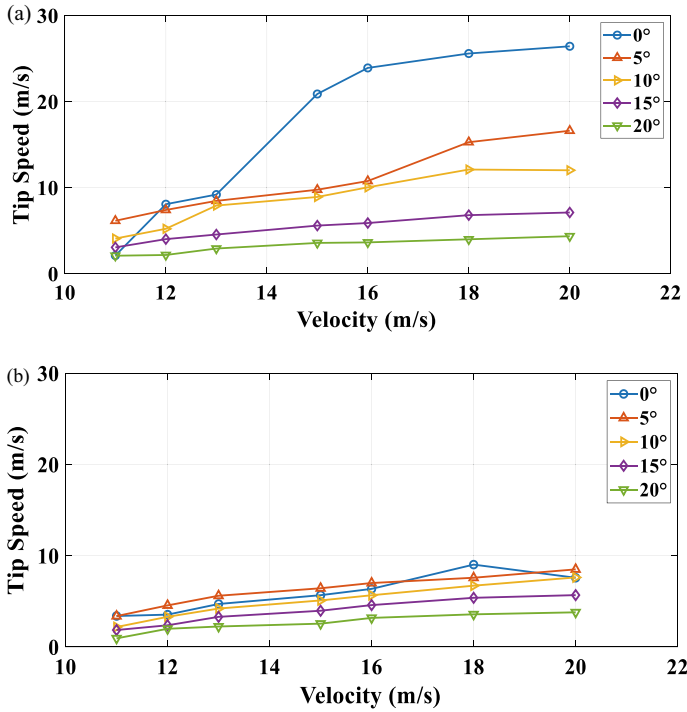


Fig. 3 Variation of tip speed for different wind conditions corresponding to different pitch angles a model 1 and b model 2

### 4 Conclusions

The series of experimental investigations performed on the VAWT configuration with and without LEP blades has led to the following conclusion:

1. The straight-blade wind turbine has shown a maximum decrease in tip speed with an increase in pitch angle.
2. The addition of the leading-edge protuberance has a comparatively lesser tip speed in the pre-stall region when compared with the VAWT with straight blades for various wind conditions.
3. The effects of the dynamic stall phenomenon on the structural vibration are observed from the reduction in tip speed for the VAWT with straight blades, and the corresponding evidence of suppression of the structural vibration was seen in the case of the VAWT with LEP blades.

Further, investigation has to be carried out by varying the amplitude and wavelength of LEP, which will result in the design of an efficient VAWT blade. The corresponding energy output arriving from the efficient blade design will potentially help us produce an efficient vertical-axis wind turbine at this immediate time of need.

**Acknowledgements** This research work was supported by the Science Engineering Research Board (SERB), Department of Science and Technology (DST), Government of India (File No: CRG/2021/005720).

## References

1. Lee J, Zhao F (2022) GWEC global wind report. Glob Wind Energy Council 75
2. Kumar R, Raahemifar K, Fung AS (2018) A critical review of vertical axis wind turbines for urban applications. *Renew Sustain Energy Rev* 89:281–291. <https://doi.org/10.1016/j.rser.2018.03.033>
3. Kc A, Whale J, Urmee T (2019) Urban wind conditions and small wind turbines in the built environment: a review. *Renew Energy* 131:268–283. <https://doi.org/10.1016/j.renene.2018.07.050>
4. Pagnini LC, Burlando M, Repetto MP (2015) Experimental power curve of small-size wind turbines in turbulent urban environment. *Appl Energy* 154:112–121. <https://doi.org/10.1016/j.apenergy.2015.04.117>
5. Solari G, Burlando M, De Gaetano P, Repetto MP (2015) Characteristics of thunderstorms relevant to the wind loading of structures. *Wind Struct An Int J* 20:763–791. <https://doi.org/10.12989/was.2015.20.6.763>
6. Suresh R, Gopal R, Pillai SN, Chandrasekar VK (2021) Evidence of extreme events in wind-induced normal stress of the columns of low- and medium-rise building structures. *EPL* 136. <https://doi.org/10.1209/0295-5075/ac30e5>
7. Lokesh U, Kirthika N, Madhu Madhan K et al (2021) Effect of solidity on the dynamic behaviour of the Darrieus turbine with leading-edge protuberance. *IOP Conf Ser Earth Environ Sci* 850. <https://doi.org/10.1088/1755-1315/850/1/012038>
8. Le Fouest S, Mulleners K (2022) The dynamic stall dilemma for vertical-axis wind turbines. *Renew Energy* 198:505–520. <https://doi.org/10.1016/j.renene.2022.07.071>
9. Horcas SG, Sørensen NN, Zahle F et al (2022) Vibrations of wind turbine blades in standstill: Mapping the influence of the inflow angles. *Phys Fluids* 34. <https://doi.org/10.1063/5.0088036>
10. Li X, Feng L-H (2022) Critical indicators of dynamic stall vortex. *J Fluid Mech* 937:A16. <https://doi.org/10.1017/jfm.2022.30>
11. Hu P, Sun C, Zhu X, Du Z (2021) Investigations on vortex-induced vibration of a wind turbine airfoil at a high angle of attack via modal analysis. *J Renew Sustain Energy* 13. <https://doi.org/10.1063/5.0040509>
12. Arunvinthan S, Raatan VS, Nadaraja Pillai S et al (2021) Aerodynamic characteristics of shark scale-based vortex generators upon symmetrical airfoil. *Energies* 14. <https://doi.org/10.3390/en14071808>
13. Ethiraj L, Pillai SN (2021) Effect of trailing-edge modification over aerodynamic characteristics of NACA 0020 airfoil. *Wind Struct An Int J* 33:463–470. <https://doi.org/10.12989/was.2021.33.6.463>
14. Livya E, Nadaraja Pillai S (2022) Effect of turbulence intensity on aerodynamic characteristics of extended trailing edge airfoil. *Aircr Eng Aerosp Technol* 94:1780–1791. <https://doi.org/10.1108/AEAT-12-2021-0382>
15. Zhang YN, Zhang MM, Cai C, Xu JZ (2020) Aerodynamic load control on a dynamically pitching wind turbine airfoil using leading-edge protuberance method. *Acta Mech Sin Xuebao* 36:275–289. <https://doi.org/10.1007/s10409-020-00939-2>
16. Wang T, Feng LH, Li ZY (2021) Effect of leading-edge protuberances on unsteady airfoil performance at low Reynolds number. *Exp Fluids* 62:1–13. <https://doi.org/10.1007/s00348-021-03310-8>

17. Arunvinthan S, Nadaraja Pillai S, Cao S (2020) Aerodynamic characteristics of variously modified leading-edge protuberanced (LEP) wind turbine blades under various turbulent intensities. *J Wind Eng Ind Aerodyn* 202:104188. <https://doi.org/10.1016/j.jweia.2020.104188>
18. Hryniuk JT, Bohl DG (2020) The effects of leading-edge tubercles on dynamic stall. *J Fluid Mech*. <https://doi.org/10.1017/jfm.2020.216>
19. Feng F, Zhao S, Qu C et al (2018) Research on aerodynamic characteristics of straight-bladed vertical axis wind turbine with S series airfoils. *Int J Rotating Mach* 2018. <https://doi.org/10.1155/2018/8350243>

# Performance Analysis of N-Beats and Regression Learners for Wind Speed Forecasting and Predictions



Jatin Prakash, P. K. Kankar, and Ankur Miglani

**Abstract** Wind energy has enormous potential to fulfil industrial and other power requirement demands specifically in remote areas. The amount of power generated from the wind turbine depends on several factors, namely wind speed, wind direction, rotor area, the height of the tower, etc. As the wind speed is highly dynamic, it highly affects the power generation capacity of the windmills. Thus, it is highly desired that wind shall be monitored as well as forecasted earlier to prevent any sudden ups or downs in the power generation. This manuscript presents a regression-based methodology to predict the wind speed using XGBoost and AdaBoost regression learners. Their learning capabilities have been compared using mean absolute error. XGBoost is found to have lesser value of MAE at 0.392. Parallely, N-Beats, the time series forecasting model is trained to forecast the wind speed. This way, the present study showcases the utility of time series forecasting method to accurately predict and forecast the wind speed.

**Keywords** Wind power · Time series forecasting · N-Beats · Regression learners

## 1 Introduction

With the increasing demand for power globally and the limited amount of fossil fuels, it is the need of the hour to look for alternative sources especially renewable sources of energy. The wind has a great potential to produce energy using some suitable means and wind power is one of the most established and efficient sources

---

J. Prakash · P. K. Kankar (✉)

System Dynamics Lab, Department of Mechanical Engineering, Indian Institute of Technology Indore, Indore 453552, India

e-mail: [pkankar@iiti.ac.in](mailto:pkankar@iiti.ac.in)

A. Miglani

Microfluidics and Droplet Dynamics Lab, Department of Mechanical Engineering, Indian Institute of Technology Indore, Indore 453552, India

e-mail: [amiglani@iiti.ac.in](mailto:amiglani@iiti.ac.in)

of renewable energy. Not only wind is used to generate the wind, but it is also used for milling grain, pumping water, windsurfing, powering ships and thus reducing carbon footprints. As per an investigation [1], the wind power capacity is growing at a rate of 30% around the world. It is quite evident that windmills are installed in windy places or in mountains where the speed of wind is considered sufficient to produce power. With the changing climate and unpredictable weather, sometimes it is quite difficult to predict or forecast wind speed in future. This uncertainty leads to fluctuations in the power supplied through the power stations. Thus, it is the need of the hour to forecast the wind speed in advance for swift management of the power supply. Previously, few of the authors have implemented wind speed forecasting using different techniques and approaches, including statistical methods, numerical weather prediction models, and machine learning techniques. Statistical methods for wind speed forecasting include time series analysis, autoregressive moving average (ARMA) models [2], autoregressive integrated moving average (ARIMA) models [3], and Kalman filters, which are commonly used to model the temporal dependencies in wind speed data. Numerical weather prediction models, such as the Weather Research and Forecasting (WRF) model and the European Centre for Medium-Range Weather Forecasts (ECMWF) model, are also commonly used for wind speed forecasting. These models use complex equations to simulate the physical processes that drive weather patterns and can provide detailed forecasts of wind speed at different heights and locations. Machine learning techniques, such as artificial neural networks (ANNs) and support vector machines (SVMs), time series-based methods like LSTM and Bi-LSTM, have also been applied to for various forecasting and classification tasks [4–10]. These techniques can be used to model nonlinear relationships in wind speed data and have been shown to perform well in comparison to traditional statistical methods. In recent years, the combination of physical models with machine learning techniques (physics-based or hybrid models) has shown promising results in wind speed forecasting. This approach uses physical understanding to improve the performance of the model and reduce the complexity of the ML models. It is worth noting that wind speed forecasting is a challenging task due to the complexity of the atmospheric processes that govern wind patterns and the sparsity and variability of wind speed data. Therefore, this manuscript presents a regression-based method to predict wind speed by using variables like active power, wind direction, etc. Two different methodologies, namely XGBoost regressor and AdaBoost regressor have been used to determine the wind speed and their performance metrics have been compared. Furthermore, a time series forecasting method is used subsequently to forecast the speed of the wind for future events to minimize the fluctuations in the power supply of the windmill. This manuscript is organized as follows: Sect. 1 presents the introduction and a brief literature review of wind speed forecasting using different means. Section 2 presents the regression analysis for predicting the wind speed by using XGBoost and AdaBoost regressors, respectively. Section 3 presents the forecasting for the wind speed using the deep learning model, N-Beats. Towards the end, Sect. 4 lists the conclusions and key takeaways from this manuscript. Figure 1 shows the methodology adopted in this manuscript for wind speed prediction and forecasting.

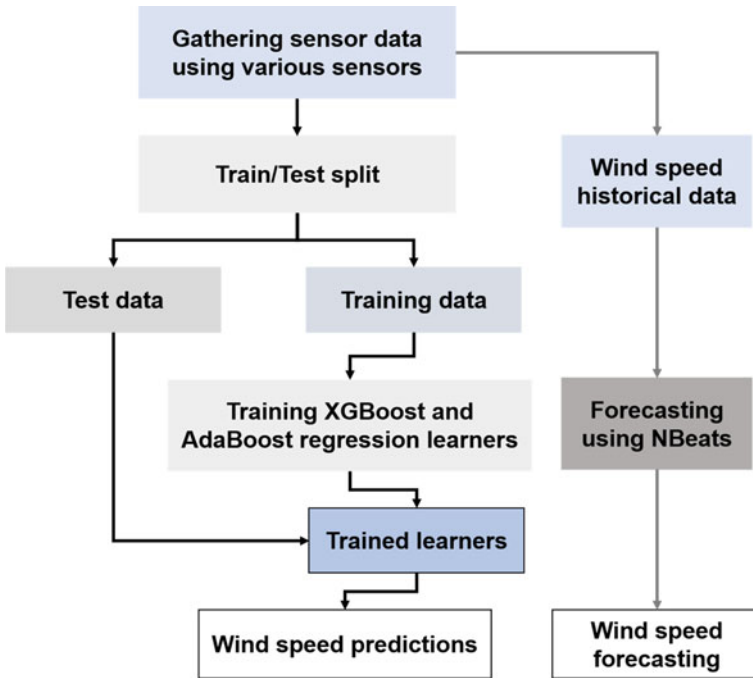


Fig. 1 Methodology adapted for the wind speed prediction and forecasting

## 2 Data Set and Regression-Based Approaches

The data set used in this study is obtained from Ref. [11]. This data set is acquired at an interval of 10 min and saves various data like wind speed, direction, and power generated and logs the theoretical power curve along with it. The data set contains 50,530 recordings. The contour of the wind speed is shown in Fig. 2. In this study, this data set is utilized for wind speed prediction as well as forecasting. For predicting the wind speed, regression models (XGBoost and AdaBoost) are trained using wind speed, direction, power generated, and theoretical power, whereas the wind speed is used as the target variable. On the other side, N-Beats is trained to forecast the speed of the wind using recent historical data.

### 2.1 XGBoost Regression

XGBoost is an ensemble machine learning model which stands for “Extreme Gradient Boosting”. It combines the predictions of multiple weak models to form a strong ensemble model. It is well capable of classification as well as regression. In regression, XGBoost predicts a continuous output value by combining the predictions

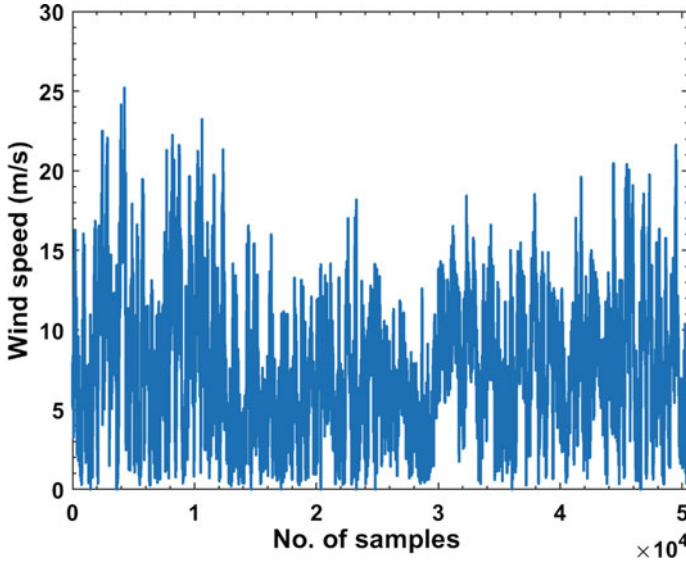


**Fig. 2** Variation of historical data of acquired wind speed

of multiple decision trees, which is a base learner in the XGBoost. The decision trees in XGBoost are built one at a time, and each tree corrects the errors carried forward by the previous tree. This process continues until the model achieves the desired accuracy or the required number of trees has been created. XGBoost provides L-1 and L-2 regularization which prevents overfitting of the model by adding a penalty to the loss function. The mathematical expression of the XGBoost is mentioned in detail in Refs. [12, 13].

To train the model, the data set is split into training and test data in the ratio of 80:20. Out of 50,530 recordings, 2720 recordings are used for testing the model and the remaining is used to train the model. Figure 3 shows the last 100 contours of the test data and the predicted data using XGBoost. It can be observed that the model achieves high accuracy during the training, and the mean absolute error is found to be 0.392.

Another statistical measure is the coefficient of determination ( $R^2$ ), which determines the proportion of variance in the dependent variable that can be explained by the independent variable. The value of  $R^2$  for trained XGBoost regression model is 0.945.

## 2.2 AdaBoost Regression

AdaBoost, short for “Adaptive Boosting”, is a machine learning algorithm used for both classification and regression. It is a meta-algorithm that can be applied to a



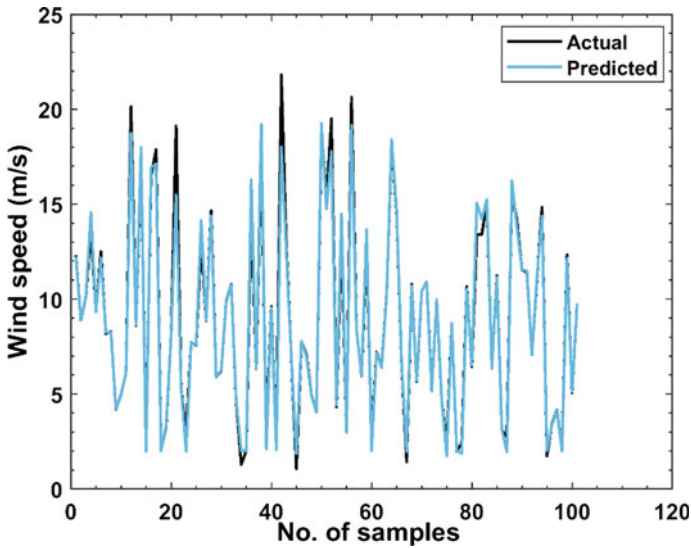


**Fig. 3** Prediction of wind speed using trained XGBoost regression learner

wide range of base classifiers. The basic idea behind AdaBoost is to train a sequence of weak classifiers, where each one tries to correct the mistakes of the previous classifier. The final output is a weighted combination of the outputs of all the weak classifiers, where the weights are determined by their accuracy. In AdaBoost, each set of features is first assigned an equal weight ( $w = 1/n$ ), and a stump is generated for each feature [14]. Subsequently, the first decision tree-based learner model is selected based on either entropy or the Gini coefficient, and the stump having the minimum value is selected for classification. Once the classification is complete, the total error is calculated by summing the individual weights of the incorrectly classified instances. In this study, the same data used to train XGBoost is used to train AdaBoost, and the mean absolute error is found to be 0.733. Figure 4 shows the wind speed predicted using the trained AdaBoost regression model.

### 3 N-Beats for Wind Speed Forecasting

N-Beats stands for neural basis expansion analysis for interpretable time series forecasting and is a deep neural architecture specifically suited for univariate as well as multivariate time series forecasting. Its architecture is based on forward and backward residual links and consists of very deep stacks of fully connected layers. These stacks of neural networks are called “beats” which are highly capable of capturing both short as well as long-term dependencies in a time series data. Each beat in the architecture consists of a pair of feed forward network (one for trend and seasonality

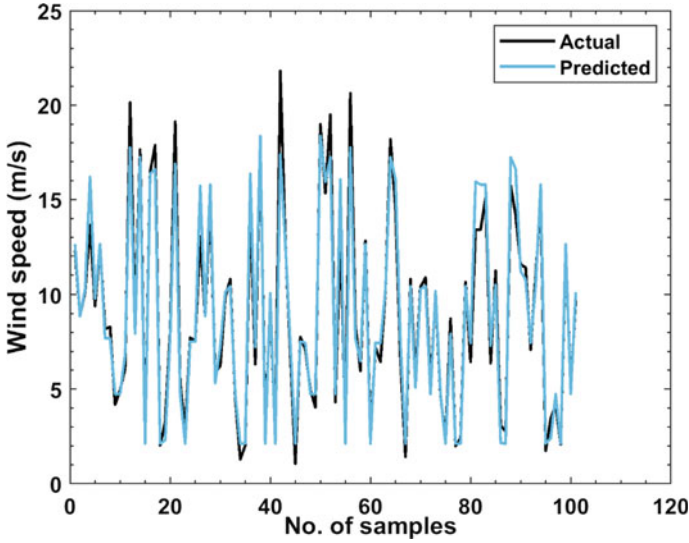


Fig. 4 Prediction of wind speed using trained AdaBoost regression learner

each). The output of these beats is combined subsequently to obtain the forecast of the time series data. N-Beats is a flexible model that can handle a variety of different time series characteristics, such as multiple seasonalities, non-stationarity, and missing data [15]. Figure 5 shows the architecture of the N-Beats in two different blocks. The left block is the basic building block with fork architecture. It receives the time series data (say:  $x_t$ ) as input and outputs two vectors ( $\hat{x}_t$  and  $\hat{y}_t$ ).  $\hat{y}_t$  is the block forward forecast for a given length of time series data, whereas  $\hat{x}_t$  is the best estimate of  $x$ , which is also known as backcast. Next, the residual principle is used to stack a number of layers together which results in an expressive model with good generalization capabilities for time series forecasting.

Considering this, in the present manuscript, N-Beats is used to forecast the wind speed using the previous 100 values of the wind speed data. While training the N-Beats model, the input and output chunk lengths are kept as 25 and 15, respectively.

The model is trained for 500 epochs, and the random state is set to 15. For forecasting the model, 100 recent data points of wind speed are used. Out of which, 50 data points are used for training, whereas the remaining 50 are used as the validation set. The trained model is used to forecast the wind speed as shown in Fig. 6. It is observed that actual and forecasted values follow the almost same trend with a mean absolute error of 0.29. The training loss is found to be  $7.15 \times 10^{-7}$ , whereas the validation loss is found to be  $6.35 \times 10^{-6}$ . N-Beats is also noted to be quite fast in training with an iteration rate of 4.63. It can be observed that forecasted values do follow the actual values closely with some exceptions. Initially, the deviation is observed to be higher and settles down to minimal values as the forecast continues.

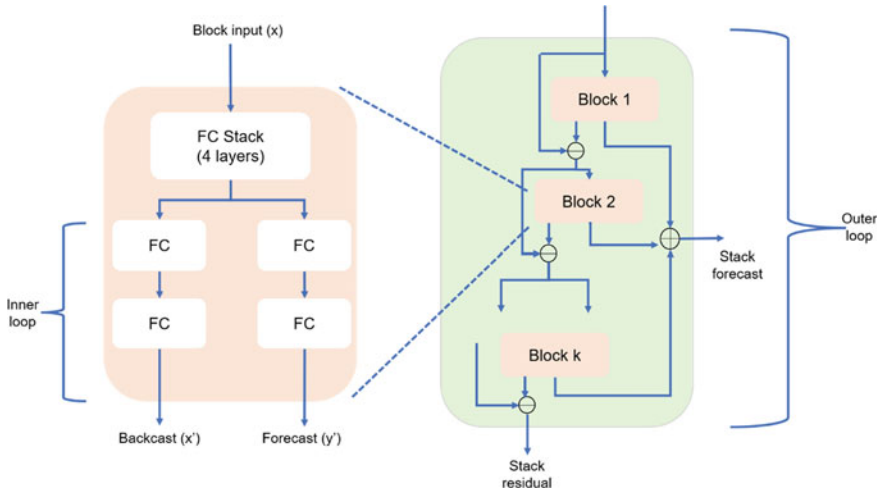


Fig. 5 Architecture of N-beats

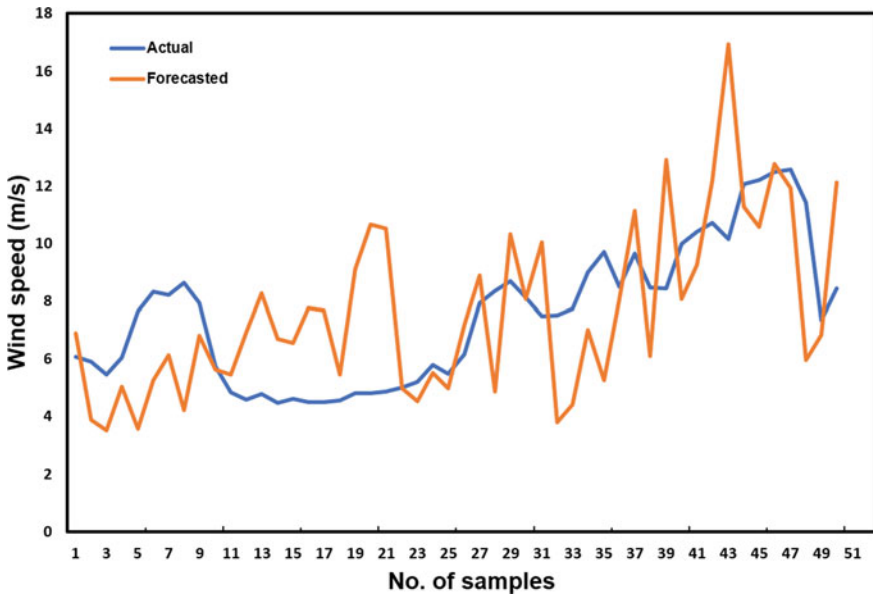


Fig. 6 Wind speed forecasting and their deviation from test data using N-Beats

## 4 Conclusions

The present manuscript describes methodologies for wind speed prediction as well as forecasting using time series forecasting method. The key conclusions of this study are listed below:

- i. Wind speed predictions can be efficiently performed using boosting algorithm-based regression learners, XGBoost and AdaBoost.
- ii. It is found that mean absolute error of the XGBoost is 0.945, whereas it is 0.733 for AdaBoost. Thus, AdaBoost is found to be more accurate in prediction whereas XGBoost is relatively faster than former.
- iii. N-Beats with an input chunk length of 25 and output chunk length of 15 is successfully used to forecast the wind speed with a mean absolute error of 0.29. The training and validation losses are in the range of  $10^{-6}$  and  $10^{-7}$ , respectively.

## References

1. Wang X, Guo P, Huang X (2011) A review of wind power forecasting models. *Energy Proc* 12:770–778
2. Cortez P, Rocha M, Neves J (2004) Evolving time series forecasting ARMA models. *J Heuris* 10:415–429
3. Zhang GP (2003) Time series forecasting using a hybrid ARIMA and neural network model. *Neurocomputing* 50:159–175
4. Prakash J, Miglani A, Kankar PK (2022) Internal leakage detection in hydraulic pump using model-agnostic feature ranking and ensemble classifiers. *J Comput Inform Sci Eng* 23(4):1–41
5. Prakash J, Kankar PK, Miglani A (2021) Internal leakage detection in a hydraulic pump using exhaustive feature selection and ensemble learning. In: 2021 international conference on maintenance and intelligent asset management (ICMIAM). IEEE, pp 1–6
6. Prakash J, Kankar PK (2021) Determining the working behaviour of hydraulic system using support vector machine. In: *Advances in systems engineering: select proceedings of NSC 2019*. Springer Singapore, Singapore, pp 781–791
7. Prakash J, Kankar PK, Miglani A (2021) Monitoring the degradation in the Switching behavior of a hydraulic valve using recurrence quantification analysis and fractal dimensions. *J Comput Inform Sci Eng* 21(6):061010-1–061010-9
8. Kankar PK, Sharma SC, Harsha SP (2011) Fault diagnosis of ball bearings using machine learning methods. *Expert Syst Appl* 38(3):1876–1886
9. Harsha SP, Nataraj C, Kankar PK (2006) The effect of ball waviness on nonlinear vibration associated with rolling element bearings. *Int J Acoust Vib* 11(2):56–66
10. Ranawat NS, Prakash J, Miglani A, Kankar PK (2023) Performance evaluation of LSTM and Bi-LSTM using non-convolutional features for blockage detection in centrifugal pump. *Eng Appl Artif Intell* 122:106092
11. Reference to a website: <https://www.kaggle.com/datasets/berkerisen/wind-turbine-scada-dataset>
12. Chen T, He T, Benesty M, Khotilovich V, Tang Y, Cho H, Zhou T (2015) Xgboost: extreme gradient boosting. R package version 0.4-2, vol 1, no 4, pp 1–4
13. Prakash J, Kankar PK (2020) Health prediction of hydraulic cooling circuit using deep neural network with ensemble feature ranking technique. *Measurement* 151:107225

14. Solomatine DP, Shrestha DL (2004) AdaBoost. RT: a boosting algorithm for regression problems. In: 2004 IEEE international joint conference on neural networks (IEEE Cat. No. 04CH37541), vol 2. IEEE, pp 1163–1168
15. Oreshkin BN, Carпов D, Chapados N, Bengio Y (2019) N-BEATS: neural basis expansion analysis for interpretable time series forecasting. arXiv preprint [arXiv:1905.10437](https://arxiv.org/abs/1905.10437)

# Effect of Turbulence Parameters on Alongwind Response of Tall Rectangular Buildings



Naveen Kwatra and Abhay Gupta

**Abstract** Alongwind and acrosswind response of tall rectangular buildings have attracted the attention of researchers in the last 50 years or so resulting in many useful findings. In order to get a deeper insight into the phenomenon related to tall building aerodynamics, experimental investigations on the model of a 240 m high rectangular multi-storey building with plan dimensions [width ( $b$ )  $\times$  depth ( $D$ )] 24 m  $\times$  48 m ( $b/D = 2.0$ ) and  $H/\sqrt{bD} = 7.07$  have been carried out to study its response in two types of terrains, viz. city outskirts ( $\alpha = 0.18$ ) and city-centre ( $\alpha = 0.30$ ). The response of the model has also been studied in three grid generated flow conditions, to investigate the effect of ‘turbulence’ parameters. The results reported particularly bring out the effect of flow parameters like Turbulence Intensity ‘ $I_u$ ’ and Integral Length Scale ‘ $L_{ux}$ ’, on the building response.

**Keywords** Tall building  $\cdot$  Turbulence Intensity  $\cdot$  Alongwind response  $\cdot$  Acrosswind response

## 1 Introduction

The computation of alongwind response of a variety of tall structures is often carried out by using the method proposed by Davenport [2] for slender line-like structures, though the method by its very concept does not intend to cover the lack of correlation across the width of a structure. Furthermore, as a measure of simplification, the method considers the wind velocity spectrum to be invariant over the building height. The interpretation of theoretical results thus requires taking cognizance of these factors.

---

N. Kwatra (✉)

Department of Civil Engineering, Thapar Institute of Engineering & Technology, Patiala, Punjab, India

e-mail: [nkwatra@thapar.edu](mailto:nkwatra@thapar.edu)

A. Gupta

Skeleton Consultants Pvt. Ltd., Noida 201301, India

On the other hand, the results from wind tunnel tests need to be modified to account for dissimilarities in the similitude requirements, which, in particular, arise from the difficulty in achieving the desired turbulence and eddy size (scale) characteristics in a wind tunnel. These two parameters—the turbulence intensity ' $I_u$ ' and the integral length scale ' $L_{ux}$ ' (of turbulence) have a major effect on the dynamic response of the structure [5]. Similar effects have been studied on stream wise pressures and effects of Intensity and Scale of Turbulence have been reported by Li and Melbourne [4], Hu and Li [3] and Aly [1]. In the present study, these have been varied to a wider extent using five different flow conditions and their effect has been examined. In studying their effect, the approach of Saathoff and Melbourne [5] and that of Sathapathy [6] has been used, in which a joint parameter,  $I_u * (b/L_{ux})^2$ , is defined, and the non-dimensionalized displacement response, with respect to  $L_{ux}$ , is plotted as a function of this joint parameter. ' $b$ ' in the expression is the width of structure normal to the wind. A large number of cases have been studied in the boundary layer wind tunnel, and typical results are reported in this paper.

## 2 The Building Studied

### 2.1 The Prototype

The prototype building selected is described by the following parameters:

- Height,  $h$  and Plan Dimensions = 240 m × 24 m × 48 m
- Aspect ratio in plan ( $D/b$ ) = 2.0
- Vertical Aspect Ratio ( $h/\sqrt{bD}$ ) = 7.07
- Bulk density = 190 kg/m<sup>3</sup>
- Natural Periods of Vibration = 5.20s (long after body) (in Fundamental modes) 6.25s (short after body)
- Damping as % of critical value = 1.5% (in either direction)
- Slenderness ratios ( $h/b$  and  $h/D$ ) = 10 and 5.

### 2.2 The Model

A stick type 2-degrees of freedom aero elastic model of the building made to 1:400 scale has been used in the study. The model was placed in two orientations for determination of characteristics, one in LAB orientation and the other in SAB orientation, and characteristics in longitudinal, i.e. stream wise and in transverse, i.e. perpendicular to wind direction were determined. Helical springs were used to simulate the dynamic characteristics. The bulk density as well as damping ratio of the prototype to the model is unity. The model was designed for a frequency ratio of 0.01 and a velocity ratio of 4.0, while the mass and stiffness ratios achieved were  $64 \times 10^6$  and

**Table 1** Summary of various scaling parameters

Parameter	Notation	Scaling requirement	Ratio	Remarks
Length ratio	$L_r$	$L_p/L_m$	400	Adopted
Bulk density ratio	$\rho_{br}$	$\rho_{bp}/\rho_{bm}$	1.0	Adopted
Damping ratio	$\xi_r$	$\xi_p/\xi_m$	1.0	Adopted
Frequency ratio	$n_r$	$n_p/n_m$	0.01	Assumed
Mass ratio	$M_r$	$L_r^3 * \rho_{br}$	$64 \times 10^6$	Derived
Velocity ratio	$V_r$	$L_r * n_r$	4.0	Derived
Stiffness ratio	$K_r$	$L_r * V_r^2 * \rho_{br}$	$64 \times 10^2$	Derived
Acceleration ratio	$a_r$	$L_r * n_r^2$	0.04	Derived

$64 \times 10^2$ , respectively. The acceleration ratio was 0.04. With a length scale ratio of 400, the building model measured 60 mm  $\times$  120 mm  $\times$  600 mm. The displacement responses are simply related by the geometrical length scale (Table 1).

### 3 Flow Characteristics

As stated earlier, the response of isolated model has been studied in five different flow conditions. These comprise two types of turbulent shear flows (boundary layer) and three types of uniform turbulent flows (grid generated). A low turbulence sub-urban flow condition has been targeted with power-law coefficient  $\alpha = 0.18$  and another more rough urban flow condition where  $\alpha = 0.30$  has been the target value. In order to study the effect of scale of the turbulence, bi-planar grids have been used in the upstream zone. The flow conditions and flow characteristics are summarized in Table 2. Displacements at the top have been recorded through strain-gauge mounted leaf spring transducers and the accelerations have been monitored by piezo-resistive accelerometers, mounted at top, in both alongwind and acrosswind directions. Two hot-wire probes have also been used, one for the incident flow and the other for the wake flow measurements.

### 4 Experimental Programme

The aero elastic model has been placed in the wind tunnel, first with its narrow side facing the wind, i.e. in long afterbody orientation (LAB) and then with its broader face normal to flow, i.e. in short afterbody orientation (SAB). Dynamic characteristics of the model have been established from free vibration records (Fig. 1).

Mean wind speed at the test section has been controlled through a variable eddy current control 'Dynodrive' mechanism. Fan speed has been varied between 300 and



**Table 2** Summary of devices used for various flow conditions and flow characteristics obtained

Flow conditions	BLT1	BLT2	BPG1	BPG2	BPG3
Type of flow	Boundary layer flow	Boundary layer flow	Grid generated flow	Grid generated flow	Grid generated flow
$\alpha$	0.18	0.30	–	–	–
$L_{ux}$	12 cm	24 cm	6 cm	9 cm	18 cm
$I_u$ (%)	4–17	6–21	8.0	9.0	11–18
$L_{ux}/b$	2.0	4.0	1.0	1.5	3.0

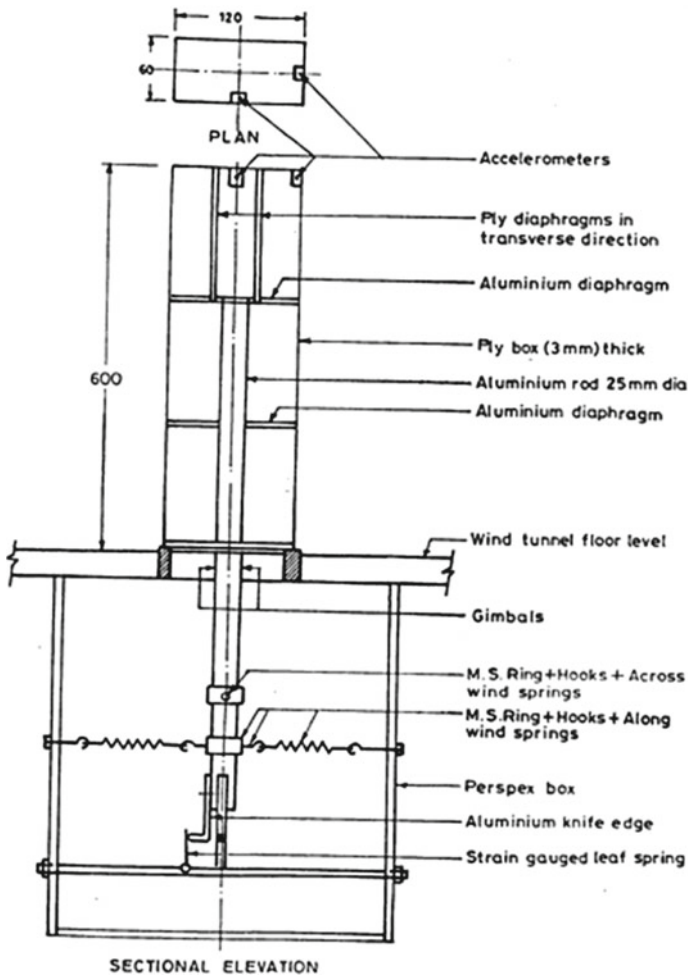


**Fig. 1** Schematic of aero elastic model

950 rpm, which correspond to mean wind speeds of 5–18 m/s in the test section. On full scale, considering a velocity scale of 4.0, this is equivalent to 20–72 m/s (or 72–260 km/h), which covers almost the entire practical range of wind speeds for significant wind effects. Corresponding reduced velocity is worked out as below

$$\text{Reduced Velocity, } RV = \frac{V_h}{n_o * b}$$

where  $V_h$  = mean wind speed near top of the model.

$n_o$  = fundamental frequency in respective direction, viz. alongwind or acrosswind.

$b$  = dimension perpendicular to the mean wind.

Thus a wind speed of 10 m/s would correspond to a reduced velocity of  $\{10/(19.2 \times 0.06)\}$ , i.e. 8.68 for alongwind response, and  $\{10/(16.0 \times 0.06)\}$ , i.e. 10.41 for a crosswind response, in the LAB orientation. In the short afterbody orientation, 10 m/s will yield reduced velocity of 5.37 for alongwind response and 4.34 for acrosswind response.

For reduced velocities between 4 and 16, the model responses have been recorded at 250 Hz for a period of 12 s, while the flow fluctuations are recorded at 1.0 kHz over a period of 8 s. The time histories of these response signals (voltage signals converted to corresponding physical quantity) served as the basic data for further processing. Each data has been repeated once to ensure reproducibility. From each of the response time history records, the mean, maximum positive, maximum negative, RMS, variance, positive and negative peaks, and peak factors have been computed.

## 5 Effect of Turbulence Parameters

The two important turbulence parameters which affect the response are turbulence intensity ( $I_u$ ) and turbulence length scale ( $L_{ux}$ ). In the present study, five different flow conditions have been investigated which yield different values of  $I_u$  and  $L_{ux}$  at the test section. Corresponding to each of the five flow conditions, the model response has been studied at different reduced velocities.

Saathoff and Melbourne [5] have drawn the conclusion that "Mean pressure distributions are strongly dependent on  $I_u$  but are not significantly affected by  $L_{ux}/b$ . Fluctuating pressures, on the other hand, depend on both  $I_u$  and  $L_{ux}/b$ . Pressure fluctuations near separation correlate reasonably well with the parameter,  $I_u(L_{ux}/b)^{0.15}$ , except when  $L_{ux}/b \gg 1.0''$ . Similar inferences were drawn in Li and Melbourne [4] using  $I_u(L_{ux}/b)^{0.40}$ . Sathapathy [6] has used a parameter  $I_u(b/L_{ux})^2 \equiv I_u(L_{ux}/b)^{0.50}$  to study the effect of turbulence parameters.

Here, the variations of Mean alongwind displacement (ALDSP), RMS alongwind displacement (ALDSP) and RMS acrosswind displacement (ACDSP) are studied with changes in the turbulence parameters of the approach flow. For this

study, plots of 'normalized response' versus  $I_u(b/L_{ux})^2$  have been prepared. For non-dimensionalizing the response, in a particular flow field, the respective length scale is used, e.g. mean and rms ALDSP and rms ACDSP in BLT1 are non-dimensionalized with respect to the turbulence length scale in BLT1. These are presented in Fig. 2. Following are the salient results:

- (i) The displacements for different wind speeds show a well-defined relationship with parameter  $I_u(b/L_{ux})^2$ . Generally, the alongwind response increases with increasing values of  $I_u(b/L_{ux})^2$ .

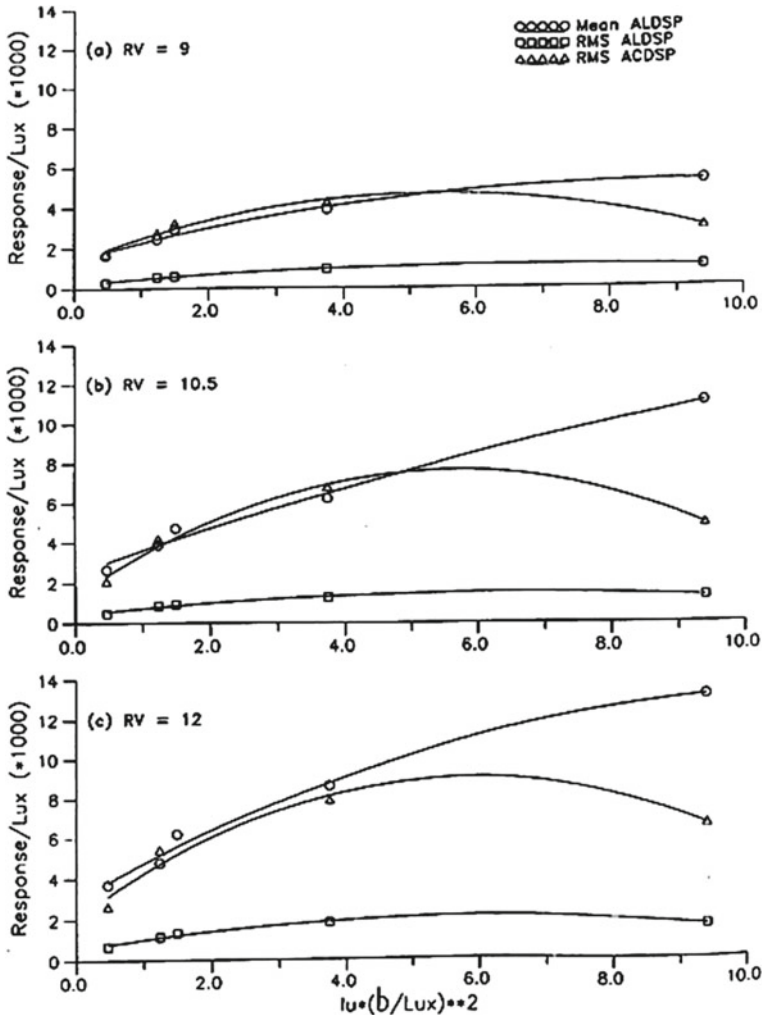


Fig. 2 Variation of response/ $L_{ux}$  with  $I_u(b/L_{ux})^2$ —LAB

- (ii) However, in acrosswind direction, there exists a value of  $I_u(b/L_{ux})^2$ , beyond which the response reduces. This is common for all speeds.

## 6 Effect of Integral Length Scale of Turbulence ( $L_{ux}$ )

The difference between the values predicted on the basis of experimental wind tunnel studies and those computed using Davenport's theory arises partly due to the choice of the value of parameter  $L$ , the characteristic eddy length scale. Computed values of RMS response are not significantly affected by varying  $L$  from 1200 m (as chosen by Davenport) to as low as 300 m, as shown by Fig. 3. However, since the scales measured in the wind tunnel were between 10 and 25 cm which correspond to prototype values between 40 and 100 m, the response gets lowered by about 40%, refer Fig. 3.

## 7 Effect of Turbulence Intensity ( $I_u$ )

The RMS response is a direct effect of the turbulent velocity fluctuations in the longitudinal direction, i.e. the longitudinal turbulence intensities, which are rather low in our study compared to the values assumed by Davenport and are 50% of the field values in upper 2/3rd to half height of building. This is expected to lower down the observed RMS along wind response, though not quantified.

## 8 A New Generalisation Approach

The wind induced response of a typical tall building is mainly derived from wind as well as structural parameters. Intensity and scale of turbulence in the incident wind stream are important parameters as far as mean and RMS response are concerned. With little variation in these parameters, response values change. In the above section, the response has been presented as a function of a joint turbulence parameters  $I_u(b/L_{ux})^2$ . Further, an attempt has also been made to normalize the non-dimensionalized response by the value 'Response/ $L_{ux}$ ' corresponding to  $I_u(b/L_{ux})^2 = 5.0$ . This is observed to yield a very interesting plot. In this representation the curves for various wind speeds for reduced velocities of 9.0, 10.5 and 12.0 merged into a single curve (Fig. 4) for the Mean alongwind displacement, RMS alongwind displacement and RMS acrosswind displacement responses. Such a converged plot, irrespective of the wind speed, may be very much useful for further interpretations where independently turbulence intensity and scales might be different than this study, but the joint parameter lies in the range studied and presented here.

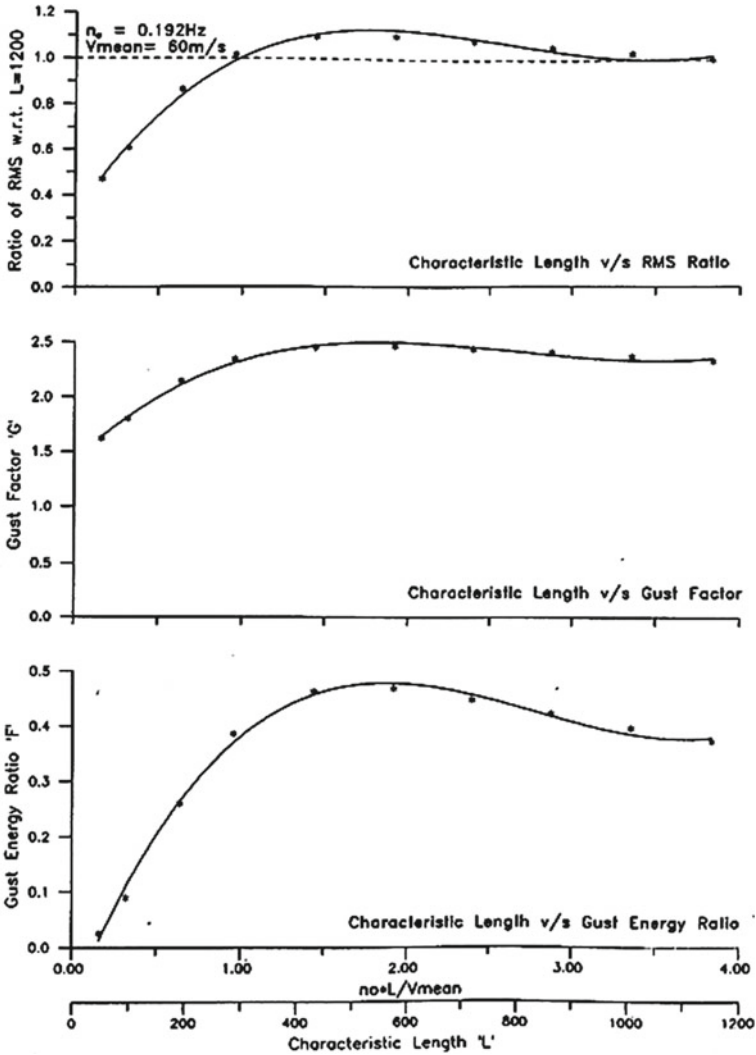


Fig. 3 Effect of characteristic length parameter 'L' on RMS alongwind response

## 9 Conclusions

1. Wind tunnel tests on an aero elastic model of a tall building yield lower values of the alongwind response as the Integral) Length Scale of turbulence generated in the tests may be much smaller than required.

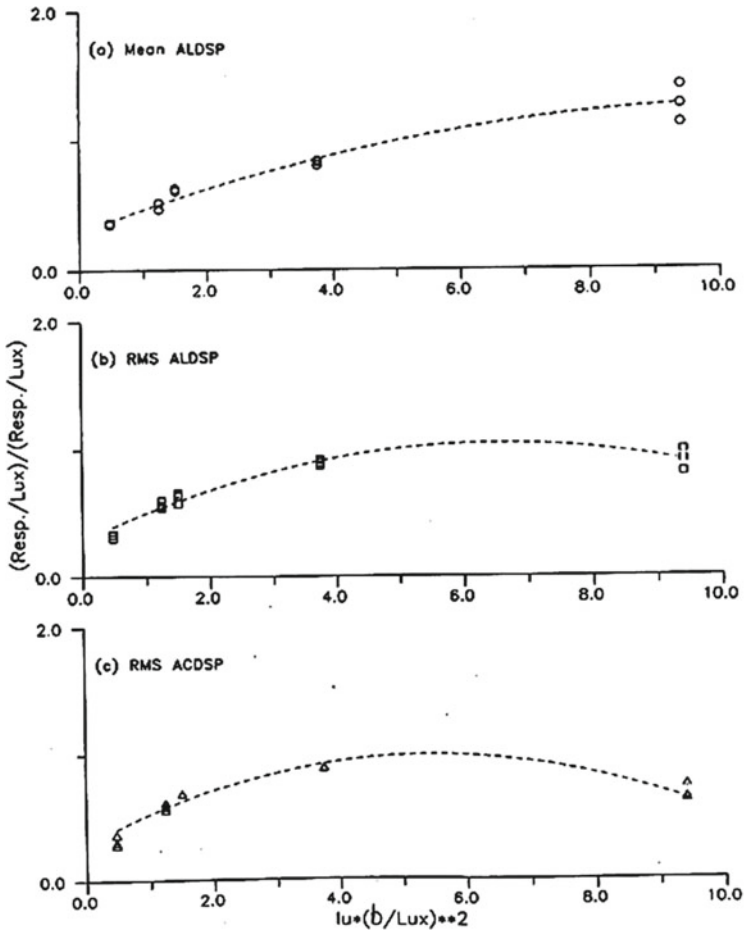


Fig. 4 Normalized response versus  $I_u * (b/L_{ux})^2$  relationship (combined for different wind speeds)

2. The along wind response is seen to increase monotonically with increase in the value of  $\{I_u * (b/L_{ux})^2\}$ . Thus correction for eddy size represented by length scale  $L_{ux}$  should be applied in addition to that for loss of correlation with wind pressures over the width of structure.
3. From the normalized response curves developed, it is possible to interpret the response of a tall rectangular building situated in a wind environment of turbulence characteristics ( $I_u$  and  $L_{ux}$ ) other than the ones in which measurements are made.

## References

1. Aly AM (2014) Influence of turbulence, orientation, and site configuration on the response of buildings to extreme wind. *Sci World J* 2014:1–15
2. Davenport AG (1962) The response of slender line-like structures to a gusty wind. *Proc ICE Lond* 23:389–408
3. Gang H, Li QS (2012) The effects of freestream turbulence on wind-induced responses of tall buildings. In: *The seventh international colloquium on bluff body aerodynamics and applications (BBAA7)*. Shanghai, China
4. Li QS, Melbourne WH (1999) Turbulence effects on surface pressures of rectangular cylinders. *Wind Struct* 2(4):253–266
5. Saathoff PJ, Melbourne WH (1987) Free stream turbulence and wind tunnel blockage effects on stream wise surface pressures. *J Wind Eng Ind Aerodyn* 26(3):353–370
6. Sathapathy B (1980) Turbulence effects on drag of three dimensional bodies in mid stream. Ph.D. Thesis, University of Roorkee, Roorkee, India

# Wind Pattern and Dispersion in a T-Intersection Street Canyon



S. K. Udupi, R. Rao, S. Mahesh, C. Tiwari, L. Singh, and S. J. Pal

**Abstract** Each year there has been a steady rise in vehicles plying on roads leading to an increase in roadside pollution. The condition is grimmer in urban sectors and metro cities. The dispersion of vehicular pollution is essential for the health of pedestrians and nearby societies. Factors like street canyon geometry and meteorological conditions play a significant role in dispersing pollution. One of a typical urban road settings includes a T-intersection canyon having buildings alongside it. The current work attempts to numerically study the wind pattern in the proximity of a T-intersection street configuration. The study investigates the effect of incoming wind velocities and building aspect ratio on the turbulence levels and flow zones adjoining the street canyon. It is observed that the flow regime for the configuration when the ratio of building height and street is one is skimming, while the bulk flow does not enter the canyon. The changes in the configuration lead to variations in the formation of distinct vortexes that are stable and isolated. The analysis of velocity profiles shows sharp gradients at the tip of the building but tends to decrease slowly away from the ground.

**Keywords** T-intersection · Wind patterns · Pollution dispersion

## 1 Introduction

The concern around the decreasing air quality especially in an urban environment is growing with each passing year [1]. The vehicular pollution is directly impacting the health of roadside pedestrians and adjoining societies. There are harmful gases and particulate emissions distributed vertically as well as horizontally having uneven

---

S. K. Udupi · R. Rao · S. Mahesh · C. Tiwari · S. J. Pal  
NIT Surathkal, Mangalore, India  
e-mail: [sjpal@nitk.edu.in](mailto:sjpal@nitk.edu.in)

L. Singh (✉)  
IIT Jammu, Jammu, India  
e-mail: [lakhvinder.singh@iitjammu.ac.in](mailto:lakhvinder.singh@iitjammu.ac.in)

© The Author(s), under exclusive license to Springer Nature Singapore Pte Ltd. 2024  
S. G. Rajasekharan et al. (eds.), *Proceedings of the 9th National Conference on Wind Engineering*, Lecture Notes in Mechanical Engineering,  
[https://doi.org/10.1007/978-981-99-4183-4\\_8](https://doi.org/10.1007/978-981-99-4183-4_8)



gradients and then there are cavities that act as pollution traps [2]. A timely dispersion of vehicular pollution becomes an essential guideline while designing a new urban space. However, the prediction of pollution dispersion becomes a complex task due to the spatial and temporal changes from spot to spot due to factors such as meteorological conditions, presence of obstacles, to name a few.

A typical urban environment consists of tall buildings on both sides of a street. However, the manner in which the streets and building align in an urban space varies from one junction to another. Some of the street junctions could be T-interactions, Y-interaction, acute angle, staggered, multiple, etc. Likewise, the building types can vary a lot. Few of the scenarios are uniform buildings on both sides of the roads, non-uniform building on both sides of the roads, buildings on single side of the roads, etc. Due to large combinations of street canyon, building configurations, and wind conditions, the study of dispersion is complex and general guidelines fails to account for accurate pollution dispersion.

A study by Costabile and Allegrini [3] measures concentration level of pollutants such as  $\text{NO}_x$ ,  $\text{NO}_2$ ,  $\text{NO}$ , benzene, toluene, and xylene (BTX) at the ground and the roof top of a building in the urban area of Suzhou (China). The building is 22 m high, while the road is 40 m wide. The measurements at the roof top account for pollutant being carried by the wind from the upstream pollutant sources. However, the study found that the concentration of pollutants at the ground was higher than rooftop. Thus, it indicates that the ground wind dynamics and pollutants levels are dominant factors for pollution dispersion. Ming et al. [4] studied dispersion in a non-uniform urban street canyon under the influence of traffic tidal flow for wind direction perpendicular to the street. The author found that there is a higher concentration of pollutants at the pedestrian breathing height when the intensity of source is greater in the leeward side than windward side.

The present study is an attempt to understand the wind pattern distribution in street canyon. A T-intersection is considered for the study. The dispersion of pollutants is largely influenced by the fluid dynamics in the proximity of buildings whereby the movement of particles is dominated by convection. The study aims to find the dynamics of fluid flow and the identification of pollution traps. The traps are represented by the recirculation regions. Further, the pressure distribution in the proximity of street canyon adds information pertaining to the formation of pollution traps.

## 2 Computational Methodology

The dispersion of pollution is significantly influenced by the meteorological conditions. The study of wind patterns around a building can be understood by solving and analyzing Navier–Stokes equation. The advancements in the modeling techniques and with enough proof of the reliability of the results, obtaining solutions using numerical techniques, has become a standard practice. The current study solves

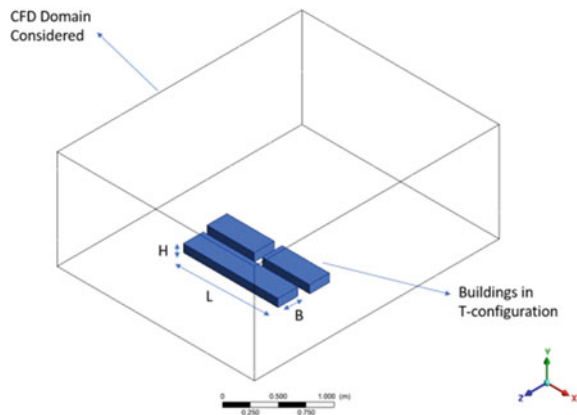
Reynolds-averaged Navier–Stokes equations to obtain flow field. The terms associated with Reynolds stresses are modeled using a two-equation approach. In the current study, RNG  $k-\varepsilon$  turbulence model is selected and preferred over other turbulence models [5, 6].

## 2.1 Computational Domain and Grid Settings

The 3D computational domain consist of a T-intersection street canyon and the surrounding area of interest as shown in Fig. 1. The three-dimensional model has a building height ( $H$ ) of 100 mm, street canyon width of 100 mm. The three buildings are placed in a way to form a T-intersection. Domain dimensions are  $43.5H \times 12.5H \times 25H$  ( $L \times H \times W$ ). The dimensions are scaled in the ratio of 1:100. The volumetric mesh has polyhedral cells which are smaller and denser closer to the walls of the buildings and coarser away from the walls. The minimum orthogonal quality is 0.2 and the maximum aspect ratio is 16.

In order to ensure that the results of the study are not dependent on the grid size, a grid independence is performed by repeating a portion of the study with different grid characteristics and ensuring invariance. The grid independence study was performed by varying the size and therefore number of cells, varying the parameter of cell count by a factor of two, and a factor of half. The velocity profiles at location  $x = 0H$  (center of the T-intersection) were obtained for three grids (G\_1, G\_2, and G\_3) having cell count as  $0.6 \times 10^6$ ,  $0.3 \times 10^6$ , and  $0.15 \times 10^6$ , respectively. The velocity profiles of G\_1 and G\_2 are nearly identical with maximum variation of 5% as shown in Fig. 2. Thus, G\_2 having cell count of  $0.3 \times 10^6$  was selected for obtaining numerical results.

**Fig. 1** Computational domain of the T-intersection



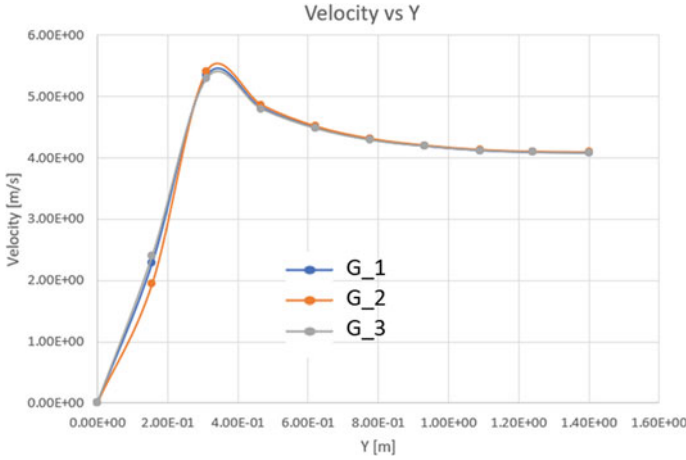


Fig. 2 Comparison of velocity profiles along y-axis on z–y plane at center of T-intersection

### 2.2 Governing Equations

The pollutant dispersion is dominated by the flow pattern. The governing equations of fluid flow are based on conservation of mass and momentum and given by Eqs. (1, 2, 3),

$$\text{div } \rho v = 0 \tag{1}$$

$$\nabla \cdot \rho v v = -\nabla p + \nabla \cdot (\tau) \tag{2}$$

$$\rho C_p v \cdot \nabla T = k_{\text{eff}} \nabla^2 T \tag{3}$$

where  $k_{\text{eff}}$  is the effective conductivity and represents the sum of material thermal conductivity and turbulent thermal conductivity, and also,  $v$ ,  $\rho$ , and  $T$  represent Reynolds-averaged velocity, density, and temperature, respectively.

### 2.3 Boundary Conditions

At the inlet of the domain, a fixed value of velocity (4 m/s) and ambient temperature (300 K) is assigned. At walls of the buildings, no-slip shear condition with the stationary wall is applied. Along with that, the standard roughness model and zero value of heat flux and heat generation rate are also employed. At the plenum, ‘Pressure Inlet’ B.C. is applied at a fixed value (here, zero) of gauge pressure and total

temperature as 300 K across its surface, and at the outlet of the domain, 'Pressure Outlet' is assigned with zero-gauge pressure and backflow temperature as 300 K.

The discretization of domain is primarily obtained by structured polyhedral mesh. The  $y^+$  in all the grids is in the range of 30–100, so the first cell is placed adjacent to viscous sublayer. Thus, wall functions are used to obtain the effect of near wall region. The governing equations are integrated over the computational domain using the finite volume method (FVM). A second-order upwind scheme has been utilized to obtain the gradients as it also improves the accuracy of the solution compared to first-order schemes. The pressure velocity coupling is done through SIMPLE algorithm. Further, the convergence criteria for all the variables are set to  $10^{-6}$ .

### 3 Results and Discussion

The understanding of the flow field in the street canyon of a T-intersection is necessary for knowing the potential pollution traps. The incoming wind conditions plays a dominant role in the development of the flow field. The results which obtain through simulations discuss the flow distribution in a T-intersection street canyon.

#### 3.1 Velocity and Pressure Distribution

The numerical results are obtained for a condition when the wind approaches at normal to the T-intersection. The speed of incoming wind is 4 m/s, while a plug wind approach is assumed. The incoming turbulence is assumed to be 5% of the mean wind speed. To understand the wind patterns, specific planes of interest are selected. Figure 3 shows the flow field distribution on plane  $z-y$  at  $x = 0H$  (middle of the T-intersection), whereas Fig. 4 shows the vector plot.

It can be seen that a strong shear flow is formed at the rooftop level and a clockwise rotating vortex is formed in the downstream street canyons. The contours of blue region show the flow recirculation and represents vortex formation. The flow regime is skimming; this means that the bulk flow does not enter the canyon and is characterized by a stable and isolated vortex at the street canyon. The bulk flow after separating at the windward side of the building does not reattach to the street. The tendency to form a big vortex at the street canyon raises concerns of formation of pollution traps.

The velocity on the street is of the order of 2 m/s that is nearly half of the ambient conditions of wind speed. At the same time on inspecting the vectors, it can be seen that the direction of wind speed on the street is opposite to the ambient wind. The exposure of wind to pedestrian is completely different to the one who is upstream of the T-intersection street canyon. However, to aid pollution dispersion, the presence of wind is important, while the direction of wind is rather not that important.

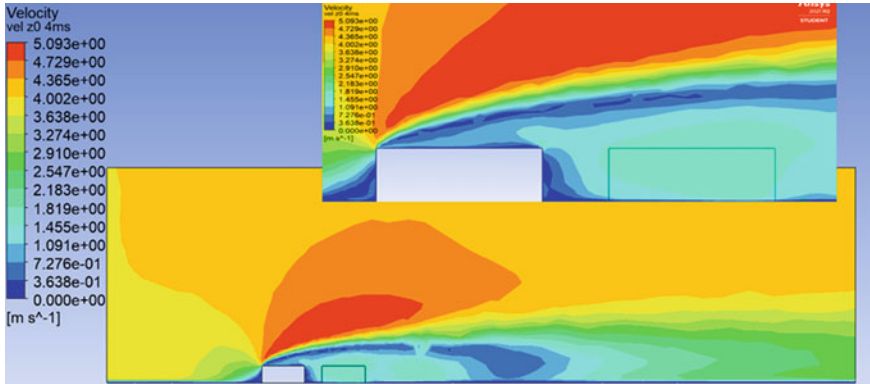


Fig. 3 Velocity contour on  $z$ - $y$  plane at  $x = 0H$  and a zoomed-in view

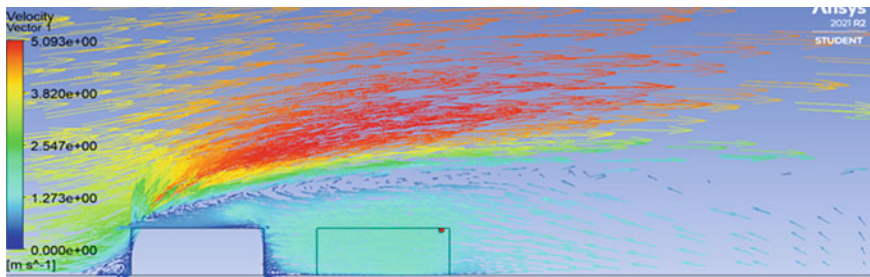


Fig. 4 Velocity vector plot on  $z$ - $y$  plane at  $x = 0H$

Figure 5 shows the pressure distribution at the middle plane ( $x = 0H$ ). The first separation point can be seen to be present at the windward face of the windward side building near to the ground. The flow velocity at this point is almost to zero and hence can be considered as a stagnation point. The second separation point can be seen to be present at the windward corner of the windward side building. A small eddy is formed at the rooftop due to the separation. The third separation point is generated when the flow moves further into the street canyon along the leeward side of the first building. Another small eddy is formed at the leeward corner of the windward side building. The formation of these small eddies are characterized by high spinning and low pressure at the core as seen in the pressure contour. While the large clockwise rotating eddy is expanding in the street canyon, another stream of flow entrains from the rooftop of the second building and enters the street canyon along the windward side of the second building. The core region of recirculation where low pressure is formed is a concern for the dispersion of pollution.

The flow field at planes  $x = 3H, 6H, -3H,$  and  $-6H$  is shown in Fig. 6. It can be seen that the flow distribution on the opposite planes such as at  $3H$  and  $-3H$  is quite similar but with minor changes. Likewise, the contours' distribution at  $6H$  and  $-6H$

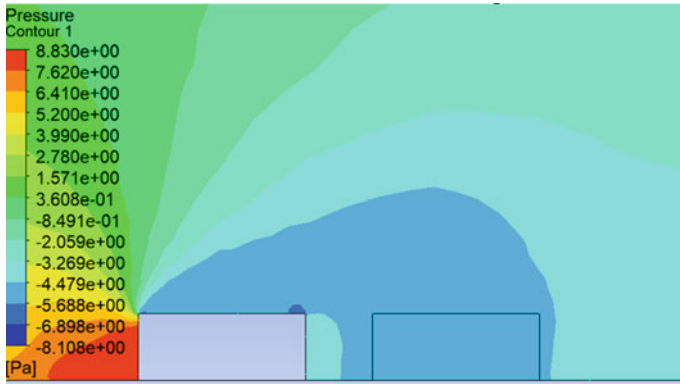


Fig. 5 Pressure distribution on  $z$ - $y$  plane at  $x = 0H$

is nearly similar. It can be said that there is a degree of asymmetry that is present in the flow although the domain is symmetric. The separation bubble position decreases in both length and height as suction near the leading edge increases in all five planes along the length of the building. Higher speed flow also emerges along the separated shear layer above the leading edge.

The flow distribution on the street shows that the velocity is wind is nearly nonexistence with values of wind speed nearing to zero at the pedestrian nose level. It is more predominant at  $6H$  and  $-6H$  planes.

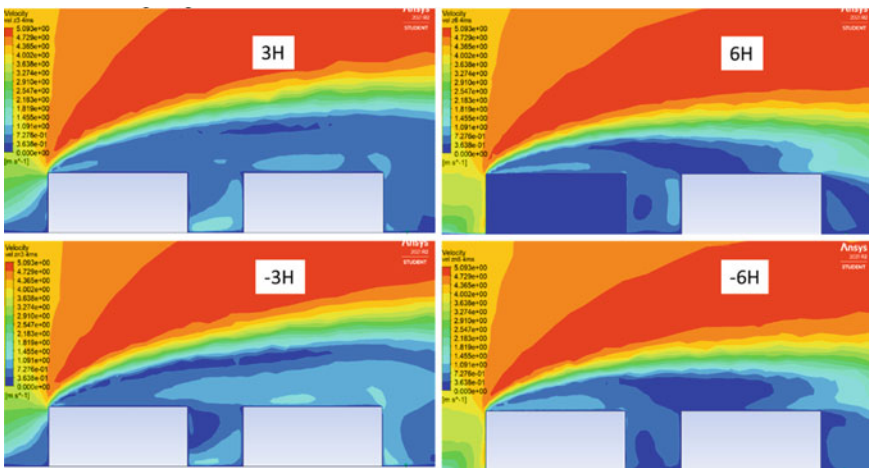
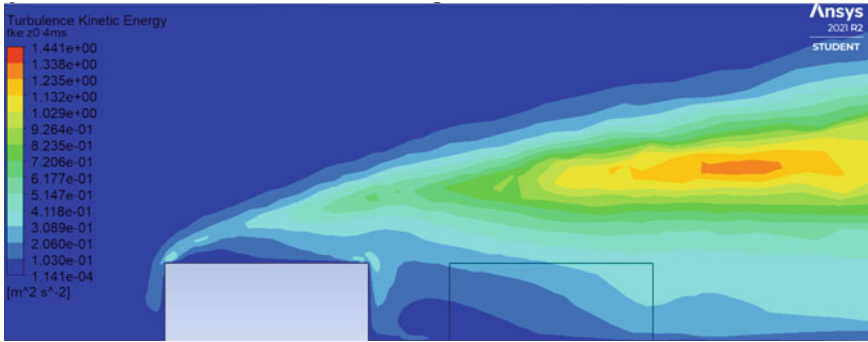


Fig. 6 Velocity contour plots at four parallel planes on both sides of the street canyon



**Fig. 7** Contours of turbulence kinetic energy on  $z$ - $y$  plane at  $x = 0H$

### 3.2 Turbulence

The characteristics flow Reynolds number based on building height of 100 mm and inlet velocity of 4 m/s makes it a turbulent flow. However, the obstacles in the form of building in the path of wind generate additional turbulence. The presence of turbulent flow in a flow field indicates the transfer of energy from the mean flow to eddy formation and then dissipation in the form of viscous heating. The presence of any amount of turbulence kinetic energy in the computational domain indicates strong mean velocity gradients in the flow. The gradients represent fast changing velocities in all the directions. Figure 7 shows the contour of the generation of turbulence kinetic energy (TKE). The separation and reattachment sites linked with the corner of the upwind and downwind building downstream of the street canyon are where the TKE is lowest. In accordance with the findings of Bernardino et al. [7] and Cheng and Liu [8], large variance zones are produced above the building top and a shear layer coming from the upwind building's corner along the length of the structure, the phenomena is seen on all five planes.

## 4 Conclusion

A T-intersection street canyon's wind flow is modeled, and the distribution of velocity, pressure, and turbulent kinetic energy in understanding dispersion of pollutants is presented. Using the RNG  $k$ -turbulence model, a scenario when the wind approach the building at 90-degree angle having an inlet wind speed of 4 m/s is solved numerically. The incoming velocity profile is assumed to be plug flow. The simulations shows that the layout (where the ratio of building height to building width is 1) has a skimming flow regime, which is characterized by a stable and isolated vortex at the center of the street canyon and prevents bulk flow from entering the canyon. Near the building's roof, the velocity profile sharply rises and then gradually falls away from

the ground. There is a drastic increase in the velocity and turbulent kinetic energy at twice the building height.

## References

1. Vardoulakis S, Fisher BEA, Pericleous K, Gonzalez-Flesca N (2003) Modelling air quality in street canyons: a review. *Atmos Environ* 37(2):155–182
2. Dobre A, Arnold SJ, Smalley RJ, Boddy JWD, Barlow JF, Tomlin AS, Belcher SE (2005) Flow field measurements in the proximity of an urban intersection in London, UK. *Atmos Environ* 39(26):4647–4657
3. Costabile F, Allegrini I (2007) Measurements and analyses of nitrogen oxides and ozone in the yard and on the roof of a street-canyon in Suzhou. *Atmos Environ* 41(31):6637–6647
4. Ming T, Fang W, Peng C, Cai C, De Richter R, Ahmadi MH, Wen Y (2018) Impacts of traffic tidal flow on pollutant dispersion in a non-uniform urban street canyon. *Atmosphere* 9(3):82
5. Salim SM, Ong KC (2013) Performance of RANS, URANS and LES in the prediction of airflow and pollutant dispersion. In: IAENG transactions on engineering technologies: special edition of the world congress on engineering and computer science 2011. Springer Netherlands, pp 263–274
6. Kim JJ, Baik JJ (2004) A numerical study of the effects of ambient wind direction on flow and dispersion in urban street canyons using the RNG  $k-\epsilon$  turbulence model. *Atmos Environ* 38(19):3039–3048
7. Bernardino AD, Monti P, Leuzzi G, Querzoli G (2015) On the effect of the aspect ratio on flow and turbulence over a two-dimensional street canyon. *Int J Environ Pollut* 58(1–2):27–38
8. Cheng WC, Liu CH (2011) Large-eddy simulation of turbulent transports in urban street canyons in different thermal stabilities. *J Wind Eng Ind Aerodyn* 99(4):434–442



# Errors and Uncertainties in Simulation of Unsteady Viscous Flow Over a Circular Cylinder at $Re = 48$



Aravind Seeni, Dhanish Ahamed, Chinni Maadesh, Harish Adishwar, and Ayshwarya Mahadevan

**Abstract** The flow past a circular cylinder is an important problem of investigation in applications such as structural engineering (bridge structures, tall buildings, chimneys, etc.) and aeronautical engineering (bluff body aerodynamics). CFD based on the Finite Volume Method implemented in the solver *Fluent* shows that aerodynamic coefficients while predicted with remarkable accuracy for the two-dimensional, steady, viscous flow past a circular cylinder case revealed errors or discrepancies in the prediction of von Kármán vortex street (and associated periodicity of lift and drag) at the Reynolds number range of 46–48. The reason for the discrepancy is investigated with a focus on predicting von Kármán vortex street at  $Re$  of 48, by making different grid design considerations, viz., varying the blockage ratio, upstream distance of cylinder to inlet, downstream distance from cylinder to outlet boundary and mesh element size parameter. Although the known flow characteristics such as fluidic unsteadiness, force oscillations and vortex shedding predictions existent at this  $Re$  were never predicted, the mean drag coefficient was predicted in all cases with high degree of accuracy. The recommendations and conclusions drawn from the study could now be applied to different fluid flow problems. The earlier obtained results provided guidance on how to find solutions to different applications as well as perform more complex fluid flow simulations effectively, with minimal error and effort.

**Keywords** Errors · Uncertainties · Unsteady flow · Viscous flow · Circular cylinder · Low Reynolds number

---

A. Seeni (✉) · D. Ahamed · C. Maadesh · H. Adishwar · A. Mahadevan  
Department of Aeronautical Engineering, Rajalakshmi Engineering College, Thandalam,  
Chennai, Tamilnadu 602105, India  
e-mail: [aravindseeni.s@rajalakshmi.edu.in](mailto:aravindseeni.s@rajalakshmi.edu.in)

© The Author(s), under exclusive license to Springer Nature Singapore Pte Ltd. 2024  
S. G. Rajasekharan et al. (eds.), *Proceedings of the 9th National Conference on Wind Engineering*, Lecture Notes in Mechanical Engineering,  
[https://doi.org/10.1007/978-981-99-4183-4\\_9](https://doi.org/10.1007/978-981-99-4183-4_9)

## 1 Introduction

Computational Fluid Dynamics (CFD) is expected to continuously play an instrumental role in the design and analysis of systems and components in various fields of engineering [1]. It is a known fact that results generated through CFD are not exact solutions or true results of the problem in question. Rather, the results are numerical approximations to governing equations in the presence of errors and uncertainties. According to AIAA, an *error* is defined as “A recognizable deficiency in any phase or activity of modeling and simulation that is not due to lack of knowledge”. Similarly, *uncertainty* can be defined as “A potential deficiency in any phase or activity of the modeling process that is due to the lack of knowledge” [2].

Prior research works on the topic of error and uncertainty estimation in CFD are [3–6]. In this paper, it is assumed that the various factors affecting the grid generation process such as wall blockage ratio, distance from cylinder to inlet, distance from cylinder to outlet boundary and mesh element size have profound impacts on computational accuracy and introduce discretization errors. This also leads to variation in prediction of the critical Reynolds number from which vortex shedding due to wake instability arises. So far, to the author’s knowledge, a study on errors and uncertainties in the simulation of unsteady flow over a circular cylinder due to the aforementioned factors at low Reynolds number of 48 is not yet available in literature. Therefore, in this paper, a comprehensive investigation is performed on the effect of blockage ratio, distance from cylinder to inlet, distance from cylinder to outlet boundary, mesh element size parameter on flow pattern, aerodynamic characteristics such as lift coefficient ( $C_l$ ), drag coefficient ( $C_d$ ) and Strouhal number ( $St$ ) of the cylinder at Reynolds number of 48. The errors generated from the computations are listed and discussed which would allow the user to select a particular grid with the smallest error. The lessons learnt can then be applied to other flow problems.

## 2 Problem Statement

The Finite Volume Method (FVM) is employed for simulating flow for the problem of flow past a single, stationary, rigid cylinder. The Finite Volume code built within the solver Fluent is used to simulate the steady flow. It is found that numerical computations are in perfect agreement with real-world experiments for steady case. It is not yet clear whether the same model can be applied to simulate unsteady flows. Henceforth, computations are performed for unsteady flow for different  $Re$  in the critical  $Re$  range with the same method, mesh and solver settings used for steady case.

Unsteady simulations are first performed on the mesh used for the steady case with a time step size ( $\Delta t$ ) of 0.1. The vorticity results for five  $Re$  cases considered, namely, 46, 47, 48, 58 and 59 are analyzed. It is observed from the vorticity contours that there is no periodic vortex shedding predicted at about  $Re = 47$  as stated in [7], no onset of

unsteadiness, as expected, for critical  $Re \approx 46$ , as described in [8] or for  $Re = 46.8$  as reported in [9]. It is further observed that the onset of fluidic unsteadiness and lift periodicity is predicted only at  $Re = 59$ . For  $Re \approx 48$ , after initial perturbations, the lift coefficient gradually reaches to steady state. Therefore, it is concluded that the model which correctly predicts steady flow characteristics is unable to correctly predict the same for unsteady flow, at  $Re$  corresponding to real-world experimental predictions. The cause of this problem requires careful examination of different parameters.

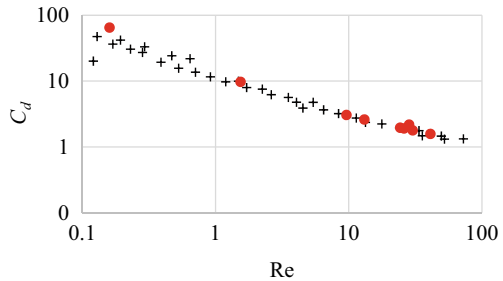
Research on the effects of blockage ratio, upstream distance of cylinder to inlet, downstream distance from cylinder to outlet boundary and mesh element size parameter on the unsteady flow characteristics from circular cylinder simulation have not yet been investigated, according to the author’s knowledge. Therefore, a detailed study of the aforementioned effects on the vorticity, aerodynamic forces and Strouhal number is performed here.

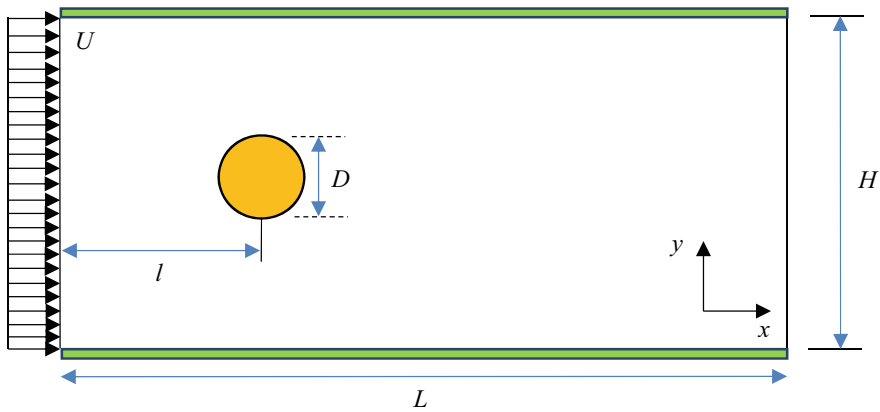
### 3 Numerical Setup

Figure 1 provides the schematic of the flow problem considered in this paper. To study the effect of different blockage ratios ( $H/D$ ), simulations are conducted for flow past a single cylinder with  $Re$  at 48, cylinder location from inlet ratio ( $l/D$ ) as 25 and channel length ( $L/D$ ) as 100, fixed. The primary aim of this research is the prediction of von Kármán vortex street at  $Re = 48$ . The channel length ratio ( $L/D$ ) of 100 is set in accordance with the recommendations of Heil et al. [8] which states the limits of boundary where unsteadiness starts to occur. The dimensions of cylinder are fixed as 1 diameters ( $D$ ). In all cases, the second-order implicit temporal discretization with time step size ( $\Delta t$ ) of 0.1 is considered. The iteration process is repeated until the residuals fall below  $10^{-4}$ . The grids of resolution in all cases are maintained close to that of the baseline grid consisting of 127,280 nodes and 126,400 elements (Fig. 2).

To study the effect of different upstream distances of cylinder to inlet ( $l/D$ ), simulations are conducted for flow past a single cylinder assuming  $Re = 48$ ,  $H/D$  of 23 and  $L/D$  of 100. Six different upstream distances from inlet to cylinder ( $l/D$ ) cases—25, 18, 15, 12, 9 and 6, are considered. The time step size in all cases is assumed to be 0.1.

**Fig. 1** Numerical and experimental comparison for drag coefficient for different Reynolds number





**Fig. 2** Schematic of the flow past single circular cylinder confined in a channel

The residual convergence criterion is fixed as  $10^{-4}$ . Six different grids are assigned. The grids of resolution in all cases are maintained close to that of the baseline grid consisting of 127,280 nodes and 126,400 elements.

In order to study the effect of downstream distance from cylinder to outlet boundary, simulations are conducted for flow past a single cylinder assuming  $Re = 48$ ,  $H/D$  of 23 and  $l/D$  of 11.5. Six different downstream distances from cylinder to outlet boundary ( $L/D$ ) cases—100, 80, 70, 60, 50 and 40, are considered. The time step size in all cases is assumed to be 0.1 and the residual convergence criterion is set to be  $10^{-4}$ . Six different grids are assigned. The resolution of grids in all cases is maintained close to that of the baseline grid consisting of 127,280 nodes and 126,400 elements.

In order to study the effect of mesh element size parameter, simulation is conducted assuming  $Re$  of 48,  $H/D$  at 23,  $l/D$  at 11.5 and  $L/D$  at 100. Five different mesh sizes, with minimum and maximum element sizes or face areas ( $\Delta s$ ) of 0.017, 0.013, 0.0098, 0.0057, 0.0043 and 1.572, 1.04, 0.78, 0.53, 0.39, respectively, are considered. In all cases, the time step size is assumed to be 0.1. The residual convergence criterion is assumed as  $10^{-4}$ .

## 4 Results and Discussion

In this section, the results for the problem are presented in terms of streamlines, vorticity contours and aerodynamic coefficients. The effects of  $H/D$ ,  $l/D$ ,  $L/D$  and  $\Delta s$  on the flow characteristics and aerodynamic forces are investigated. In all the cases, the  $Re$  is fixed at 48 and time step size as 0.1.

### 4.1 Effect of Blockage Ratios

Six different blockage ratio ( $H/D$ ) cases—13, 18, 23, 28, 33 and 38, are investigated in this study. The vorticity contours for confined flow over a circular cylinder at different blockage ratios are presented in Fig. 3. The lift coefficient, drag coefficient of cylinder and Strouhal number results showed that for all blockage ratios, the vorticity contours are symmetric about the top and bottom halves of the cylinder. The fluid unsteadiness in the wake and periodic vortex shedding could not be observed in all cases. The results are therefore inconsistent with earlier obtained results by Norberg [7], Heil et al. [8] and Baranyi and Lewis [9]. Nevertheless, as also in the case of an earlier experimental study by Strykowski and Sreenivasan [10], the natural vortex shedding process could only be observed from  $Re \approx 60$  and not 46. Due to the absence of vortex shedding and the von-Kármán vortex street phenomenon, in all cases, the drag coefficient is seen to be steady. The time history of drag coefficient for Case 3 ( $H/D = 23, l/D = 25, L/D = 100, Re = 48$ ) is shown in Fig. 4. In addition, the lift coefficient is found to be transient for a period of time and converges to the initial steady-state solution. The Strouhal number is found to be zero. The trend in the lift coefficient, drag coefficient and Strouhal number observed is a consequence of the absence of vortex shedding.

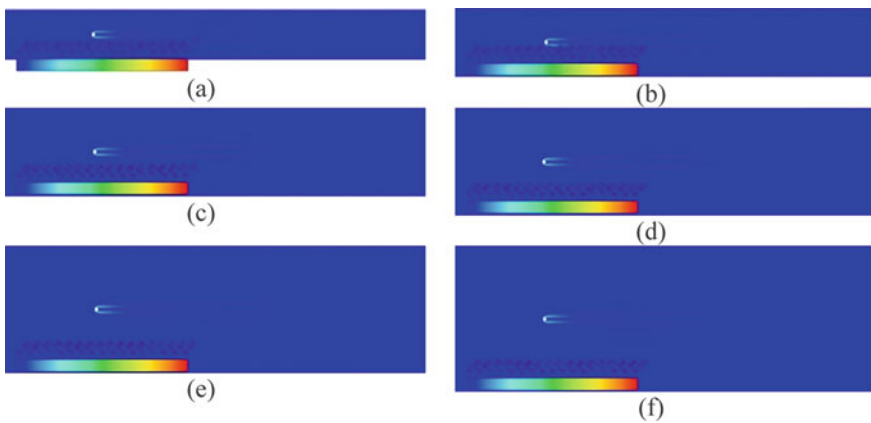


**Fig. 3** Vorticity contours for different blockage ratios ( $l/d = 25, L/D = 100, Re = 48$ ). **a**  $H/D = 13$ , **b**  $H/D = 18$ , **c**  $H/D = 23$ , **d**  $H/D = 28$ , **e**  $H/D = 33$ , **f**  $H/D = 38$

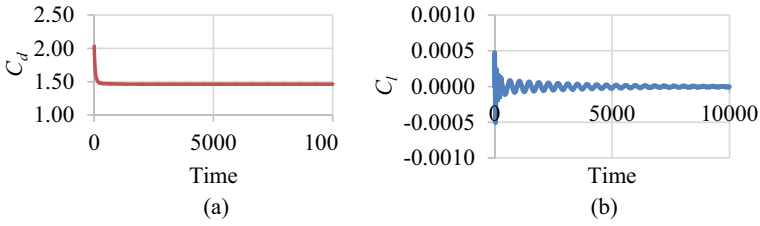


**Fig. 4** Time history of **a** drag coefficient, **b** lift coefficient for  $H/D = 23$  ( $l/D = 25, L/D = 100, Re = 48$ )

### 4.2 Effect of Upstream Distance of Cylinder to Inlet

Six different upstream distances from inlet to cylinder ( $l/D$ ) cases—25, 18, 14, 11.5, 8 and 5, are investigated in this study. The vorticity contours for the different cases are provided in Fig. 5. The lift coefficient, drag coefficient of cylinder and Strouhal number results showed that the vorticity contours are symmetric about the top and bottom halves of the cylinder. It is, therefore, concluded that there is no vortex shedding present in all cases. The drag coefficient is steady and non-periodic. An illustration of time history of drag coefficient for case of  $l/D = 11.5, H/D = 23, L/D = 100$  is shown in Fig. 6. The lift coefficient is found to be transient and converges to the initial steady-state solution due to the absence of vortex shedding. The Strouhal number is found to be zero. The trend in the lift coefficient, drag coefficient and Strouhal number is a result of absence of vortex shedding.

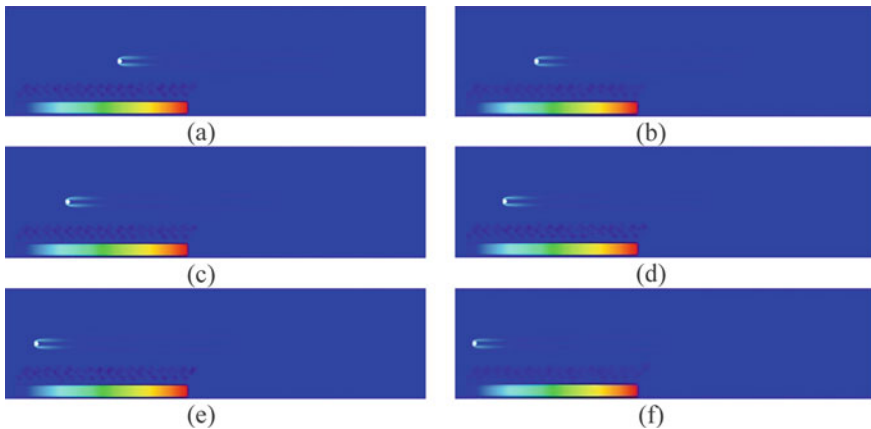


**Fig. 5** Vorticity contours for different upstream distances of cylinder to inlet ( $H/D = 23, L/D = 100, Re = 48$ )

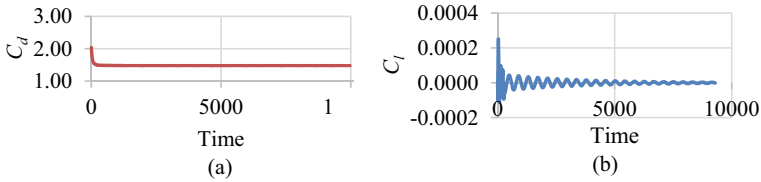


**Fig. 6** Time history of **a** drag coefficient, **b** lift coefficient for  $l/D = 11.5$  ( $H/D = 23$ ,  $L/D = 100$ ,  $Re = 48$ )

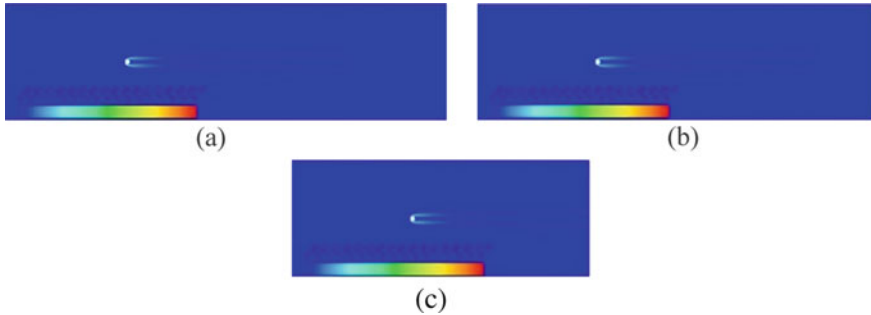


**Fig. 7** Vorticity contours for different downstream distances of cylinder to outlet boundary ( $H/D = 23$ ,  $l/D = 25$ ,  $Re = 48$ ). **a**  $L/D = 100$ , **b**  $L/D = 80$ , **c**  $L/D = 60$ )

### 4.3 Effect of Downstream Distance of Cylinder to Outlet Boundary

Six different downstream distances of cylinder to outlet cases, i.e., the ratio  $L/D$  assumed as 100, 80 and 60, are investigated in this study. The vorticity contours for the different cases are given in Fig. 7. The lift coefficient, drag coefficient of cylinder and Strouhal number results showed that the vorticity contours are symmetric and there is no vortex shedding. The drag coefficient is seen to be steady and non-periodic. An illustration of time history of drag coefficient for case of  $L/D = 80$ ,  $H/D = 23$ ,  $l/D = 25$  is shown in Fig. 8. The lift coefficient after some transience converges to a steady-state solution. The magnitude of lift coefficient and Strouhal number is zero for all cases due to the absence of vortex shedding.

### 4.4 Effect of Element Size Parameter

Six different downstream distances of cylinder to outlet cases, i.e., the ratio  $L/D$  assumed as 100, 80 and 60, are investigated in this study. The vorticity contours for the different cases are given in Fig. 9. The lift coefficient, drag coefficient of cylinder

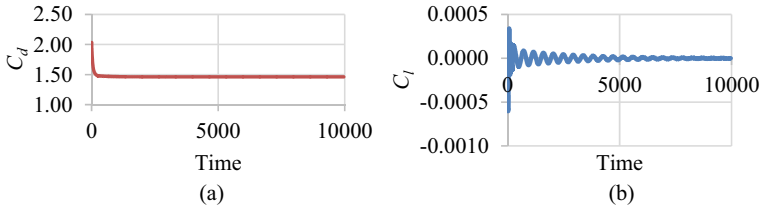


**Fig. 8** Time history of **a** drag coefficient, **b** lift coefficient for  $L/D = 80$  ( $H/D = 23$ ,  $L/D = 25$ ,  $Re = 48$ )

and Strouhal number results showed that the variation in element size parameter did not have any impact on the vortex shedding as well as the lift and drag characteristics. The vorticity contours are symmetric and the drag coefficient is steady. An illustration of time history of drag coefficient for case of  $\Delta s_{min}$  and  $\Delta s_{max}$  of  $0.0098 \text{ m}^2$  and  $0.78 \text{ m}^2$ , respectively,  $H/D = 23$ ,  $L/D = 25$ ,  $L/D = 100$ , is shown in Fig. 10, as an example. The lift coefficient after some duration of transience converges to steady state. The Strouhal number is zero for all cases due to the absence of vortex shedding.

The absence of unsteadiness and vortex shedding in all different cases from this study shows that the model using FVM (second-order) may not perform well and be accurate enough to simulate practical real-world physics of flows, especially for  $Re = 48$ . Nevertheless, it is observed that FVM may perform well at a different  $Re$  condition. In the experimental study by Strykowski and Sreenivasan [10], vortex shedding is captured only from  $Re$  of 60. The numerical error due to discretization can now be quantified. The error ( $E$ ) in each of the cases is calculated using the below formula (Eq. 1) and is summarized in Table 1.

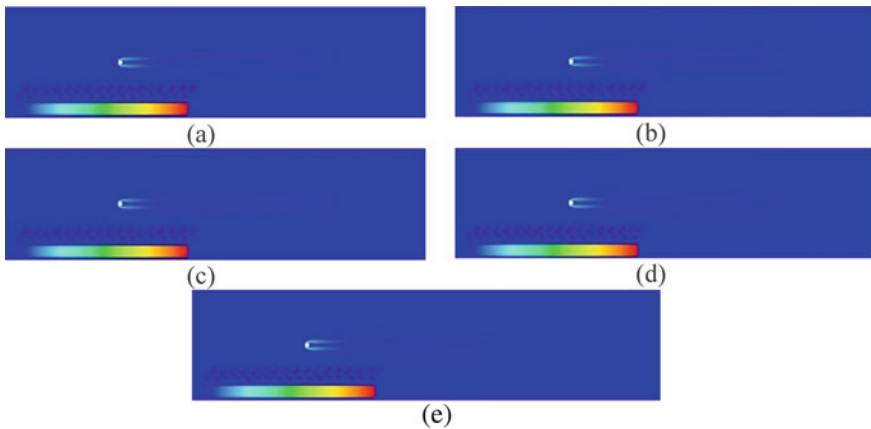


**Fig. 9** Vorticity contours for different element sizes ( $H/D = 23$ ,  $L/D = 25$ ,  $L/D = 100$ ,  $Re = 48$ ). **a** 34,000 elements, 34,440 nodes, **b** 72,900 elements, 73,560 nodes, **c** 126,400 elements, 127,280 nodes, **d** 277,200 elements, 278,520 nodes, **e** 486,400 elements, 488,160 nodes



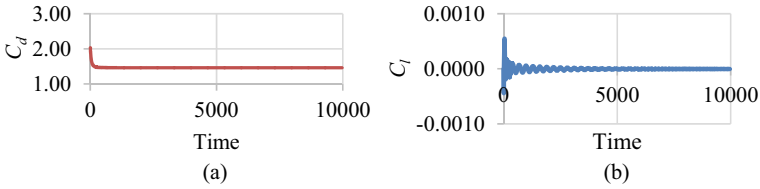


**Fig. 10** Time history of **a** drag coefficient, **b** lift coefficient for mesh element minimum and maximum face areas of 0.0098 and 0.78 m<sup>2</sup>, respectively ( $H/D = 23$ ,  $l/D = 25$ ,  $L/D = 100$ ,  $Re = 48$ )

$$E = \left( \frac{C_{d,mean} - C_{d,exp}}{C_{d,exp}} \right) \times 100 \tag{1}$$

The results in Table 1 show that among all  $H/D$  cases, the grid studied for Case 3 has the lowest error and has the best agreement of  $C_{d,mean}$  with the total  $C_d$  of Hoerner [11]. Furthermore, Table 1 shows that among all  $l/D$  cases, the grid studied for Case 12 has the lowest error and has the best drag coefficient agreement. Table 1 shows that among all  $L/D$  cases, Case 13 has the lowest error and has the best drag

**Table 1** Summary of numerical errors for cases 1–20

Parameter	Case #	Error (%)
$H/D$	Case 1	6.05
	Case 2	2.06
	Case 3	0.12
	Case 4	− 0.96
	Case 5	− 1.62
	Case 6	− 2.04
$l/D$	Case 7	0.12
	Case 8	0.27
	Case 9	0.63
	Case 10	1.19
	Case 11	3.24
	Case 12	8.94
$L/D$	Case 13	0.12
	Case 14	0.13
	Case 15	0.13
$\Delta s$	Case 16	0.17
	Case 17	0.12
	Case 18	0.12
	Case 19	0.18
	Case 20	0.43

agreement. Among all  $\Delta s$  cases, Case 17 and Case 18 have the lowest errors and have the best drag agreement. In such cases, the lowest mesh resolution is selected on account of cost considerations.

## 5 Prediction of Critical Reynolds Number

In this section, the obtained optimum values are used to predict the critical  $Re$  ( $Re_c$ ) for the single circular cylinder. Table 2 compares the lift coefficient, drag coefficient and Strouhal number for different  $Re$ . It is seen that the periodicity in drag and lift is obtained from  $Re = 54$ . Table 3 compares the critical flow parameters,  $Re_c$  and  $St_c$  with results obtained from literature. The results portray a fairly accurate prediction of  $Re_c$  with approximately,  $- 10.0\%$  to  $+ 14.8\%$  difference as compared to other researchers.

**Table 2** Comparisons of lift coefficient, drag coefficient and Strouhal number for predicting critical Reynolds number ( $H/D = 23, l/D = 25, L/D = 100, 73,560$  nodes,  $72,900$  elements)

	$Re$	$C_{d,max}$	$C_{d,min}$	$C_{d,mean}$	$C_l$	$St$
Present study	54	1.4552	1.4535	1.4547	$\pm 0.092$	0.025
Present study	55	1.4516	1.3876	1.4138	$\pm 0.10$	0.032
Baranyi and Lewis [9]	55	–	–	1.4225	–	0.1312

**Table 3** Comparisons of critical Reynolds number and Strouhal number with other studies

Study	Method	$Re_c$	$St_c$	Domain size ( $L/D \times H/D$ )
Berger and Wille [12]	Experiment	50.0	0.12	–
Williamson [13]	Experiment	47.9	0.122	$H/D = 150$
Norberg [7, 14]	Experiment	47.4 ( $\pm 0.5$ )	0.1177	$H/D = 6250$
Gresho [15]	FEM	50.0	0.14	–
Strykowski and Sreenivasan [10]	Experiment	60.0	–	–
Kumar and Mittal [16]	FEM, direct time integration	46.877	0.1168	$100 \times 100$
Kumar and Mittal [16]	FEM, sub-space iteration	47.318	0.1169	$100 \times 100$
Baranyi and Lewis [9]	Finite difference method, vortex cloud	46.8	–	–
Heil et al. [8]	Finite difference method	46	–	–
Present study	2D FVM in Fluent	54	0.025	$100 \times 23$

## 6 Conclusion

Research on errors and uncertainties in simulation of unsteady flow over circular cylinder has been completed. The Finite Volume-based solver Fluent is assessed for computational accuracy in simulating the problem. The effects of blockage ratio, upstream distance of cylinder to inlet, downstream distance from cylinder to outlet boundary and mesh element size parameter on the flow pattern and aerodynamic forces are investigated. The results of the study are summarized below.

1. The von Kármán vortex street was not present at  $Re = 48$  in all the cases, 1–20.
2. The blockage ratio ( $H/D$ ) of 23 provided the best result on drag coefficient with the lowest error of 0.12% under steady condition.
3. The upstream distance of cylinder to inlet ( $l/D$ ) of 25 provided the best result on drag coefficient with the lowest error of 0.12% under steady condition.
4. The downstream distance of cylinder to outlet boundary ( $L/D$ ) of 100 provided the best result on drag coefficient with the lowest error of 0.12% under steady condition.
5. The mesh with 73,560 nodes and 72,900 elements provided the best result on drag coefficient with the lowest error of 0.12% under steady condition.
6. The FVM employed on the optimized mesh with domain of  $H/D = 23$ ,  $l/D = 25$ ,  $L/D = 100$  and consisting of 72,900 elements and 73,560 nodes predicted the onset of vortex shedding at critical  $Re$  of 54 (difference of within  $-10.0\%$  to  $+14.8\%$  compared to earlier studies).

A comprehensive investigation on domain size and mesh size and their influence on the unsteady results for flow past a circular cylinder was performed. From the results, it is inferred that the Finite Volume Method employed in the solver Fluent was unable to predict the von Kármán vortex street at the low  $Re$  of 48. The absence of fluidic unsteadiness and lift/drag periodicity confirms the result. The reason for the discrepancy is attributed to the solver's capability to solve such problems at low  $Re$ . Nevertheless, the results obtained could be used to identify the best grid that provided the least error. The identified optimum domain size and mesh parameters were applied to other fluid flow problems with minimal effort, and the solver's accuracy for simulating such problems was successfully demonstrated. It can be added that the use of additional sources of error contributed by additional solutions of the governing equation (higher-order accuracy solution, lower-order accuracy solution), auxiliary PDE solutions, auxiliary algebraic evaluations and surrogate estimators as stated by Roache [3] should also be investigated in the future.

## References

1. Spalart PR, Venkatakrishnan V (2016) On the role and challenges of CFD in the aerospace industry. *Aeronaut J* 120(1223):209–232
2. AIAA (1998) Guide for the verification and validation of computational fluid dynamics simulations. AIAA Standard G-077-1998
3. Roache PJ (1997) Quantification of uncertainty in computational fluid dynamics. *Annu Rev Fluid Mech* 29(X):123–159
4. Stern F, Wilson RV, Coleman HW, Paterson EG (2001) Comprehensive approach to verification and validation of CFD simulations—Part 1: methodology and procedures. *J Fluids Eng Trans ASME* 123(4):793–802
5. Oberkampf WL, Trucano TG (2002) Verification and validation in computational fluid dynamics. *Prog Aerosp Sci* 38(3):209–272
6. Knupp P, Salari K (2003) Verification of computer codes in computational science and engineering. Chapman & Hall/CRC
7. Norberg C (1994) An experimental investigation of the flow around a circular cylinder: influence of aspect ratio. *J Fluid Mech* 258:287–316
8. Heil M, Rosso J, Hazel AL, Brøns M (2017) Topological fluid mechanics of the formation of the Kármán-vortex street. *J Fluid Mech* 812:199–221
9. Baranyi L, Lewis RI (2006) Comparison of a grid-based CFD method and vortex dynamics predictions of low Reynolds number cylinder flows. *Aeronaut J* 110(1103):63–70
10. Strykowski PJ, Sreenivasan KR (1990) On the formation and suppression of vortex ‘shedding’ at low Reynolds numbers. *J Fluid Mech* 218:71–107
11. Hoerner SF (1965) Fluid-dynamic drag: theoretical, experimental and statistical information. Hoerner Fluid Dynamics, Bakerfield, CA
12. Berger E, Wille R (1972) Periodic flow phenomena. *Annu Rev Fluid Mech* 4(1):313–340
13. Williamson CHK (1989) Oblique and parallel modes of vortex shedding in the wake of a circular cylinder at low Reynolds numbers. *J Fluid Mech* 206:579–627
14. Norberg C (2001) Flow around a circular cylinder: aspects of fluctuating lift. *J Fluids Struct* 15(3):459–469
15. Gresho PM, Chan ST, Lee RL, Upson CD (1984) A modified finite element method for solving the time-dependent, incompressible Navier-Stokes equations. Part 1: theory. *Int J Numer Methods Fluids* 4(6):557–598
16. Kumar B, Mittal S (2006) Prediction of the critical Reynolds number for flow past a circular cylinder. *Comput Methods Appl Mech Eng* 195:6046–6058

# Aerodynamics Analysis of Industrial Wind Turbines



Chinni Maadesh, Dhanish Ahamed, Harish Adishwar,  
Ayshwarya Mahadevan, and Aravind Seeni

**Abstract** Aerodynamic forces are used by all wind turbines to capture wind energy. Lift vector acts normal to the relative wind, whereas drag force acts parallel to the relative wind. The factors taken into account include the swept area of the turbine, the density of air, the wind speed, the aerodynamic efficiency, and the coefficient of power which is directly proportional to blade tip speed. The research demonstrates that the operational aerodynamic characteristics have a direct impact on the power produced, which will encourage researchers to concentrate on the most important aerodynamic factors for developing and manufacturing the next generation of wind turbines. At last, the results are examined whether the flow parameters meet the aerodynamic requirements for the design of industrial wind turbines.

**Keywords** Wind energy · Wind turbine · Airfoil · CFD · Blade geometry

## 1 Introduction

Since wind turbine blades have a high slenderness ratio with a low spanwise velocity component compared to their high streamwise velocity component. A coordinate system can be used to describe the plane that makes up two-dimensional flow. Computational fluid dynamics (CFD) provides solution for problems with fluid flow by using numerical analysis as in [1]. In order to produce electricity, wind power devices, often known as wind turbines, are now used [2]. In practically every area of fluid dynamics, from aircraft propulsion to weather forecasting, computational fluid dynamics has developed from a mathematical curiosity to an indispensable tool. Continuity, the set of Navier–Stokes equations, extra conservation equations, such as those relating to energy or species concentrations, and the numerical solution of these governing equations, which characterize fluid flow, are all included in the term CFD. Since the

---

C. Maadesh · D. Ahamed · H. Adishwar · A. Mahadevan · A. Seeni (✉)  
Department of Aeronautical Engineering, Rajalakshmi Engineering College, Thandalam,  
Chennai, Tamilnadu 602105, India  
e-mail: [aravindseeni.s@rajalakshmi.edu.in](mailto:aravindseeni.s@rajalakshmi.edu.in)

© The Author(s), under exclusive license to Springer Nature Singapore Pte Ltd. 2024  
S. G. Rajasekharan et al. (eds.), *Proceedings of the 9th National Conference on Wind Engineering*, Lecture Notes in Mechanical Engineering,  
[https://doi.org/10.1007/978-981-99-4183-4\\_10](https://doi.org/10.1007/978-981-99-4183-4_10)

invention of the digital computer, computational fluid dynamics has attracted a lot of attention as a burgeoning field from all over the world [3].

## **1.1 Problem Statement**

The research involves the analysis of a set of airfoils and performing Computational Analysis on them and obtaining the parameters such as lift, drag, pressure distribution, temperature distribution, velocity contour, pressure contour,  $C_D$  versus  $C_L$ , power. National Renewable Energy Laboratory (NREL) airfoils are chosen for analysis because they have high capacity to reduce the energy losses that are caused by roughness effect. In Horizontal Axis Wind Turbine (HAWT), the airfoils S809, S812, S813, S814 are chosen for the analysis. Previously, the analysis for such wind turbine has been done wherein the analysis has been done for VAWT with different airfoils. But in this paper, the HAWT is the chosen blade type and four airfoils S809, S812, S813 and S814 are chosen, and they are analyzed based on aerodynamics and performance characteristics. The airfoils S809, S814 have been analyzed in [4]. This paper provides in-depth analysis of HAWT with airfoils S809, S812, S813 and S814. A total of four airfoils have been chosen for comparative study [5]. The analysis is done in QBlade software.

## **2 Methodology**

To perform the analysis, three different airfoils from NREL are chosen and studied. A blade is designed on the criteria of good efficiency and the expected power output. The airfoil chosen is S809, S812, S813 and S814. The efficiency of a wind turbine decreases due to a lot of reasons such as high angle of attack, working hours. The prime objective is to increase the Coefficient of Performance (COP) of the wind turbine. The four airfoils are analyzed for their performance, and the results are shown for the best airfoil and blade design.

### **2.1 Code QBlade**

The software QBlade is used for wind turbine analysis. QBlade is a free program for calculating wind turbines. Designing and simulating the aerodynamics of wind turbine blades are the goal of this software. The user can quickly create unique airfoils and calculate their performance curves using the integration in XFOIL. A graphical user interface in the software helps the user throughout the entire wind turbine design process.

## 2.2 Theory

The wind turbine works primarily on the principle of BEM theory. It is used to determine the precise forces acting locally on a wind turbine or propeller blade. To reduce some of the challenges in computing the induced velocities at the rotor, momentum theory and blade element theory are merged [6]. The idea behind the BEM theory is that forces acting on the rotor can be inferred from the aerodynamic lift and drag on a blade section given using two-dimensional airfoil [7]. Velocity of rotor is found from the below equation:

$$u = (1 - x)u_{\infty}, \quad (1)$$

where  $u_{\infty}$  is the speed of wind and  $x$  is the induction factor.

The maximum theoretical power coefficient is  $C_{p\max} = 0.593$  which is often referred to a Betz limit in designing the shape of the wind turbine blades.

The equations of rotor performance coefficients are given by

$$c_T = 4x(1 - x), \quad (2)$$

$$c_p = 4x(1 - x)^2. \quad (3)$$

Aerodynamic relations involved in designing wind turbine blades.

Equation of lift that is generated during the working of the turbine:

$$L = \frac{1}{2}\rho v^2 S c_L. \quad (4)$$

Equation of lift coefficient:

$$c_L = \frac{2L}{\rho v^2 S}. \quad (5)$$

Drag experienced by the blades:

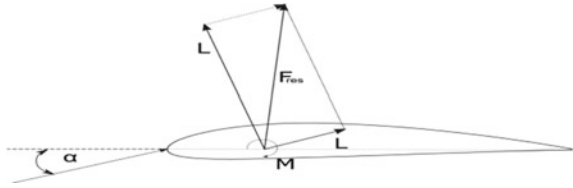
$$D = \frac{1}{2}\rho v^2 S c_D. \quad (6)$$

Equation of drag coefficient (Fig. 1):

$$c_D = \frac{2D}{\rho v^2 s}. \quad (7)$$

Mathematical equations to determine the performance of wind turbine.

**Fig. 1** Diagram of aerodynamic forces acting on an airfoil



Thrust coefficient:

$$C_T = \frac{T}{\rho n^2 D^4} \tag{8}$$

Torque coefficient:

$$C_Q = \frac{Q}{\rho n^2 D^5} \tag{9}$$

Power coefficient:

$$C_P = \frac{P}{\rho n^3 D^5} \tag{10}$$

### 3 Results and Discussions

The four airfoils chosen are compared as given in Table 1.

#### 3.1 Blade Design

The airfoils were chosen and below given is the diagram of all the airfoils (Fig. 2 and Table 2).

**Table 1** Comparison chart of the four airfoils

S. No	Airfoil	$C_{Lmax}$	Design $C_L$	$C_M (L = 0)$	$C_D$	Thickness
1	S809	1.0	0.5	- 0.05	0.04	0.210 c
2	S812	1.2	0.5	- 0.07	0.008	0.210 c
3	S813	1.1	0.5	- 0.07	0.007	0.160 c
4	S814	1.3	0.50	- 0.15	0.012	0.240 c



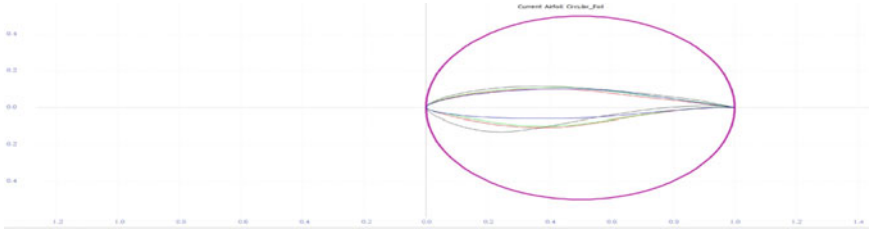


**Fig. 2** Airfoil design

**Table 2** Airfoil design module

S. No	Airfoil	Thickness (%)	At (%)	Camber (%)	At (%)	Points	LE Flap (deg)
1	Circular airfoil	99.99	49.40	0.00	0.40	251	0.00
2	S809	20.99	38.30	0.99	82.30	66	0.00
3	S812	21.00	39.10	1.57	77.10	62	0.00
4	S813	15.99	40.50	2.27	54.40	62	0.00
5	S814	24.15	26.20	3.09	74.50	66	0.00

### 3.2 Airfoil Analysis

The blade is analyzed for different wind speeds and the wind speeds lie between 4 and 10 m/s. Curves of  $C_L$  versus  $\alpha$ ,  $C_D$  versus  $\alpha$ , and  $C_L$  versus  $C_D$  ( $\alpha$  is in degrees) (Figs. 3, 4 and 5).

### 3.3 Turbine Performance Analysis

For the process of analyzing the wind turbine, the plots of performance are obtained for four different wind speeds that are 4, 6, 8, and 10 m/s.

Below given are the plots of power versus TSR ( $\lambda$ ), thrust versus TSR ( $\lambda$ ), and torque versus TSR ( $\lambda$ ).

The performance graphs of all the four airfoils are given in Figs. 6, 7, 8, 9, 10, 11, 12, 13, 14, 15, 16 and 17.

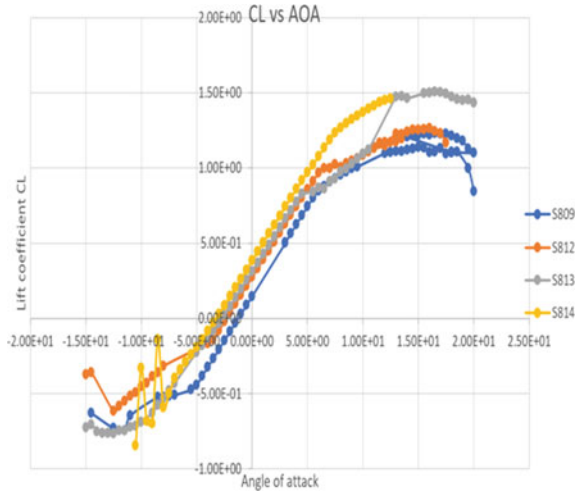


Fig. 3  $C_L$  versus  $\alpha$

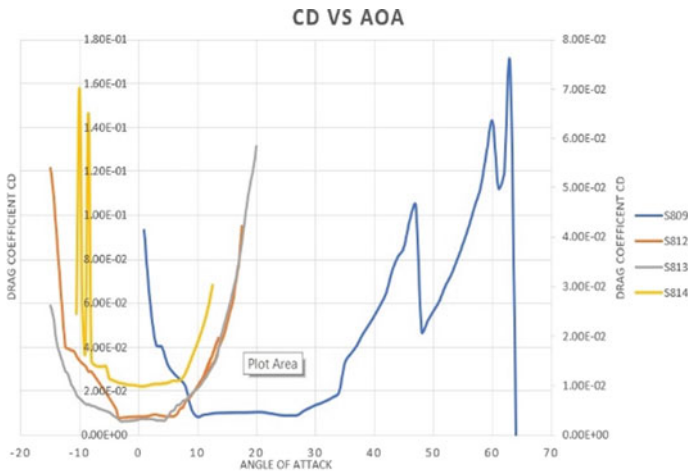


Fig. 4  $C_D$  versus  $\alpha$

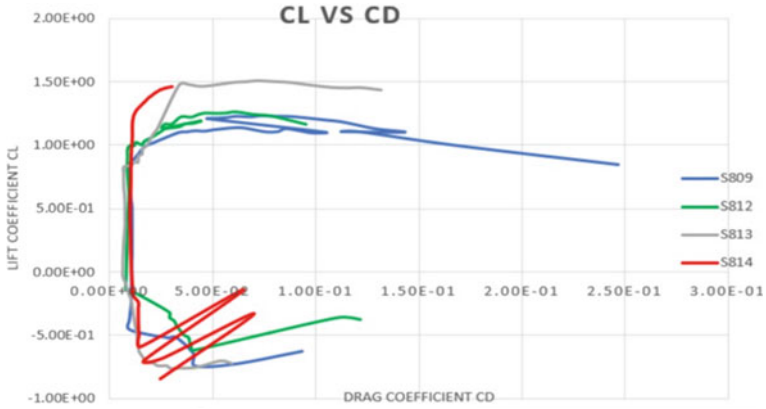


Fig. 5  $C_L$  versus  $C_D$

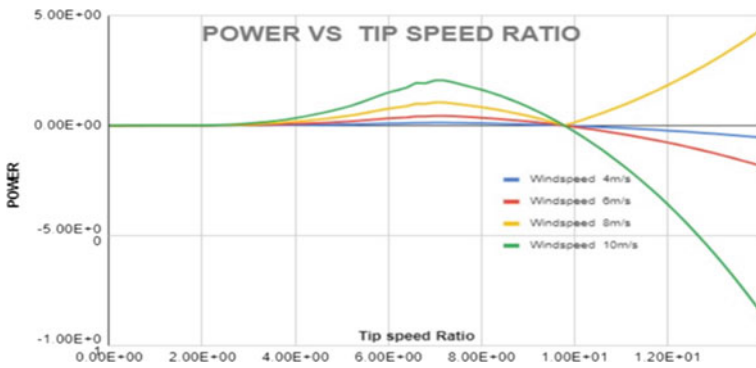


Fig. 6 Power versus  $\lambda$

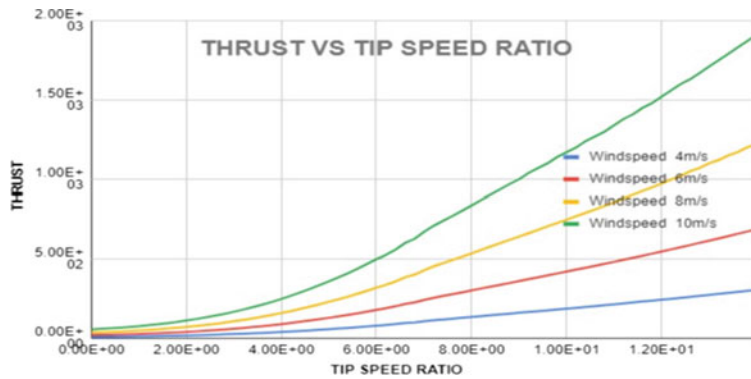


Fig. 7 Thrust versus  $\lambda$

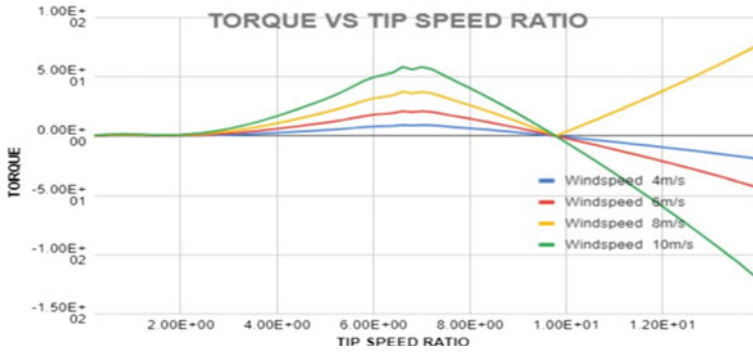


Fig. 8 Torque versus  $\lambda$ .

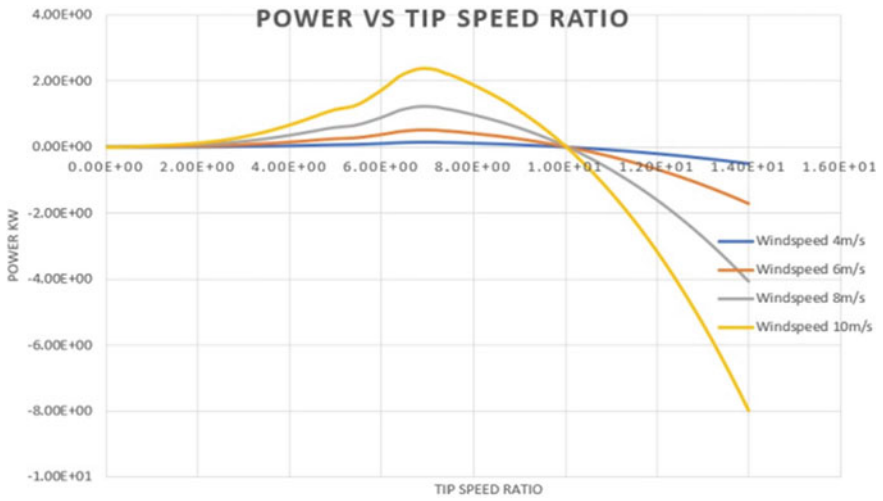


Fig. 9 Power versus  $\lambda$ .

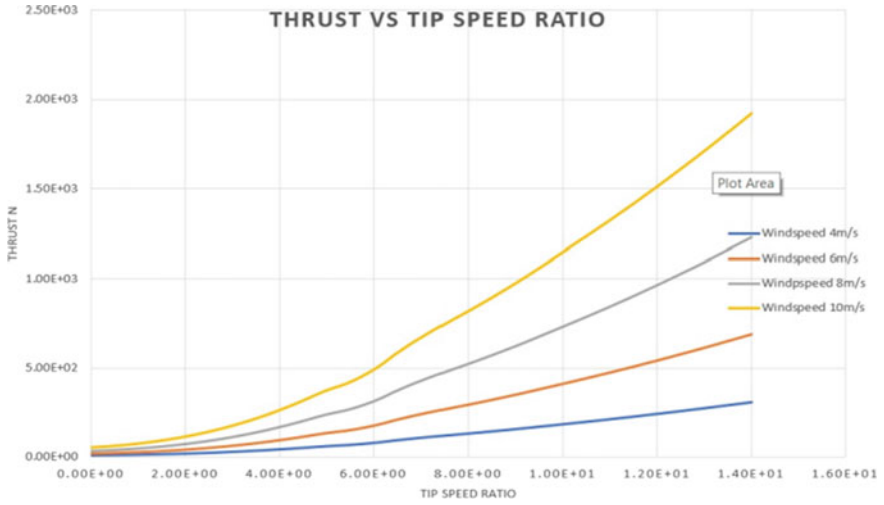


Fig. 10 Thrust versus  $\lambda$ .

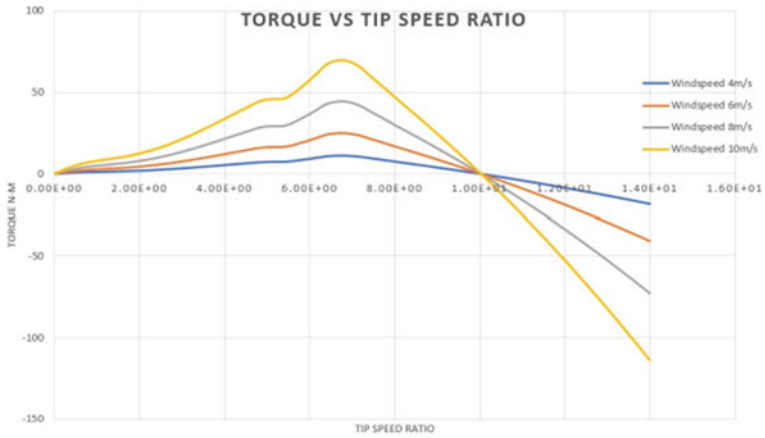


Fig. 11 Torque versus  $\lambda$ .

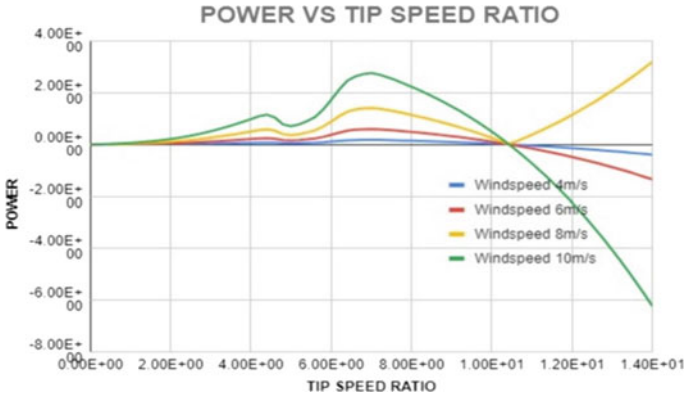


Fig. 12 Power versus  $\lambda$ .

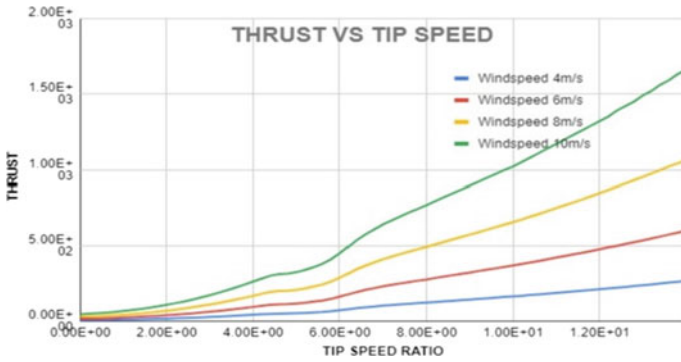
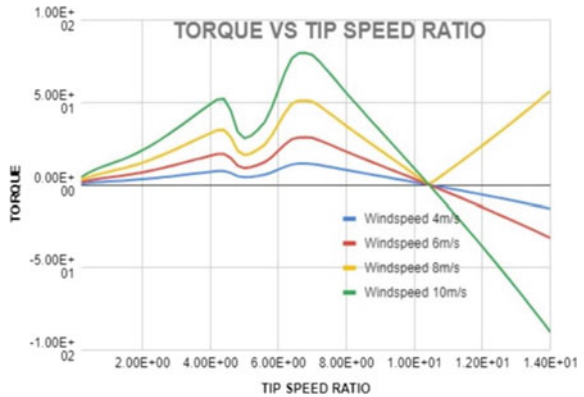


Fig. 13 Thrust versus  $\lambda$ .

Fig. 14 Torque versus  $\lambda$ .



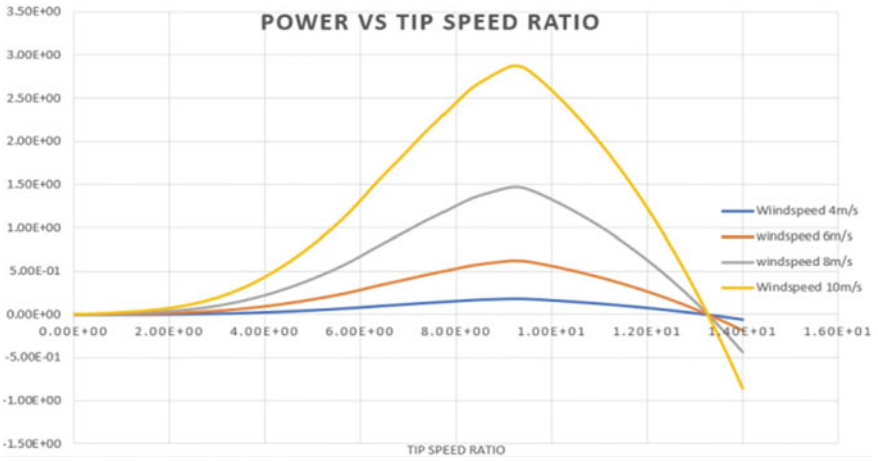


Fig. 15 Power versus  $\lambda$

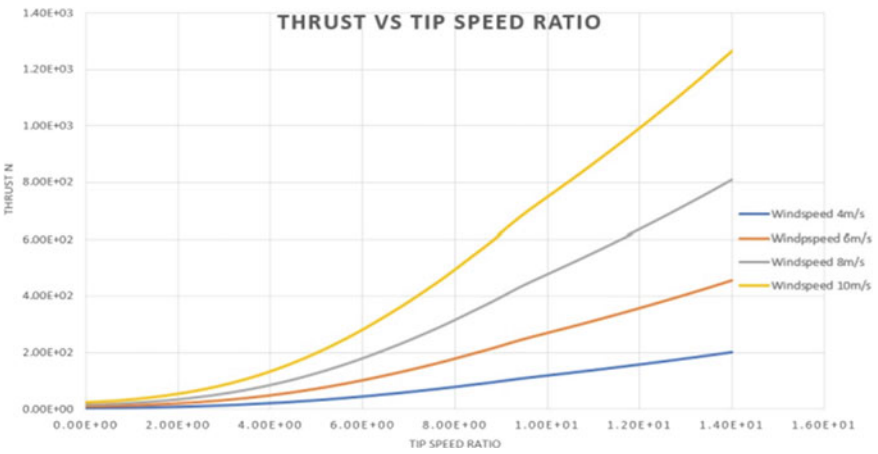


Fig. 16 Thrust versus  $\lambda$

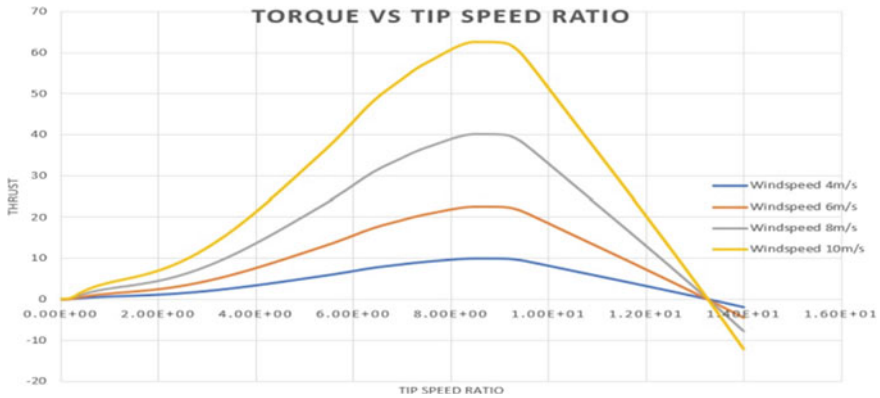


Fig. 17 Torque versus  $\lambda$

## 4 Conclusion

The analysis of the four airfoils (S809, S812, S813, and S814) has been done, and the performance graphs have been obtained. The wind turbine analyzed was HAWT (three-bladed), and various aerodynamic parameters were obtained. The purpose of such analysis is to determine the best wind turbine for use that is profitable in all aspects. The best wind turbine will be the one that produces the highest amount of energy and is equally economical. The above analysis is to find the best airfoils for HAWT, and the results show that from the chosen airfoils S809, S812, S813, S814, the airfoil that give the maximum power, thrust, and torque output will be the most preferred airfoil. So, it is found that S814 airfoil produces the maximum power output compared to the airfoils S809, S812, S813.

## References

1. Somers DM (1997) Design and experimental results for the S809 Airfoil, NREL/SR-440-6918. National Renewable Energy Laboratory, Golden, Colorado, p 103
2. Sørensen JN, Mikkelsen R, Troldborg N, Okulov VL, Shen WZ (2013) Mechanics down under. <https://doi.org/10.1007/978-94-007-5968-8>
3. Alaskari M, Abdullah O, Majeed MH (2019) Analysis of wind turbine using QBlade software. IOP Conf Ser Mater Sci Eng 518(3). <https://doi.org/10.1088/1757-899X/518/3/032020>
4. Jafari M, Razavi A, Mirhosseini M (2018) Effect of airfoil profile on aerodynamic performance and economic assessment of H-rotor vertical axis wind turbines. Energy 165:792–810. <https://doi.org/10.1016/j.energy.2018.09.124>
5. Paul A, Ghoshal T, Hassan M (2020) Computational analysis of a horizontal axis wind turbine blade profiles at low wind speed, pp 1–6
6. Sunny KA, Kumar P, Priscilla S, Kumar NM (2018) Computational analysis of three blade vertical axis wind turbine. Prog Ind Ecol Int J 12(1/2):120. <https://doi.org/10.1504/pie.2018.10016967>



7. Tjiu W, Marnoto T, Mat S, Ruslan MH, Sopian K (2015) Darrieus vertical axis wind turbine for power generation II: challenges in HAWT and the opportunity of multi-megawatt Darrieus VAWT development. *Renew Energy* 75(March):560–571. <https://doi.org/10.1016/j.renene.2014.10.039>

# Computational Technique Adopted to Study Vortex Formation in Industrial Wind Turbines



Dhanish Ahamed, Chinni Maadesh, Harish Adishwar, Ayshwarya Mahadevan, and Aravind Seeni

**Abstract** Problems in wind engineering are addressed using computational techniques, or computational wind engineering (CWE). Although Computational Fluid Dynamics (CFD) is just one component of CWE, it has up to now been used as a main tool. The vortex formation in wind turbines has to be studied certainly in order to avoid the formation of induced drag and methods that are required to minimize the effects of vorticity. The boundary layer formation analysis and vortex formation analysis in the blades of industrial wind turbines are solved using numerical techniques. To achieve the necessary flow characteristics, such as vortex generation and boundary layer creation in the wind turbine blades during flow separation, the lift-to-drag ratio, pressure coefficient, variation of lift with respect to the angle of attack, variation of drag with respect to the angle of attack, and intensity of induced drag brought on by vortex formation are studied using CFD. It also encloses the control and minimizing techniques of vorticity generation and boundary layer formation.

**Keywords** CFD · Vorticity · Boundary layer · HAWT · Three-blade turbine

## Abbreviation

- v Tangential velocity (m/s)
- r Strength of vortex filament ( $m^2/s$ )
- $\omega$  Angular velocity of fluid particle (rad/s)
- r Radial distance between elemental vortex filament and point in space
- l Total length of the vortex filament

---

D. Ahamed · C. Maadesh · H. Adishwar · A. Mahadevan · A. Seeni (✉)  
Department of Aeronautical Engineering, Rajalakshmi Engineering College, Thandalam,  
Chennai, Tamil Nadu 602105, India  
e-mail: [aravindseeni.s@rajalakshmi.edu.in](mailto:aravindseeni.s@rajalakshmi.edu.in)

© The Author(s), under exclusive license to Springer Nature Singapore Pte Ltd. 2024  
S. G. Rajasekharan et al. (eds.), *Proceedings of the 9th National Conference on Wind Engineering*, Lecture Notes in Mechanical Engineering,  
[https://doi.org/10.1007/978-981-99-4183-4\\_11](https://doi.org/10.1007/978-981-99-4183-4_11)

## 1 Introduction

Humanity has known for ages how useful wind power can be in daily life, from sailboats to windmills. Developing and designing vertical axis wind turbines have been the subject of several research projects. Among the few investigations, two were emphasized here and categorized as computational studies and experimental studies. Due to population increase and the expansion of economies, the world's energy demand is anticipated to more than quadruple by 2060. Lift-based Darrieus VAWT design is more frequently utilized since it has larger power coefficients [1]. Darrieus VAWTs typically fall into one of two categories based on blade configuration: both straight and curved blades. Straight line blades, in particularly the H-rotor types, have gained popularity because of how easily they can be produced. On employing VAWT, maximum power coefficient can be achieved, but on the other hand, construction, operation, and cost of manufacturing are crucial considerations when choosing VAWTs as in [2] for power production. Power generation expenses will be decreased by raising the power coefficient of VAWTs and HAWTs.

## 2 Problem Statement

The present analysis incorporates the formation of vorticity in the wind turbines and the intensity of vortices in the tip and the root of the blades. Unlike the aircrafts, the vortex in the wind turbine blade is of different structures and it is an important aspect of study the vortex structure in the blades. The airfoils chosen are S833, S834, and S835 of the NREL series. Also, vorticity formation due to the upstream flow or the wind speed is analyzed and an insight on ways to reduce the vortices is given. The turbulence analysis is included in the paper and the corresponding results are provided.

## 3 Methodology

The paper is expected to exhibit the study of vortex formation in the wind turbines. Initially, the blade is designed with S833, S834, and S835 airfoils separately and the simulation is done with four different wind speeds, and the vortices' formations are obtained. The turbulence models are taken and analyzed [3]. These airfoils are made with the intention of having a constrained maximum lift and a minimal sensitivity to leading-edge roughness [4]. In the past, an analysis for this type of wind turbine was performed where the analysis was performed for HAWT with a NACA airfoil. However, in this study, the HAWT blade type is chosen and S833, S834, and S835 airfoils are picked, and they are then given an aerodynamic analysis [5]. The vortex

formations in the wind turbine is a function of wind speed which is why the analysis involves choosing different wind speeds in order to provide the best airfoil for wind turbines.

## 4 Code QBlade

The turbulence analysis and vorticity formation were simulated in QBlade. It is a wind turbine design and simulation software. QBlade is a software that helps to design wind turbine and maximizes all the key relations between blade twist, chord, section airfoil performance, turbine control, power, and load curves in a clear and understandable manner.

## 5 Theory

For quantitatively predicting liquid and gas flows in many industrial applications, Computational Fluid Dynamics (CFD) is a potent tool. Air flows around wind turbines to produce renewable energy by turning the turbine blades, which is an obvious application of CFD in wind energy.

### 5.1 Vorticity

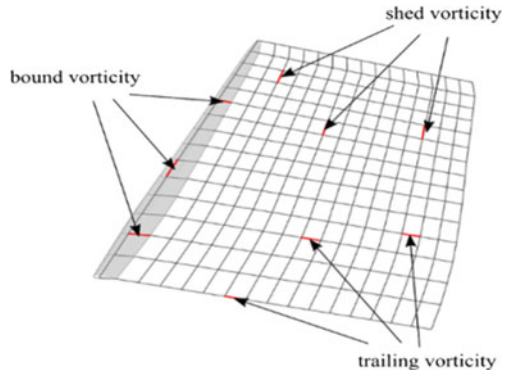
The vortex flow is that type of flow in which the fluid particles take a rotational motion during its flow separation from the fluid–solid interaction. Free vortex flow and forced vortex flow are the two types of vortex flows, whereas in forced vortex flow, the fluid particles rotate in its own axis by means of the external torque applied to the fluid flow. Tangential velocity acting on the fluid,

$$v = \omega r. \quad (1)$$

The analysis is based on the formation of vortices in the wind turbine which replicates the number of vortex filaments that has formed during the flow separation in the wind turbine blades. The vortices are developed is formed in the downstream of the blades which induces a velocity at some points by Biot–Savart law.

$$d\vec{v} = \frac{\Gamma}{4\pi} \frac{\vec{d}_l \times \vec{r}}{r^3} \quad (2)$$

**Fig. 1** LLFVW model



By integrating the above expression, the velocity relation is obtained

$$v = \frac{\Gamma}{4\pi} \int_{-\infty}^{\infty} \frac{\sin \vartheta}{r^2} dl \tag{3}$$

The Lifting Line Free Vortex Wake technique may be used in QBlade to mimic the aerodynamic forces operating on a rotor (LLFVW). The FVW approach used in this study solves for the turbine wake. The FVW model is derived from Lagrangian method (Fig. 1).

## 6 Results and Discussions

In this analysis, geometric models of the airfoils have been created and vortex formations in the wind turbines are simulated for three different turbine blade geometries. According to the author’s knowledge, it is found theoretically that the number of vortex filaments formed across the wake of the blade is inversely proportional to the wind speed.

### 6.1 Geometric Model

The below given figure shows the blade design of the airfoils S833, S834, and S835:

1. S833 (Fig. 2).



**Fig. 2** S833 blade



**Fig. 3** S834 blade



**Fig. 4** S835 blade

- 2. S834 (Fig. 3).
- 3. S835 (Fig. 4).

### 6.2 Vortex Simulations

The vortex simulations for four different wind speeds are shown:

- (1) *Airfoil: S833 speed of wind in m/s*
  - 1. *Speed of wind: 10 (Fig. 5).*
  - 2. *Speed of wind: 12 (Fig. 6).*
  - 3. *Speed of wind: 14 (Fig. 7).*
  - 4. *Speed of wind: 16 (Fig. 8).*

**Fig. 5** Vortex formation of S833 (10)

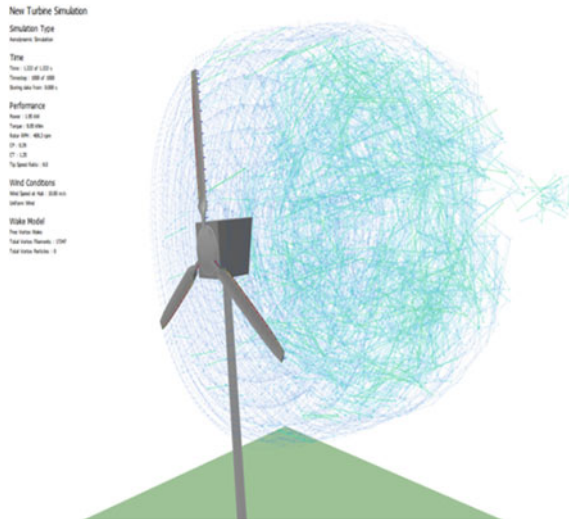


**Fig. 6** Vortex formation of S833 (12)

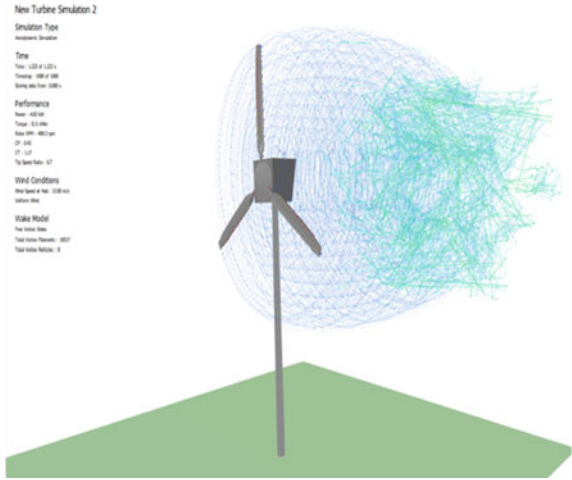


**Fig. 7** Vortex formation of S833 (14)

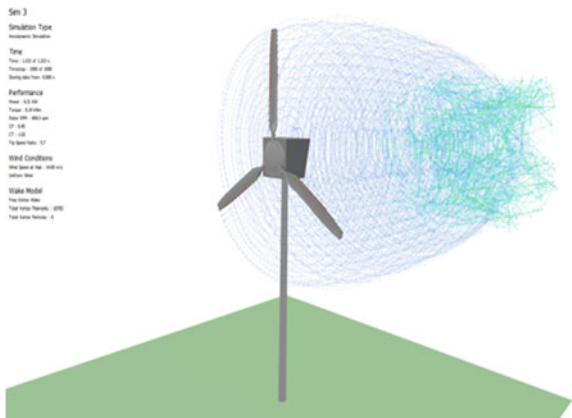
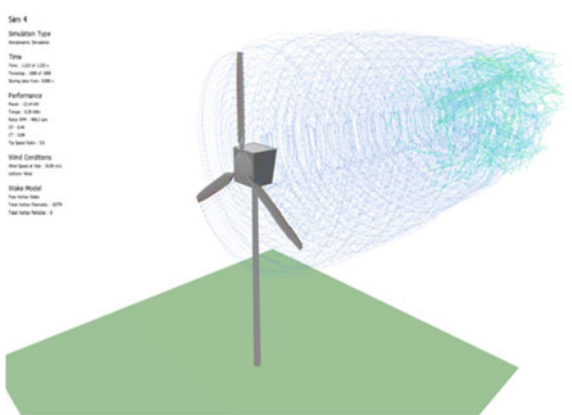


**Fig. 8** Vortex formation of S833 (16)



### 6.3 Turbulence Graphs

The graphs of blade length versus circulation, time versus induced velocity, and time versus vortex filaments for S833 are given below (Figs. 9, 10 and 11):

(2) *Airfoil: S834*

1. *Speed of wind:* 10 (Fig. 12).
2. *Speed of wind:* 12 (Fig. 13).
3. *Speed of wind:* 14 (Fig. 14).
4. *Speed of wind:* 16 (Fig. 15).

**Fig. 9** Plot of blade length versus circulation

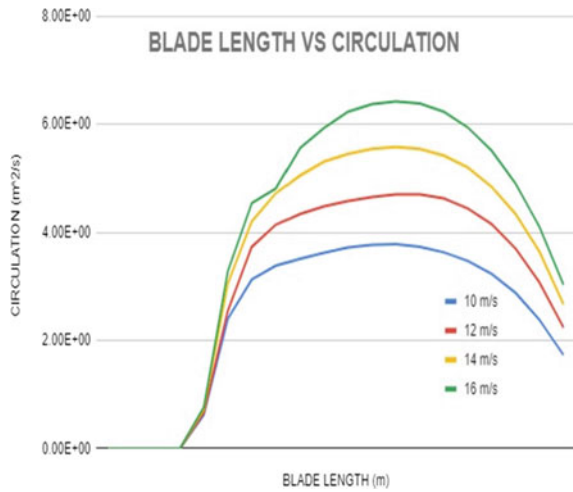


**Fig. 10** Plot of time versus induced velocity

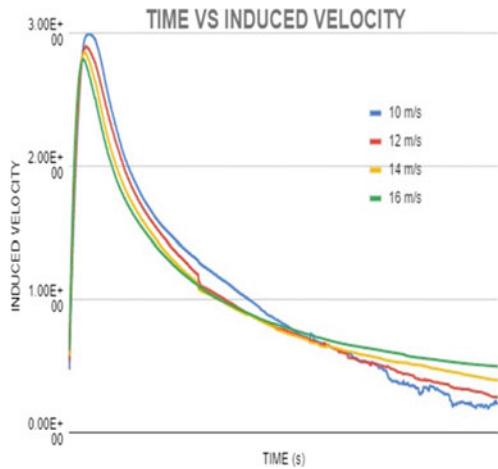




**Fig. 11** Plot of time versus vortex filaments

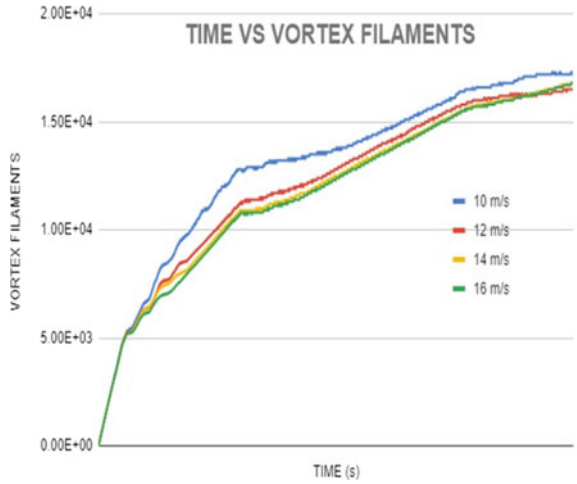


**Fig. 12** Vortex formation of S834 (10)

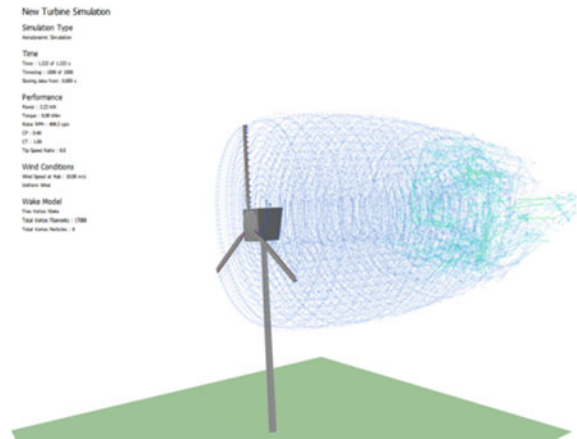


**Fig. 13** Vortex formation of S834 (12)

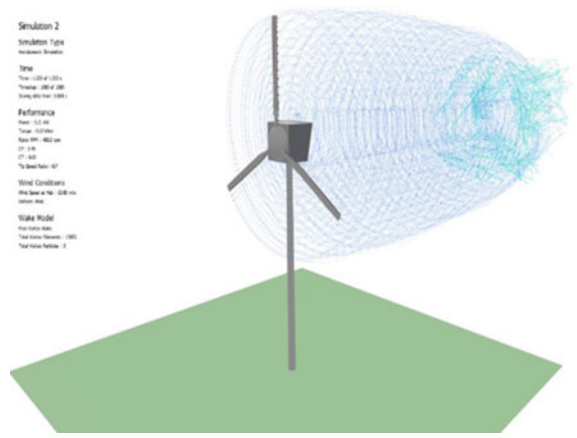


**Fig. 14** Vortex formation of S834 (14)

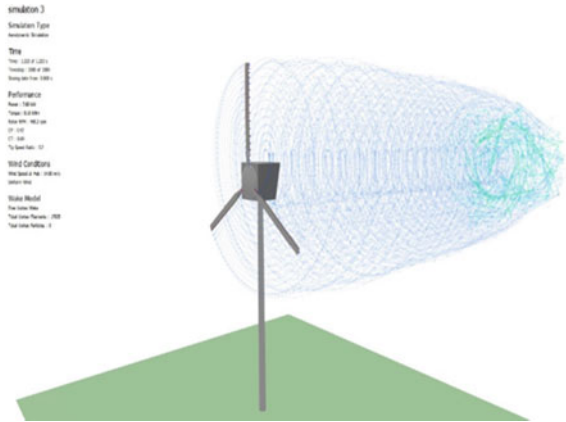
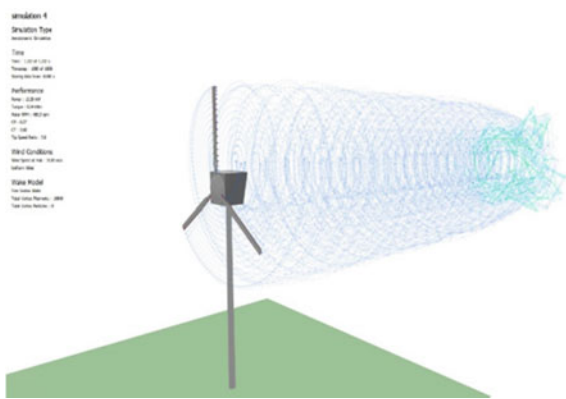


**Fig. 15** Vortex formation of S834 (16)



### 6.4 Turbulence Graphs

The graphs of blade length versus circulation, time versus induced velocity and time versus vortex filaments for S834 are given below (Figs. 16, 17 and 18):

(3) *Airfoil: S835*

1. *Speed of wind: 10* (Fig. 19).
2. *Speed of wind: 12* (Fig. 20).
3. *Speed of wind: 14* (Fig. 21).
4. *Speed of wind: 16* (Fig. 22).

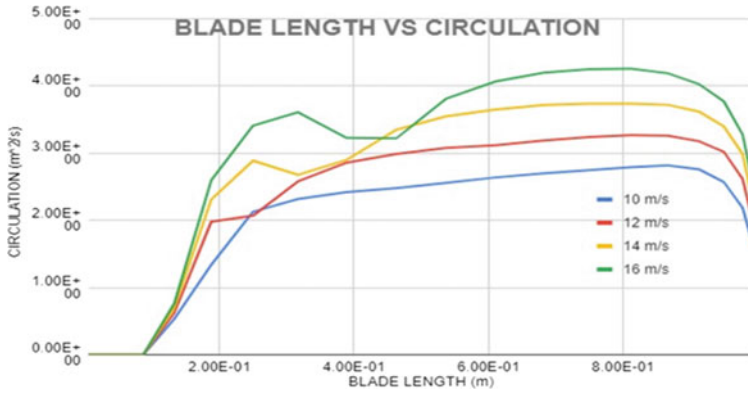


Fig. 16 Plot of blade length versus circulation

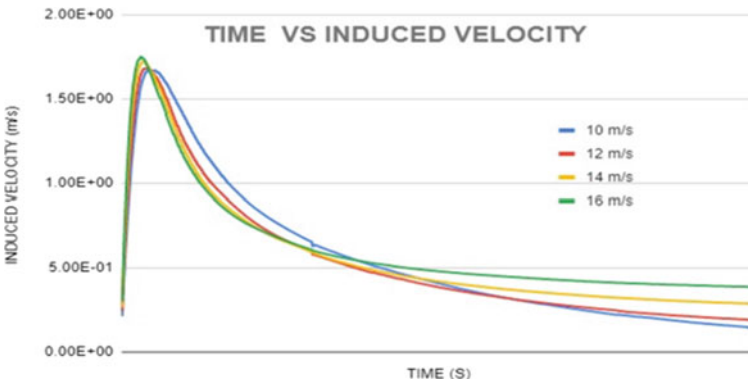


Fig. 17 Plot of time versus induced velocity

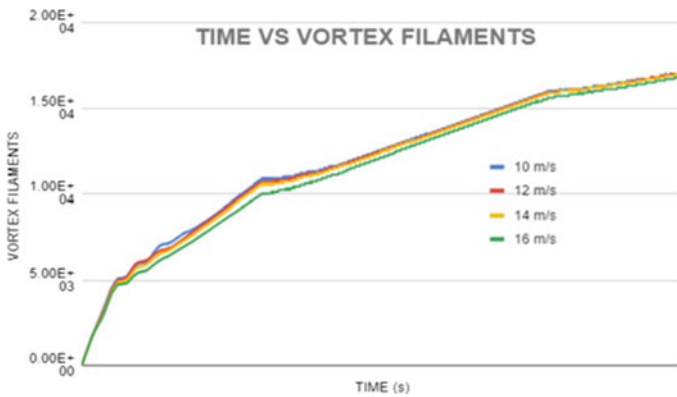
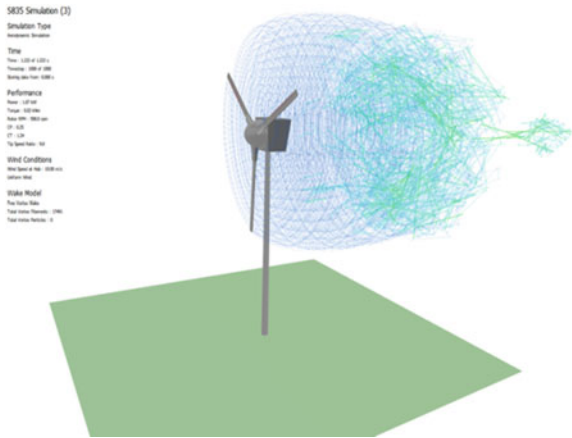
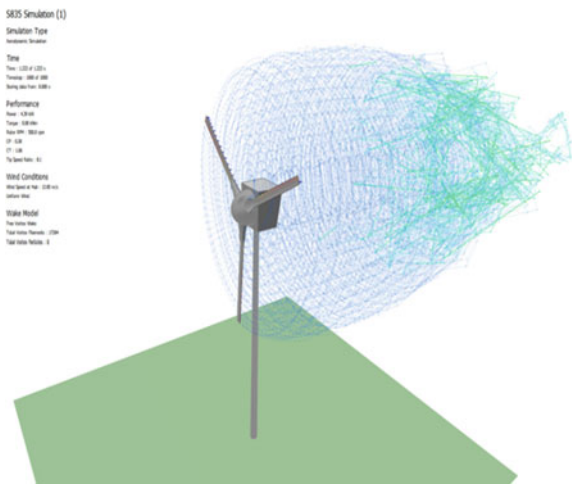


Fig. 18 Plot of time versus vortex filaments

**Fig. 19** Vortex formation of S835 (10)



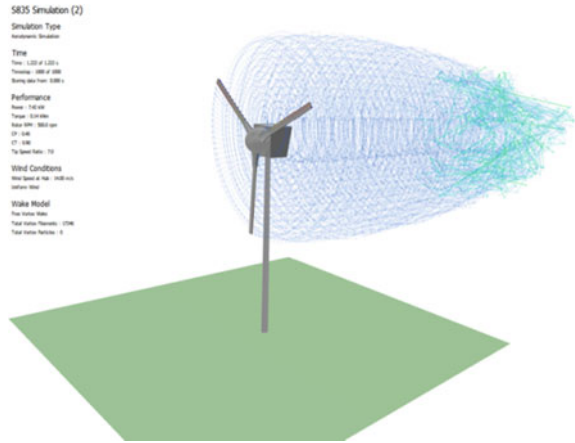
**Fig. 20** Vortex formation of S835 (12)



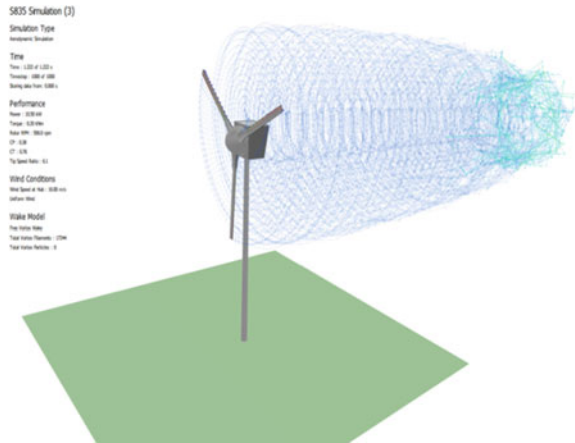
### 6.5 Turbulence Graphs

The graphs of blade length versus circulation, time versus induced velocity, and time versus vortex filaments for S835 are given below (Figs. 23, 24 and 25):

**Fig. 21** Vortex formation of S835 (14)



**Fig. 22** Vortex formation of S835 (16)



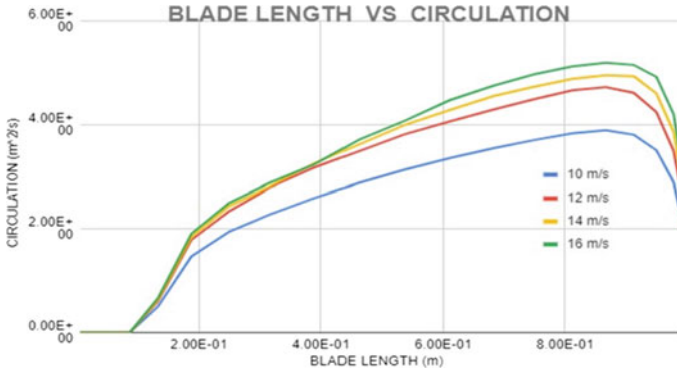


Fig. 23 Plot of blade length versus circulation

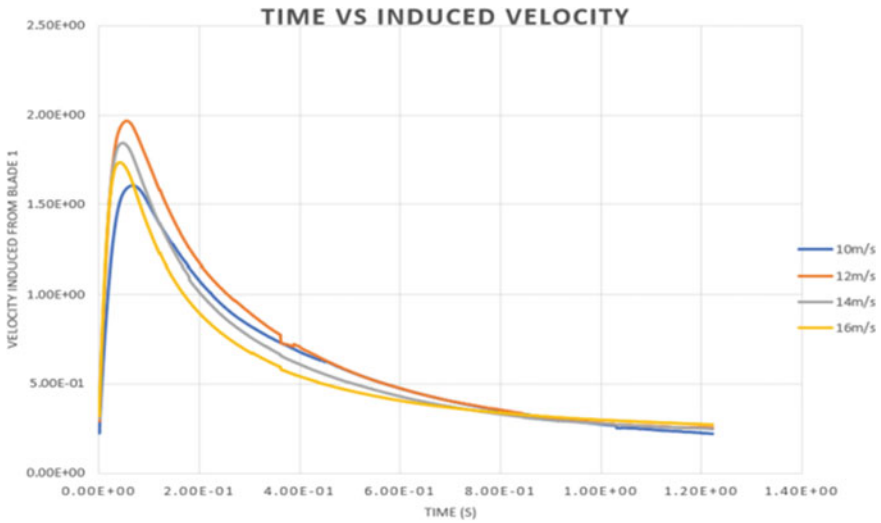


Fig. 24 Plot of time versus induced velocity

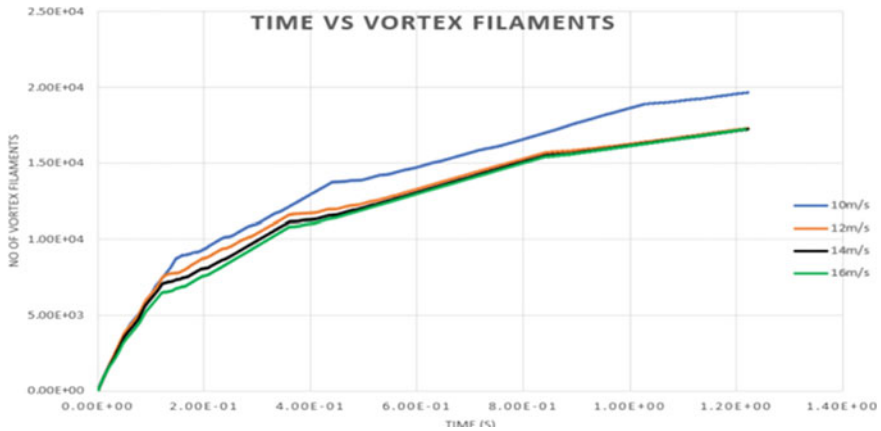


Fig. 25 Plot of time versus vortex filaments

## 7 Conclusion

The vorticity formation for the three airfoils has been obtained along with the graphs to study turbulence. The vortices formed during the working of a wind turbine affect the performance of it. Hence, it is essential to analyze and study ways to reduce them. From this analysis, it is found that distance between the wind turbine and the formation of vortex filaments is lesser at low wind speeds and formation of vortex filaments which is at high wind speeds is farther from the wind turbine. During the blade rotation, there is formation of vortices' downstream of wind turbine. By comparing the airfoils S833, S834, S835 based on the formation of vortex filaments, it is found that for S834 airfoil, the distance between the formation vortex filaments and wind turbine is more at low wind speeds, whereas for S833 and S835 airfoils, the distance is less at low wind speeds.

## References

1. Air KM (2012) Aerodynamic analysis of the NREL 5-MW wind turbine using vortex panel method master's thesis in fluid mechanics
2. Chen W-H, et al (2021) Two-stage optimization of three and four straight-bladed vertical axis wind turbines (SB-VAWT) based on Taguchi approach. *Electron Energy* 1(December):100025. <https://doi.org/10.1016/j.prime.2021.100025>
3. Ngala G, Shuwa M (2015) A CFD analysis of a micro horizontal axis wind turbine blade a CFD analysis of a micro horizontal axis wind turbine blade aerodynamics. In: Center for entrepreneurial and enterprise development keywords : computerized fluid dynamics, wind turbine, aerodynamic, May 2020

4. Voutsinas SG (2006) Vortex methods in aeronautics: how to make things work. *Int J Comput Fluid Dyn* 20(1):3–18. <https://doi.org/10.1080/10618560600566059>
5. Xue Z, Fu J, Zhao M (2019) Numerical simulation and analysis of the arrangement of wind direction meter for wind turbine. In: *E3S web conference*, vol 118, pp 1–8. <https://doi.org/10.1051/e3sconf/201911802040>



# Shear Lag Effect in Framed-Tube Buildings Due to Torsional Wind Load



Ashish Singh, Piyush Gaikwad, and Sasankasekhar Mandal

**Abstract** Wind load causes shear lag in high-rise tubular buildings. A building's stability may be adversely affected by this phenomenon when tension inevitably develops in upper story columns. The amount of shear lag depends on several factors, such as the building layout, the spacing between the outer peripheral columns, and the load applied to the building. The shear lag effect must therefore be accurately analyzed by considering these factors. This paper attempts to study the effect of torsional wind loads on the shear lag effect. Four wind load cases are adopted from American code (ASCE 7-22) to analyze the wind load effects on a 40-storied RCC tubular building. The results indicate that axial force distribution changes significantly with changes in the loading patterns of the building. Torsion and non-torsional load cases exhibit different unsymmetrical axial force distributions. Load cases with both direction loadings show notable differences in the axial force distribution compared to single-direction loadings. Axial force distributions due to the case of both face loading are unsymmetrical on both sides of the central column.

**Keywords** Codal provisions · Framed tube · Shear lag phenomenon · Wind loading · Torsional wind load

## 1 Introduction

Structural systems, such as rigid frames, braced frames, shear-walled frames, outriggers, framed tubes, braced tubes, and bundled tubes, can be used to resist wind load depending on the functional requirements of the building. In terms of lateral load resistance, framed-tube systems are one of the most reliable structural systems. It consists of closely spaced columns at the periphery of the building, and it is connected by deep spandrel beams. The shape of the tube is similar to that of a hollow concrete tube. Shear lag occurs when a box structure is loaded laterally [1–4]. As a result,

---

A. Singh (✉) · P. Gaikwad · S. Mandal  
Department of Civil Engineering, IIT (BHU), Varanasi, India  
e-mail: [ashishsingh.rs.civ18@iitbhu.ac.in](mailto:ashishsingh.rs.civ18@iitbhu.ac.in)

© The Author(s), under exclusive license to Springer Nature Singapore Pte Ltd. 2024  
S. G. Rajasekharan et al. (eds.), *Proceedings of the 9th National Conference on Wind Engineering*, Lecture Notes in Mechanical Engineering,  
[https://doi.org/10.1007/978-981-99-4183-4\\_12](https://doi.org/10.1007/978-981-99-4183-4_12)

tubular structures are likely to exhibit a greater degree of shear lag. It alters the assumptions about the plane section in box structures and causes non-uniform stress along the sides, which violates the elementary beam theory (Fig. 1). Flexural normal stress is greater at the edge of the flange than at the center (positive shear lag). Foutch and Chang [5] discovered the opposite shear lag anomaly, known as negative shear lag. An investigation of the negative shear lag for composite beams was also conducted by Singh et al. [6]. Positive shear lag is found to be the source of negative shear lag [7]. Shear lag reduces the efficiency of tube-type structures [8, 9]. Considering shear lag, Mahjoub et al. [10] evaluated the performance of the framed tube by assessing the axial stress distribution on the exterior panels. Leonard [11] examined the shear lag effect in diagrid systems with a given factor. Moghadasi et al. [12] examined the relationship between shear lag and lateral loads (wind and earthquake) on concrete tubular structures. The effect of terrain category, aspect ratio, and number of stories on the shear lag phenomenon in RCC-framed tube structures was examined by Kumari et al. [13].

An analysis of the shear lag effect in a 40-story RCC-framed tube building is presented in this paper based on torsional wind loading cases, recommended by

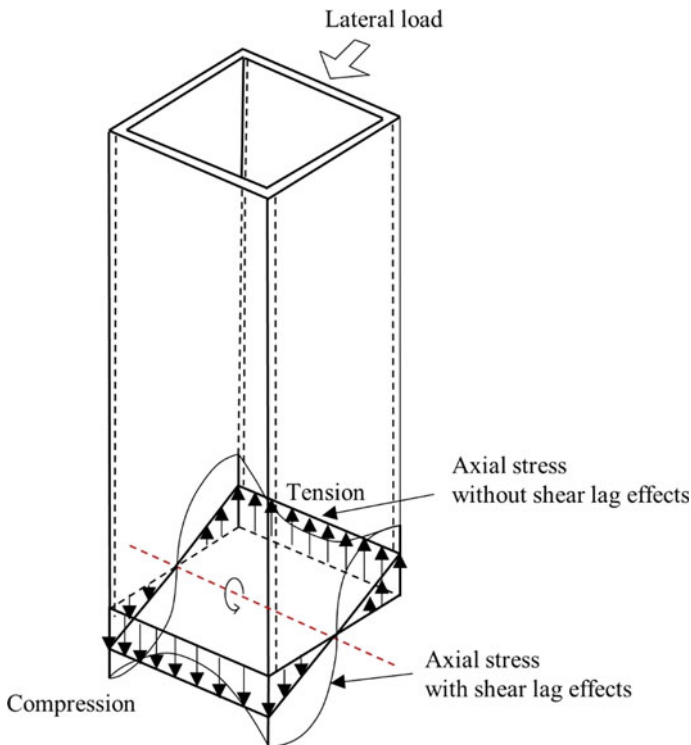


**Fig. 1** Framed tube building with and without shear lag effects

ASCE 7-22 [14]. This study is useful to understand how the axial forces in peripheral columns vary under torsional wind loading due to the shear lag effect.

## 2 Codal Provisions

Figure 2 shows the wind load cases that must be considered when designing main wind force-resisting system (MWFRS) for buildings of all heights. Torsional moment per unit height ( $M_T$ ) in Case 2 is calculated as  $M_T = 0.75 (P_{WX} + P_{LX}) B_X e_X$ , and in Case 4,  $M_T = [0.563 (P_{WX} + P_{LX}) B_X e_X + 0.563 (P_{WZ} + P_{LZ}) B_Z e_Z]$ , where  $e_X = \pm 0.15B_X$  and  $e_Z = \pm 0.15B_Z$ , and the building plan dimensions considered are  $B_X = 30$  m and  $B_Z = 35$  m.  $P_{WX}$ ,  $P_{WZ}$ , and  $P_{LX}$ ,  $P_{LZ}$  are windward and leeward pressure acting in x and y principal axes, which are calculated using the Indian standard [15].

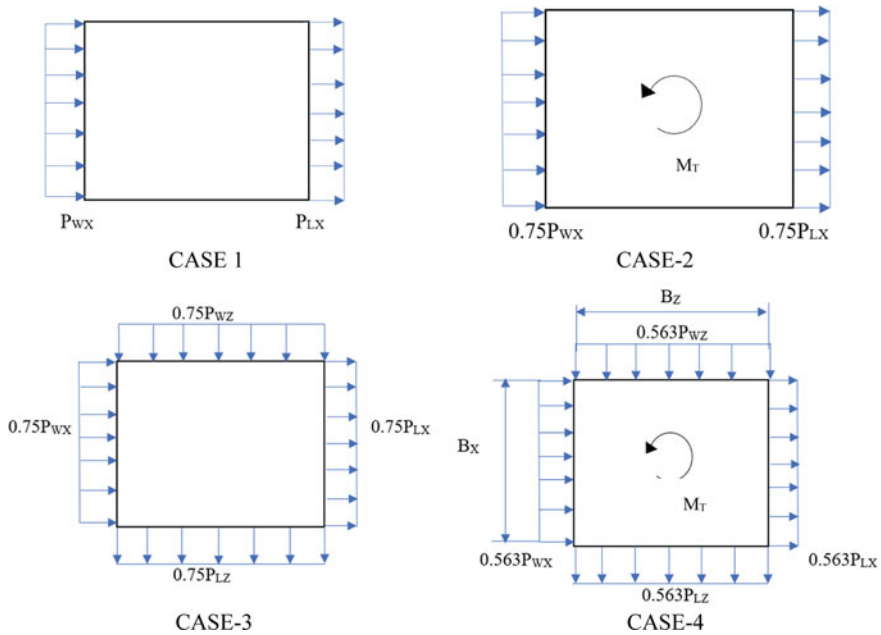


Fig. 2 Four different wind load cases taken from ASCE 7-22 [14]

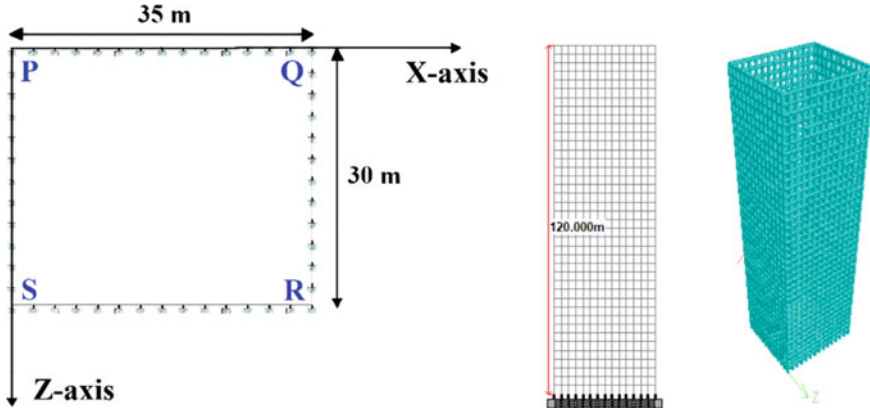


Fig. 3 Plan, elevation, and isometric view of STAAD-pro building model

### 3 Modeling and Analysis

#### 3.1 Building Dimensions

A model of 40-story RCC-framed tube building is analyzed using STAAD-pro software. Specification of the building is taken from Singh et al. [16], the height of the building is 120 m, and each floor has a height of 3 m; the plan dimensions of the framed tube are 35 m along X-axis and 30 m along Z-axis (Fig. 3); the beam and column sizes are  $0.8 \times 0.8$  m; the center-to-center spacing of the columns is 2.5 m in each direction, and the modulus of elasticity ( $E$ ) is 20 GPa and Poisson's ratio ( $\mu$ ) is 0.15. Also, a uniform dead load of  $3.43 \text{ kN/m}^2$  has been considered for all the cases.

#### 3.2 Calculation of Wind Pressure

Based on clause 6.3 (Design Wind Speed) and clause 7.2 (Design Wind Pressure) of code IS 875 (Part 3): 2015 [15], wind pressure calculations have been made. Table 1 lists the parameters and their values used to calculate wind load.

### 4 Results and Discussion

In this section, results of the analysis based on four different load cases are presented. The shear lag of a 40-story RCC tubular building is studied under four different loading cases. Axial force in columns of short edge (QR and PS-face) and long edge (SR and PQ-face) is plotted for 1st, 10th, 20th, 30th, and 40th stories in Figs. 4, 5,

**Table 1** Specification of the wind load

Parameters and descriptions	Values
Basic wind speed ( $V_b$ )	55 (m/s)
Terrain category	1
Probability factor ( $k_1$ )	1.08
Topography factor ( $k_3$ )	1
Importance factor for cyclonic region ( $k_4$ )	1
Area averaging factor ( $K_a$ )	0.8
Wind directionality factor ( $K_d$ )	0.9
Combination factor ( $K_c$ )	0.9

6 and 7. In order to conveniently understand the effect of four-direction loading, the axial force is plotted for all the faces. For Case 1 and Case 2, axial force pattern is similar in face QR and SR. This is due to loading in one direction. Case 3 and Case 4 also have the similar axial load pattern due to loading pattern similarity. Case 1 and Case 3 have totally different axial force patterns due to their distinct loading pattern.

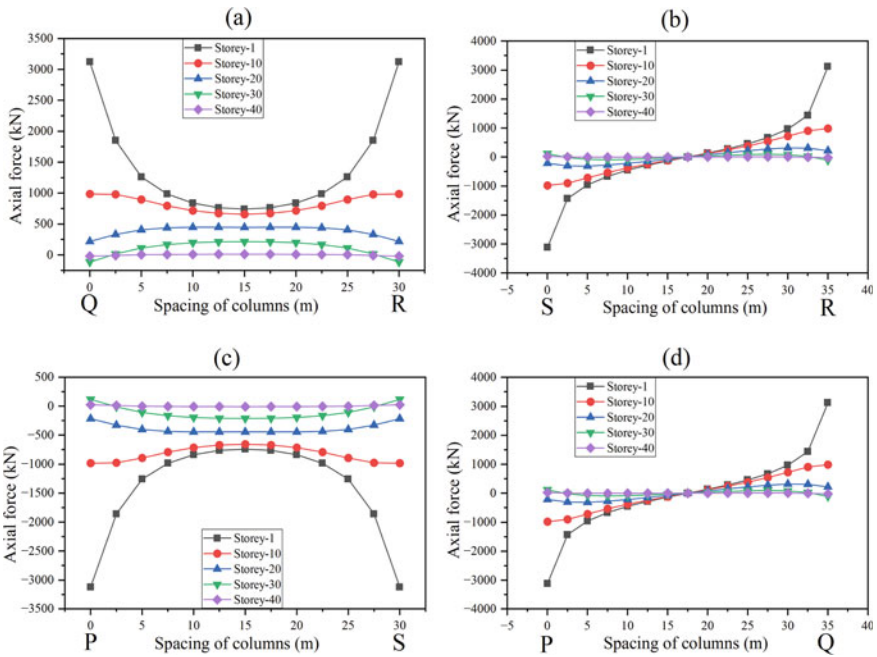


**Fig. 4** Axial force in a QR, b SR, c PS, and d PQ edge panels columns for ASCE Case 1

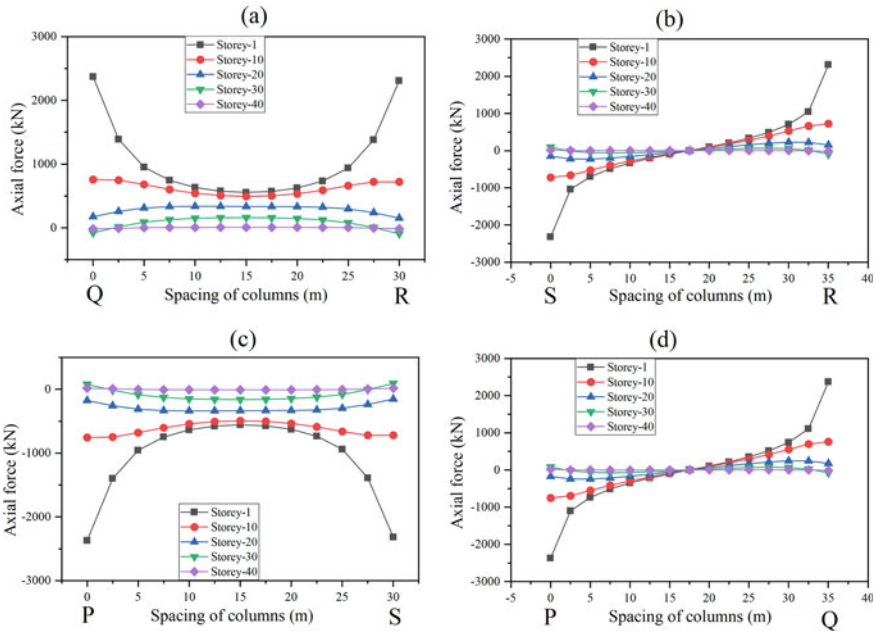


Fig. 5 Axial force in a QR, b SR, c PS, and d PQ edge panels columns for ASCE Case 2

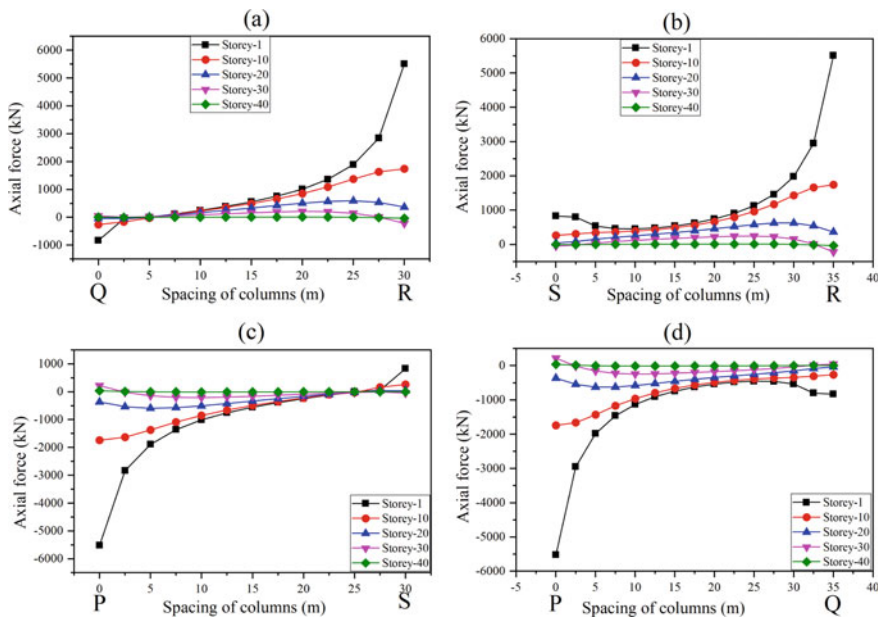


Fig. 6 Axial force in a QR, b SR, c PS, and d PQ edge panels' columns for ASCE Case 3

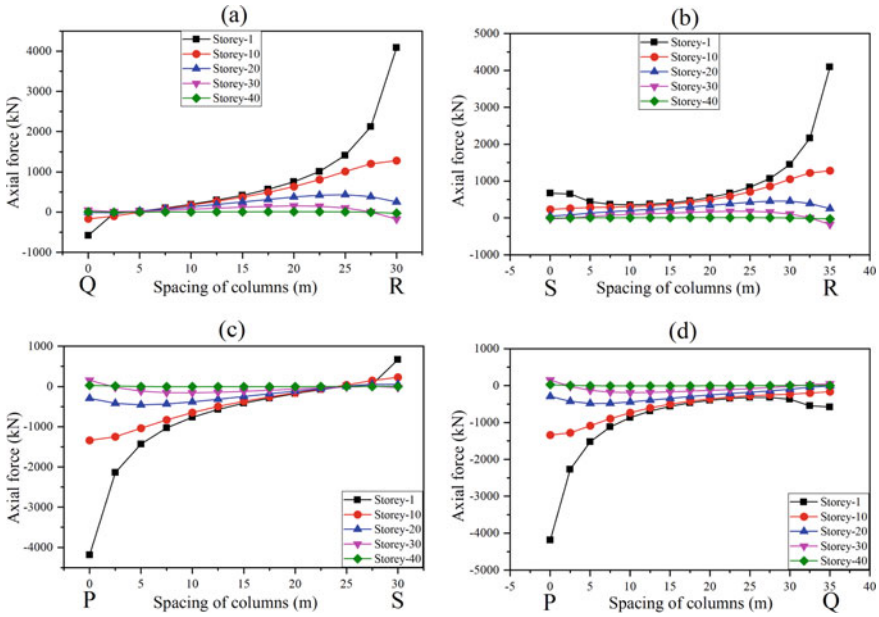


Fig. 7 Axial force in a QR, b SR, c PS, and d PQ edge panels columns for ASCE Case 4

### 4.1 Shear Lag Due to ASCE Case 1 Loading

The distribution of axial force obtained in Fig. 4 is called as positive shear lag, i.e., corner columns have more axial force than middle columns.

### 4.2 Shear Lag Due to ASCE Case 2 Loading (Including Torsion)

From Fig. 5, it can be seen that the distribution of axial force along both the panel is similar to that ASCE Case 1 which has no torsion. However, in this case, the magnitude of axial force gets reduced due to the application of partial (75% of ASCE Case 1) loading.

### 4.3 Shear Lag Due to ASCE Case 3 Loading

It can be clearly seen from Fig. 6 that axial force distribution is not symmetrical in any particular face unlike Figs. 4 and 5. The resultant load direction, in this case, is diagonal which is the PR direction; therefore, positive axial force at corner R

is observed which indicates compression, and negative axial force at corner  $P$  is observed which indicates tension. This case yields the maximum axial force as 5510 kN compared to all four cases. According to elementary beam theory, the variation of force must be linear; in this case, the variation of force is not linear, so shear lag is occurring.

#### **4.4 Shear Lag Due to ASCE Case 4 Loading**

Figure 7 shows the axial force distribution of this case, which produces similar results as Case 3 with 25% lesser magnitude. It is due to the 25% lesser wind load.

### **5 Conclusions**

In the present work, the shear lag effect is studied in framed-tube buildings due to torsional wind load. Based on the American Standard for torsional wind loads, four wind load cases are applied on 40-story RCC-framed tube building. Results obtained from the present study indicate that the shear lag phenomenon is occurring in all the loading cases. Both Cases 1 and 2 exhibit similar axial force patterns with distinct magnitudes. The results indicate the occurrence of positive shear lag in Cases 1 and 2. Both Cases 3 and 4 produced almost similar axial loading patterns with different magnitudes. The results indicate unsymmetrical axial loading in parallel faces and nonlinear loading patterns in each face in both Cases 3 and 4. Further study related to varying plan ratio, height aspect ratio, and spacing of outer column can be done in the future to get a better understanding of the shear lag phenomenon in the case of non-uniform wind loading.

### **References**

1. Kuzmanovic BO, Graham HJ (1981) Shear lag in box girders. *J Struct Div* 107(9):1701–1712
2. Lee SC, Chai HY, Dong YY (2002) Analysis of shear lag anomaly in box girders. *J Struct Eng* 128(11):1379–1386
3. Rovnak M, Duricova A (2004) A Discussion on analysis of shear lag anomaly in box girders. *J Struct Eng* 128(11):1860–1861
4. Zhou SJ (2008) Shear lag analysis of box girders. *Eng Mech* 25(2):204–208
5. Foutch DA, Chang PC (1982) A shear lag anomaly. *J Struct Div* 108(7):1653–1658
6. Singh GJ, Mandal S, Kumar R, Kumar V (2020) Simplified analysis of negative shear lag in laminated composite cantilever beam. *J Aerosp Eng* 33(1)
7. Singh Y, Nagpal AK (1994) Negative shear lag in framed-tube buildings. *J Struct Eng* 120(11):3105–3121
8. Khan FR, Amin NR (1972) Analysis and design of framed tube structures for tall concrete buildings. *Special Publ* 36:39–60



9. Coull A, Bose B (1975) Simplified analysis of framed-tube structures. *J Struct Div* 101(11):2223–2240
10. Mahjoub R, Rahgozar R, Saffari H (2011) Simple method for analysis of tube frame by consideration of negative shear lag. *Aust J Basic Appl Sci* 5(3):309–316
11. Leonard J (2007) Investigation of shear lag effect in high-rise buildings with diagrid system. M. E. Thesis, Massachusetts Institute of Technology, Massachusetts
12. Moghadasi M, Taeepoor S, Rahimian K, Petru M (2020) The effect of lateral load type on shear lag of concrete tubular structures with different plan geometries. *Crystals* 10(10):897
13. Kumari S, Singh A, Mandal S (2022) Effect of terrain category, aspect ratio and number of storeys on the shear lag phenomenon in RCC framed tube structures. In: *International conference on advances in structural mechanics and applications*. Springer
14. ASCE/SEI 7-22 (2022) American Society of Civil Engineers, Minimum design loads for buildings and other structures. American Society of Civil Engineers (ASCE): Reston, VA, USA
15. IS:875 Part 3 (2015) Code of practice for design loads (other than earthquake) for building and structures - Part 3. Wind Loads, New Delhi, India
16. Singh GJ, Mandal S, Kumar R (2015) Investigation on shear lag phenomenon in RCC framed tube structures. *i-Manager's J Struct Eng* 4(3):18

# Wind-Induced Interference Effects on a 125 m Tall RC Chimney in Typical Power Plant



G. Ramesh Babu, Ramya Niranjana, and A. Abraham

**Abstract** This paper presents the details of the wind tunnel investigations carried out on the aeroelastic behaviour of a tall RC chimney in the presence of surrounding structures for two typical power plant layouts in India. The RC chimney under investigation considered as a principal chimney has uniform diameter of 10.41 m and height of 124.5 m. The surrounding structures include 275 m tall chimney considered as interfering chimney and other power plant structures with the c/c distance-to-diameter ratio of 16 (layout-1) and 25 (layout-2) between principal chimney and interfering chimney. Experiments were conducted on the models with a geometric scale of 1:250 under simulated boundary layer conditions in the wind tunnel facility at CSIR-SERC, Chennai. Both the layouts are tested for various wind incidence angles and reduced velocity ( $\bar{U}/n_0D$ ) ranges from 1.8 to 6.56. From the previous research works carried out, the magnification factor was observed to be maximum when the principal chimney is in downstream and interfering chimney is at  $0^\circ \pm 15^\circ$ . In this work, the maximum magnification factor was noticed to occur when the interfering chimney is at  $15^\circ, 180^\circ, 210^\circ$  for layout-1 and  $35^\circ, 65^\circ, 320^\circ$  for layout-2. In addition to the magnification factor, the variation of maximum interference factor for the resultant bending moment at critical wind speed with respect to the angle wind incidence was also discussed.

**Keywords** Wind tunnel test · Interference effects · RC chimneys · Aeroelastic response · Magnification factor

## 1 Introduction

It is important to understand the dynamic response of wind-sensitive structures such as tall chimneys as complex fluid–structure interactions are expected to occur when subjected to wind loads. In a typical thermal power plant, a chimney is seldom in

---

G. Ramesh Babu · R. Niranjana (✉) · A. Abraham

Wind Engineering Laboratory, CSIR—Structural Engineering Research Centre, Chennai, India  
e-mail: [ramya@serc.res.in](mailto:ramya@serc.res.in)

© The Author(s), under exclusive license to Springer Nature Singapore Pte Ltd. 2024  
S. G. Rajasekharan et al. (eds.), *Proceedings of the 9th National Conference on Wind Engineering*, Lecture Notes in Mechanical Engineering,  
[https://doi.org/10.1007/978-981-99-4183-4\\_13](https://doi.org/10.1007/978-981-99-4183-4_13)

133

stand-alone condition and is usually surrounded by other structures, viz., similar or dissimilar chimneys, cooling towers, boiler and bunker buildings, etc. The complexity in flow mechanism and associated fluid–structure interaction increases manifold due to change in flow field caused by these surrounding structures. This phenomenon is termed as wind-induced interference effects which should be accounted during the design of chimneys.

The wind-induced behaviour of circular cylinders has importance in many engineering applications and has been studied extensively by many researchers. The presence of neighbouring structures/cylinders introduces interference effects either through shielding or enhancement on loads. Several researchers, starting with the pioneering work of Zdravkovich [1], have studied the effects of wind-induced interference effects between group of cylinders. Sets of two-, three-pipe clusters, square and irregular multi-pipe clusters with pipes of same diameter subjected to flow conditions are studied to obtain the variation of lift and drag coefficients. Based on a series of experiments, Zdravkovich classified three regions for the purpose of studying flow interference between two cylinders as (a) proximity, (b) wake and (c) no interference regions. Wind tunnel experiments were carried out by Gowda et al. [2] on two circular cylinders with varying diameter ratios for different arrangements (tandem, staggered and side-by-side). It was inferred that the tandem arrangement was critical as peak response in interference condition increased by 2–3 times compared to the isolated case. Wind tunnel investigations of interference effects between two and three cylinders of equal diameter of finite height were carried out by Kareem et al. [3] in simulated boundary layer conditions in both tandem and side-by-side configurations. The variation of force coefficients with respect to different arrangements, spacing of cylinders and wind incident angles was discussed. Pressure distributions on two circular cylinders in staggered arrangement with aspect ratio of 6.4 were reported by Gu and Sun [4]. From their study, they have classified the pressure pattern distribution into three groups corresponding to various angles of attack. Interference effect of two-, three- and four-cylinders of varying diameters (6, 8.9 and 12.2 cm) arranged in-line was investigated by Liu et al. [5] through wind tunnel tests. The change in mean force coefficients for different spacings, smooth and turbulent flow conditions, surface roughness and Reynolds numbers were discussed in detail.

Following the studies on group effects of uniform circular cylinder at subcritical flow conditions, research activities on understanding the interference effects between tall chimneys subjected to boundary layer flow were extensively carried out. Wind tunnel experiments were performed by Niemann and Kasperski [6] on two 200 m reinforced concrete (RC) chimneys of 20 m diameter subjected to  $0^{\circ}$ – $30^{\circ}$  angle of attack. They opined that the interference leads to mixed excitation besides resonance due to the turbulence of the oncoming flow, and considerable resonance excitation may occur due to wake buffeting for chimneys with high natural frequencies. Aeroelastic model of 100 m tall chimney with surrounding chimneys and buildings was tested in wind tunnel by John et al. [7]. The across-wind response was found to be predominant and was two times higher in interference condition compared to isolated condition. The reduction in response due to the influence of stakes has also been discussed. Interference effects were studied for two 200 m tall chimneys using

rigid model in wind tunnel by Sun et al. [8]. Pressure distribution was obtained for various angles of attack ranging from  $0^\circ$  to  $180^\circ$  and spacing-to-diameter ratios of 2–6. Critical angles of attack and spacing ratios were identified, and it was also observed that across-wind response was predominant. This work was followed by performing experimental tests on aeroelastic model of tall chimneys by Su et al. [9] for the critical angles of attack and spacings. For spacing-to-diameter ratios of 3–6, response is influenced by vortex shedding due to upstream chimney, and for ratio less than 2, gap flow was found to dominate the response. In addition, the experimental values with ACI 307-08 standard [10] was also compared. Three different groups of two tall chimneys with combination of straight, 1:40 and 1:50 taper cylinders were tested by Rajora et al. [11] to compare the along- and across-wind responses. The results were compared with various codes for spacing-to-diameter ratios greater than 15. The magnification factors were found to be greater than 1 even for higher spacing to diameter ratios ( $>35$ ).

From the previous research works conducted, it is evident that the wind-induced interference effects have been mostly studied for identical cylinders/chimneys with same height and diameter and the interfering cylinder placed in tandem, staggered or side-by-side positions. In a thermal power plant layout, these typical cases may not be directly applicable to obtain responses of tall chimneys. In this work, we have considered dimensions of tall chimneys from a typical power plant layout to understand the wind-induced interference effects. The effect of 275 m tall RC chimney with base diameter of 30 m and having tapering for the bottom 40% of the height (interfering chimney) and surrounding building structures on a 124.5 m tall uniform diameter (10.41 m) RC chimney (principal chimney) for two different layouts are investigated using wind tunnel experiments. The *c/c* distance-to-diameter (*S/D*) ratio is 16 for layout-1 and 25 for layout-2. The location and orientation of surrounding structures are different in two layouts as in a typical power plant.

## 2 Wind Tunnel Test Setup

Experiments are performed in open circuit and blower-type boundary layer wind tunnel having test section of dimensions 2.5 m (*W*)  $\times$  2.0 m (*H*)  $\times$  18.0 m (*L*) at CSIR-SERC, India. It is possible to satisfactorily generate a boundary layer depth of about 1.20 m in the test section corresponding to open terrain conditions. Since the model of the chimney is to be fully immersed within the boundary layer as per similarity requirements, a scale of 1:250 was selected in the present study. The aeroelastic model of the principal chimney is fabricated using aluminium, and the resulting model dimensions to a geometric scale of 1:250 is 498 mm height, 41.64 mm diameter and 1.6 mm thickness. The interfering chimney is also scaled down as rigid model is made of wood material with a height of 1100 mm. The models of surrounding building structures are fabricated with acrylic sheets. The principal chimney is mounted at the centre of the turntable whose diameter is about 2.4 m.

Wind tunnel tests are conducted under simulated wind characteristics pertaining to open terrain category as per Indian Standard (IS) 875 (Part 3):2015 [12]. The required wind characteristics are achieved using a trip board and wooden panels containing roughness cubes in the test section. The typical power law coefficient for open terrain condition as per IS 875 (Part 3):2015 of 0.16 is also experimentally accomplished. Furthermore, the turbulence intensity is also achieved as per the IS code. The power spectrum of longitudinal fluctuating component of wind speed simulated is found to be in good agreement with the von Karman spectrum.

Tests are conducted for a range of mean wind speeds between 8.78 and 32.2 m/s measured at top of principal chimney model (498 mm). The mean wind speeds during the tests are measured using pitot-static tube whose static and total are connected to a 2480 Pa pressure scanner. Strain gauge instrumentations are adopted on the aeroelastic model of the principal chimney with strain gauge channels in two orthogonal directions at four locations, at base (0.0241 H), 0.25 H, 0.5 H and 0.75 H, where H is the height of the chimney, to measure the bending moments (BMs) at these levels. For each channel, full bridge circuitry is used with four strain gauges having a resistance of 120  $\Omega$  and gauge factor of  $2.13 \pm 1\%$ . The strain gauge channels are calibrated using standard dead weights. Additionally, the model is instrumented with two accelerometers at the top in orthogonal directions to measure tip accelerations. The data are acquired with a sampling frequency of 1200 samples/s and a sampling duration of 15 s. For each wind speed, data are acquired for three trials.

Experimental investigations are carried out in three stages. Firstly, the principal chimney is tested in stand-alone condition subjected to 13 different wind speeds having mean wind velocities between 8.78 and 32.2 m/s. These wind velocities correspond to a reduced velocity  $\bar{U}/n_0D$  of 1.79–6.55. Following which, tests are performed for two different interference configurations (case-1 and case-2) with  $c/c$  distance-to-diameter ratios between principal and interfering chimneys of 16 and 25, respectively, for various angles of wind incidences between  $0^\circ$  and  $360^\circ$ . Figures 1 and 2 show the wind tunnel test setup for interference case-1 and case-2, respectively.

### 3 Evaluation of Modal Parameters for the Principal Chimney

Free vibration tests are performed to obtain the first natural frequency in sway mode and damping ratio of the principal chimney. Tests are conducted in two orthogonal directions by giving an initial disturbance to the aeroelastic model by hitting the model at the top using hammer. From the free vibration trace and its corresponding spectrum, natural frequency of 118 Hz is observed, and the damping ratio is computed using logarithmic decrement method which is around 1.6%. Mode shape corresponding to the first mode is obtained using measurements from two accelerometers. One accelerometer is fixed at the top of the model, and the position of the other



**Fig. 1** Wind tunnel setup for interference case-1 showing the principal chimney with the interfering chimney and surrounding building structures for  $120^\circ$  angle of wind incidence



**Fig. 2** Wind tunnel setup for interference case-2 showing the principal chimney with the interfering chimney and surrounding building structures for  $345^\circ$  angle of wind incidence

accelerometer is varied along the height. The relative magnitudes of spectral ordinates in the spectra of the free vibration traces of the two accelerometers at natural frequency of the model resulted in the mode shape co-ordinate at respective location along the height. Furthermore, the influence line profile for the tip deflection is evaluated by fixing a dial gauge at top of the model and varying the standard weight at different locations along the height. This influence line profile is used to compute the mean tip deflection.

## 4 Results and Discussion

### 4.1 Isolated Condition

The principal chimney is tested in stand-alone condition to understand the variation of along-wind and across-wind BMs corresponding to different wind speeds. The time histories of along-wind BMs are first resolved by separating the mean and the fluctuating components. Figure 3 shows the variation of mean and total fluctuating components of along-wind base BM with wind speeds. The values of mean BM with respect to wind speeds are found to vary linearly with square of mean wind velocity ( $U$ ). The total along-wind fluctuating component of BM is calculated using the spectra of BM and is found to linearly vary with  $U^{2.4}$ . The fitted equations using the above variations as given in Fig. 3 can be further used to compute the BMs for other wind speeds at which are not experiments are not conducted.

The across-wind BM has a zero-mean, and the time histories of across-wind BMs are converted to frequency domain to have a better understanding of the complex

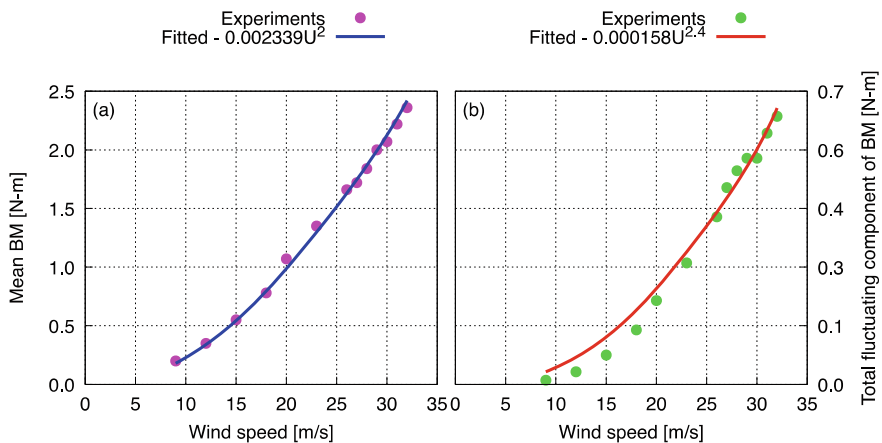


**Fig. 3** Variation of along-wind **a** mean, and **b** total fluctuation component of base BM with wind speeds

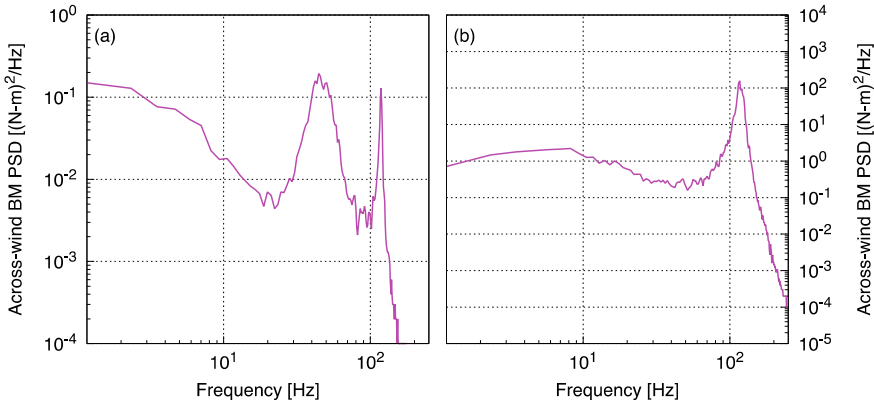


**Fig. 4** Power spectral density of across-wind BM of principal chimney in isolated condition for reduced velocities of **a** 2.38, and **b** 5.54

phenomena. Figure 4 gives the across-wind BM power spectral density (PSD) for reduced velocities of 2.38 and 5.54. At reduced velocity of 2.38, two peaks in the spectrum, one corresponding to vortex shedding frequency and other of structural frequency, are clearly observed and the Strouhal number is calculated as 0.171. It is also evident that with increase in wind speeds, there is increase in vortex shedding frequency. At reduced velocity of 5.54, there is no clear distinction between vortex shedding frequency and natural frequency in the spectrum. This clearly indicates that, at a reduced velocity of 5.54, the principal chimney is in lock-in region, where natural frequency controls the vortex shedding. The average Strouhal number considering values from all the wind speeds is computed as 0.181. Further, the critical wind speed for across-wind is evaluated as 27.15 m/s. The design wind speed for the chimney location under study is 39 m/s at top of the principal chimney, and the  $V_{z_{ref}}$  as per IS 4998:2015 [13] is 38 m/s. Since critical wind speed value is between  $0.5 V_{z_{ref}}$  and  $1.3 V_{z_{ref}}$  as mentioned in IS 4998:2015, across-wind load due to vortex shedding is critical.

### 4.2 Interference Case-1

The model of principal chimney is placed at a S/D ratio of 16 to the model of interfering chimney along with the models of surrounding structures in the corresponding locations for layout-1. Tests are conducted at different wind speeds for various wind angles of attack from  $0^\circ$  to  $360^\circ$ . Wind direction corresponding to the tandem arrangement of principal and interfering chimney is reckoned as  $0^\circ$ . All the models on the turntable are rotated in clockwise direction to conduct the tests for other angle of wind incidences. As mentioned above, as the across-wind response is critical for isolated condition, we discuss the response due to the across-wind



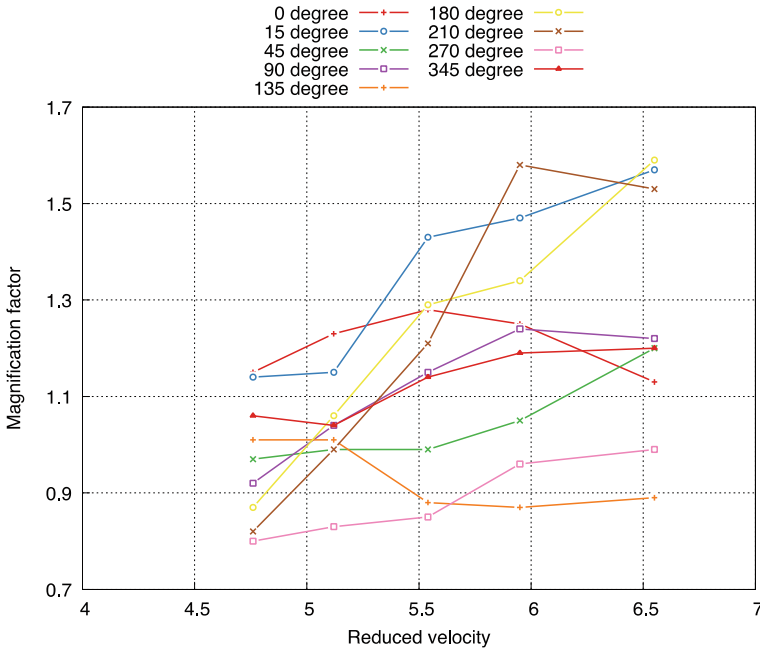


**Fig. 5** Variation of magnification factor with respect to wind speeds and wind incidence angles for interference case-1

in detail in this section for the interference cases also. Interference effects due to across-wind response are usually represented in terms of magnification factor (MF) which is defined as the ratio of the across-wind response of chimney in interference condition to the across-wind response of chimney in isolated condition. Figure 5 shows the variation of MF with respect to different wind speeds for critical angles of attack. The maximum values of MF (MMF) are observed in lock-in region for reduced velocity range of 4.75–6.55 for all the angles of attack considered. For all the test cases performed with varying wind speeds and angles of attack, MMF value of 1.6 is observed for 15°, 180° and 210°. This is also evident from Fig. 6 which shows the envelope of MMF with respect to different angles of attack.

### 4.3 Interference Case-2

For the interference case-2, the model of principal chimney is placed at a S/D ratio of 25 to the interfering chimney along with the models of other surrounding structures in the corresponding locations of the layout-2. For this case also, tests are conducted at different wind speeds and for various angles of wind incidences in the range of 0°–360° covering the critical angles related to tandem, side-by-side and staggered

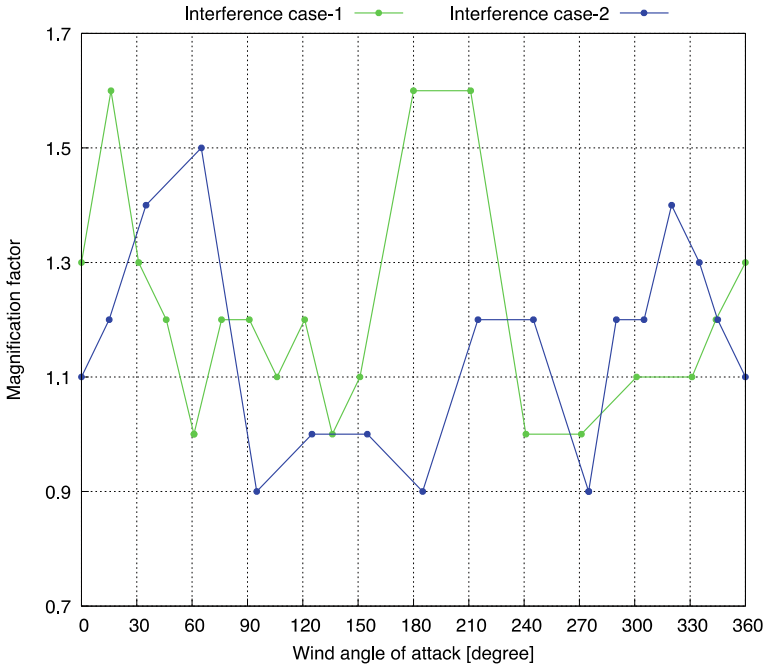


**Fig. 6** Variation of maximum magnification factor with respect to wind incidence angles for interference case-1 and case-2

arrangements. Figure 7 shows the variation of MF with respect to different wind speeds for the critical angles of wind incidences. From the envelope of MMF (Fig. 6) for the interference case-2, the maximum of MMF is observed as 1.5.

Based on the analysis of test data, the peak along-wind BM at the design wind speed of 39 m/s, for both isolated and all interference cases, is evaluated. Also, the resultant BM at critical wind speed, which is defined as the square root of the sum of squares of peak across-wind BM and mean along-wind BM at critical wind speed, is evaluated for isolated and interference cases. Resultant BM at critical wind speed is about 0.8 times its along-wind BM at design wind speed for the isolated case. For the interference cases, the ratio between resultant BM at critical wind speed and its corresponding peak along-wind BM at design wind speed for each angle of incidence is calculated. Maximum ratios of 1.25 and 1.05 are observed for case-1 and case-2, respectively. However, maximum resultant BM is 1.04 and 1.03 times the maximum peak along-wind BM from all angles of wind incidences for case-1 and case-2, respectively. From these values, it is clearly evident that the interference effects are predominant in both along-wind and across-wind directions depending upon the angle of wind incidence.

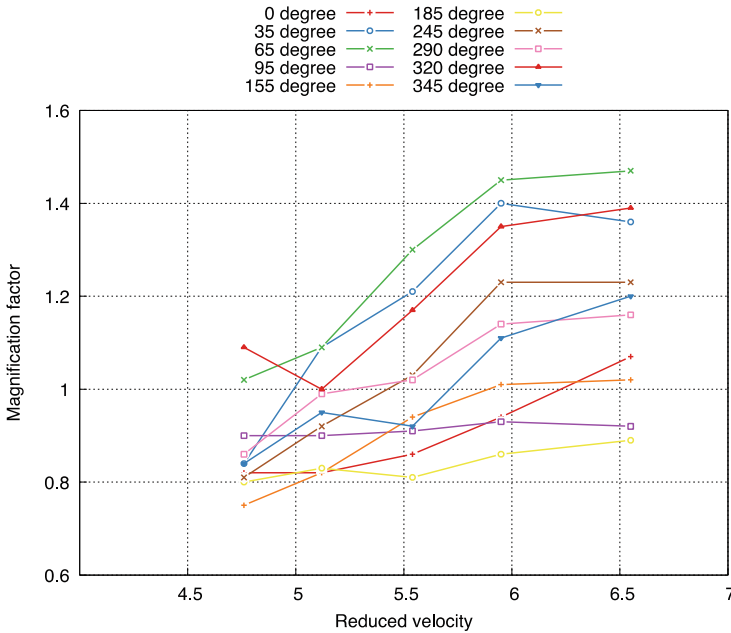


**Fig. 7** Variation of magnification factor with respect to wind speeds and wind incidence angles for interference case-2

## 5 Conclusion

Wind-induced interference effects on a 125 m tall chimney due to the presence of surrounding structures including a 275 m tall chimney for two different interference cases are assessed using wind tunnel studies. Experimental setup and results are briefly discussed in this paper. The results pertaining to BM at base are only discussed. The maximum values of the MF from the envelope of the MMF are observed as 1.6 and 1.5 for case-1 and case-2, respectively. Interference effects are predominant in both along-wind and across-wind directions depending upon the angle of wind incidence for the tested interference configurations. The paper presents only case study related to specific configurations. In addition to this specific study, systematic investigations are needed to establish the individual roles of the location of 275 m tall chimney and other surroundings structures as a whole in creating group effects.

## References

1. Zdravkovich M (1987) The effects of interference between circular cylinders in cross flow. *J Fluids Struct* 1(2):239–261
2. Gowda BL, Sreedharan V, Narayanan S (1993) Vortex induced oscillatory response of a circular cylinder due to interference effects. *J Wind Eng Ind Aerodyn* 49(1–3):157–166
3. Kareem A, Kijewski T, Lu PC (1998) Investigation of interference effects for a group of finite cylinders. *J Wind Eng Ind Aerodyn* 77:503–520
4. Gu Z, Sun T (1999) On interference between two circular cylinders in staggered arrangement at high subcritical Reynolds numbers. *J Wind Eng Ind Aerodyn* 80(3):287–309
5. Liu X, Levitan M, Nikitopoulos D (2008) Wind tunnel tests for mean drag and lift coefficients on multiple circular cylinders arranged in-line. *J Wind Eng Ind Aerodyn* 96(6–7):831–839
6. Niemann HJ, Kasperski M (1999) Interference effects for a group of two reinforced concrete chimneys. *J Fluids Struct* 13(7–8):987–997
7. John AD, Gairola A, Ganju E, Gupta A (2011) Design wind loads on reinforced concrete chimney—an experimental case study. *Procedia Eng* 14:1252–1257
8. Sun Y, Li Z, Sun X, Su N, Peng S (2020) Interference effects between two tall chimneys on wind loads and dynamic responses. *J Wind Eng Ind Aerodyn* 206:104227
9. Su N, Li Z, Peng S, Uematsu Y (2021) Interference effects on aeroelastic responses and design wind loads of twin high-rise reinforced concrete chimneys. *Eng Struct* 233:111925
10. ACI 307 (2008) Code requirements for reinforced concrete chimneys (ACI 307-08) and commentary. American Concrete Institute Farmington Hills
11. Rajora R, Veeravalli SV, Ahmad S (2020) Aerodynamic interference of straight and tapered cylinder pairs near the first critical wind speed. *J Wind Eng Ind Aerodyn* 201:104171
12. IS 875 (Part 3) (2015) Code of practice for design loads (other than earthquake) for buildings and structures, Part 3. Bureau of Indian Standards, New Delhi
13. IS 4998 (2015) Criteria for design of reinforced concrete chimneys. Bureau of Indian Standards, New Delhi

# Studies on 1:300 Scale Wind Tunnel Simulation of Atmospheric Boundary Layer Characteristics Under Open Terrain Conditions Using a State-of-the-Art Boundary Layer Wind Tunnel



Sumit Dubey , S. Arunachalam , Sanjeev Gupta, Rajendra Singh, Sumit Gandhi , and Nitin K. Samaiya 

**Abstract** Physical simulation of atmospheric boundary layer characteristics is very important for wind tunnel testing of models on buildings and structures. A 1:300 scale flow simulation under open terrain conditions was conducted satisfactorily, in the recently established state-of-the-art boundary layer wind tunnel at JUET Guna, Madhya Pradesh, India. The size of the test section is 3.5 m ( $W$ )  $\times$  3.0 m ( $H$ )  $\times$  22 m ( $L$ ). Using a combination of a trip board and floor roughness cubes, profiles of mean velocity, turbulence intensity and spectrum of wind speed were measured and compared with values recommended in the literature, including IS code and ESDU guidelines. The power law coefficient of the mean velocity was 0.16 and the value of turbulence intensity at 600 mm model height was 0.11. The measured spectra of wind speeds at different heights in model showed a good comparison with von Karman power spectrum to a scale of 1:300.

**Keywords** Boundary layer wind tunnel testing · Turbulence intensity · Power spectrum

---

S. Dubey (✉) · S. Arunachalam · R. Singh · S. Gandhi · N. K. Samaiya  
Wind Engineering Application Centre, Jaypee University of Engineering and Technology, Guna,  
MP, India  
e-mail: [sumit.dubey@juet.ac.in](mailto:sumit.dubey@juet.ac.in)

S. Gupta  
JAL India Pvt(Ltd)., Noida, India

© The Author(s), under exclusive license to Springer Nature Singapore Pte Ltd. 2024  
S. G. Rajasekharan et al. (eds.), *Proceedings of the 9th National Conference on Wind Engineering*, Lecture Notes in Mechanical Engineering,  
[https://doi.org/10.1007/978-981-99-4183-4\\_14](https://doi.org/10.1007/978-981-99-4183-4_14)

## 1 Introduction

Boundary layer wind tunnel (BLWT) testing is an internationally accepted practice for experimentally investigating the wind induced loads and responses on scaled models of different buildings and structures. Recently, a state-of-the-art BLWT has been established at the Wind Engineering Applications Centre, Jaypee University of Engineering and Technology at Guna in Madhya Pradesh, to meet the growing needs of the construction industry for civil engineering structures. A fundamental requirement for the wind tunnel testing is proper physical simulation of the characteristics of atmospheric boundary layer as per scaling laws. In this paper, details of physical simulation of ABL characteristics corresponding to an open terrain category, with a flow scale of 1:300, are presented. Using a trip board and floor roughness cubes as vortex generators, profiles of mean velocity, turbulence intensity and spectrum of wind speeds were simulated satisfactorily. The simulated results are showing good comparison with IS code and ESDU guidelines.

## 2 Experimental Studies

A view of the artificial arrangement of a set of roughness blocks and a trip board for the experiment is shown in Fig. 1. A trip board of 200 mm height and roughness cubes of size 40 mm spread on the floor of the test section length (with a longitudinal and lateral spacing of 160 mm c/c) were adopted to simulate the open terrain conditions. Mean velocity measurements were taken at location at the center of the turntable.



**Fig. 1** Experimental setup for terrain simulation studies

### 3 Mean Velocity Measurements (with Vortex Generators and BTR Arrangement)

The mean velocity was measured using a standard pitot tube and a differential pressure indicating meter which was corresponding to 11 m/s at the pitot height of 600 mm. The variation of mean velocity profile along the height is shown in Fig. 2. The mean velocity profile characteristics are analyzed using standard logarithmic law and power law equations. It is apparent that the values of shear friction velocity,  $u_*$ , and aerodynamic roughness length,  $z_0$ , are sensitive to a range of lower heights being considered for their evaluation.

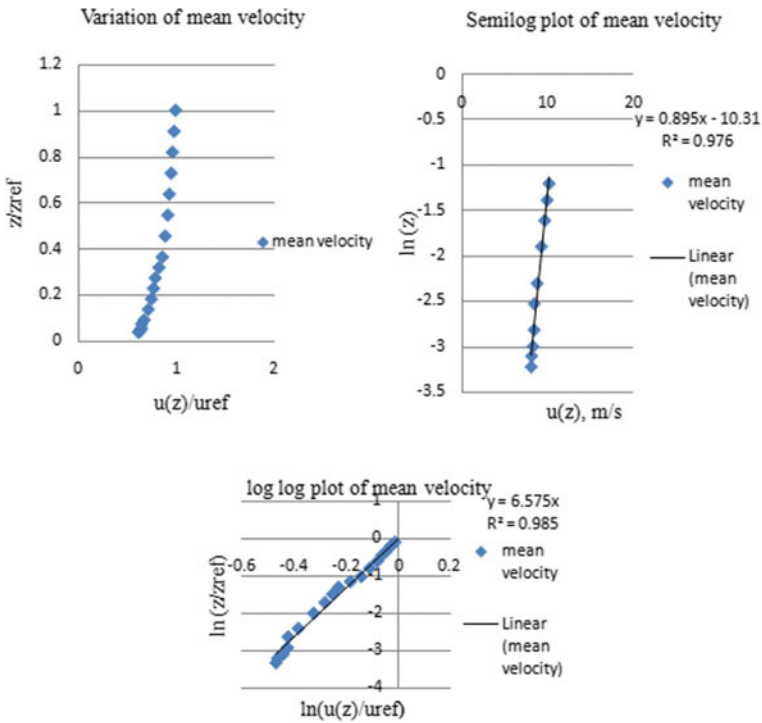


Fig. 2 Variation of mean velocity profile with height

### 4 Turbulence Intensity Measurements (with Vortex Generators and BTR Arrangement)

Fluctuating velocity measurements were measured using a hot wire anemometer system. Using the 3D traverse system, measurements were taken at different levels along the height varying between 40 and 1200 mm above the tunnel floor. It is to be noted that due to HWA probe support mounting on the transverse, at lower levels between 4 and 30 cm, flow disturbance was observed. Consequently, for this height region, a correction factor of 15% was applied and the corrected turbulence intensity values are plotted in the Fig. 3.

The measured  $I_z$  profile from wind tunnel data is plotted in Fig. 4, with a target scale ratio of 1:300. A good agreement can be seen for  $I_z$  profiles with respect to IS code and ESDU code and wind tunnel experimental profiles.

**Fig. 3** Variation of turbulence intensity profile with height

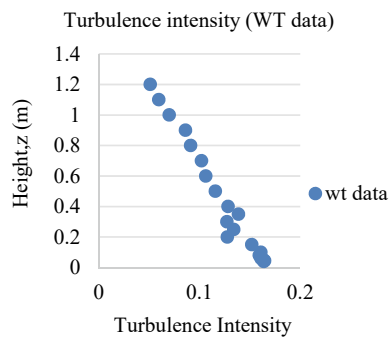
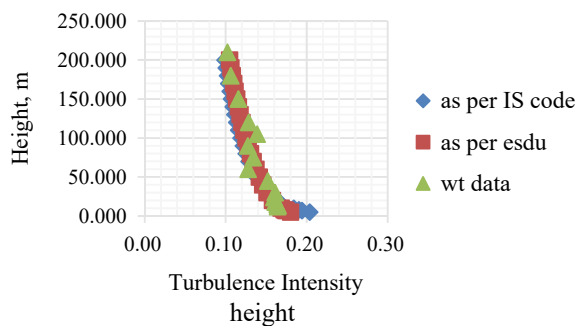


**Fig. 4** Variation of turbulence intensity profile with height





## 5 Power Spectrum Analysis and Evaluation of $L_{ux}(z)$ Values at Different Heights in the Wind Tunnel

As per the concept of terrain simulation in a wind tunnel, it is required that the pattern of distribution of wind energy over different eddy frequencies shall be the same both in the nature and in wind tunnel. Technically, this implies that the power spectrum of wind speed ( $U$ -component) generated from the time traces of fluctuating wind velocity in the wind tunnel shall reasonably match with that of the theoretical wind spectrum, such as von Karman spectrum, Davenport spectrum, Simiu spectrum. In the literature, von Karman spectrum is widely used to represent the theoretical wind spectrum to describe the spectrum occurring in full-scale conditions. Hence, for the present study, the wind tunnel spectrum is compared with von Karman spectrum and thereby the model scale is determined. More details can be seen in Ref. [1].

The von Karman spectrum is given by the following equation:

$$\frac{nS_u(n)}{u_*^2} = \frac{4X_k}{(1 + 70.78X_k^2)^{5/6}}, \quad (1)$$

$$\text{where } X_k = nL_{ux}(z)/u(z), \quad (2)$$

and it is termed as reduced frequency. It is defined in terms of the frequency,  $n$ , mean wind speed,  $u(z)$ , and the turbulent length scale factor,  $L_{ux}(z)$ , for the  $U$ -component wind along  $x$ -direction. The term  $L_{ux}(z)$  represents the size of maximum eddy in the atmosphere.

For an open terrain, Cook proposed [2] the following equation for evaluating the length scale parameter,  $L_{ux}(z)$ , as:

$$L_{ux}(z) = 25z^{0.35}z_0^{-0.063}, \quad (3)$$

where  $z_0$  is the roughness height and  $z$  is the respective height. Equation (3) is recommended in ESDU guidelines. It is reported that uncertainties in values of  $L_{ux}(z)$  using Eq. (3) can be as much as  $\pm 30\%$  [2]. A typical value of  $z_0 = 0.03$  m is used in Eq. (3) for an open terrain category.

The degree of stationarity of the recorded measurement and the length of the measurement are quoted to significantly influence the estimates of  $L_{ux}(z)$ . According to Simiu and Scanlan, for example, for an open terrain, at an elevation of 150 m,  $L_{ux}(z)$  varies between 120 and 630 m with an average value of 450 m. This clearly indicates that in full-scale conditions, recommended values of  $L_{ux}(z)$  are having greater levels of uncertainty.

For the present analysis, Eq. (3) is used to evaluate  $L_{ux}(z)$  values in full-scale conditions, they are matched with corresponding values of  $L_{ux}(z)$  values in wind tunnel, and accordingly, the length scale value is determined.

Counihan [1, 2] also has proposed the following expression to evaluate  $L_{ux}(z)$  values which are valid in the range of  $10 \text{ m} < z < 200 \text{ m}$ .

$$L_{ux}(z) = Cz^m, \tag{4}$$

where  $C$  and  $m$  are parameters which depend on the roughness length,  $z_0$ . Generally, it is observed that values of  $L_{ux}(z)$  predicted using Eq. (4) are significantly higher than those obtained by using Eq. (3) [1].

Based on the time histories of fluctuating velocities measured in the wind tunnel at different heights, using MATLAB software, and with pwelch spectrum command function considering twenty times averaging of data samples and fifty percent overlapping of data samples, power spectrum plots were generated. It is well known from the theory that at high-frequency region, the slope of the curve when drawn between the reduced spectrum,  $\left(\frac{nS_u(n)}{\sigma_u^2}\right)$ , versus the non-dimensional frequency,  $\left(\frac{n*z}{u(z)}\right)$  will follow the trend of  $n^{-5/3}$ , where  $n$  is the frequency. This trend is experimentally exhibited in plot in Fig. 5.

And the semi-theoretical von Karman curve is also super-imposed on each of the above curves. This validates a good simulation of ABL conditions in the wind tunnel from the spectrum distribution point of view. In Fig. 5, all the power spectra curves at different heights ranging from  $z = 100$  mm to  $z = 1000$  mm are plotted which show a good trend with Karman spectrum when plotted between  $\left(\frac{nS_u(n)}{\sigma_u^2}\right)$  and  $\left(\frac{n*z}{u(z)}\right)$ . Also, the decreasing trend of  $\left(\frac{nS_u(n)}{\sigma_u^2}\right)$  with  $\left(\frac{n*z}{u(z)}\right)$  was clearly following  $n^{-5/3}$ , as discussed above.

It is apparent from the above figures that the trend shown by power spectra when plotted in a reduced scale at different heights is following Karman spectrum.

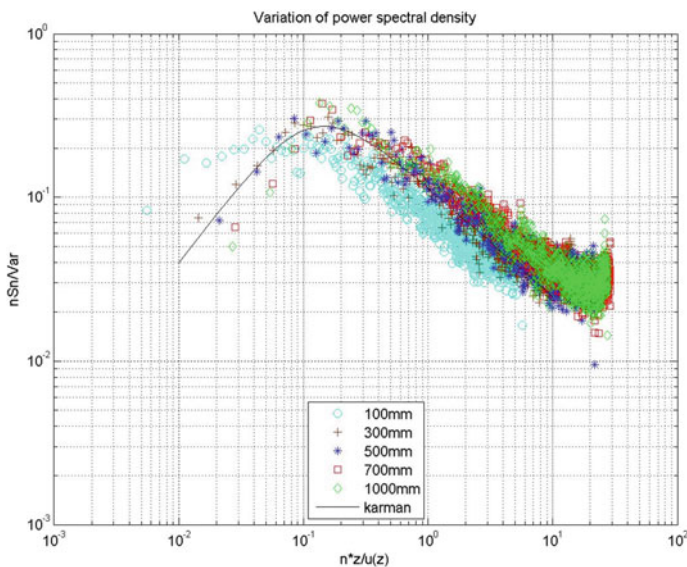
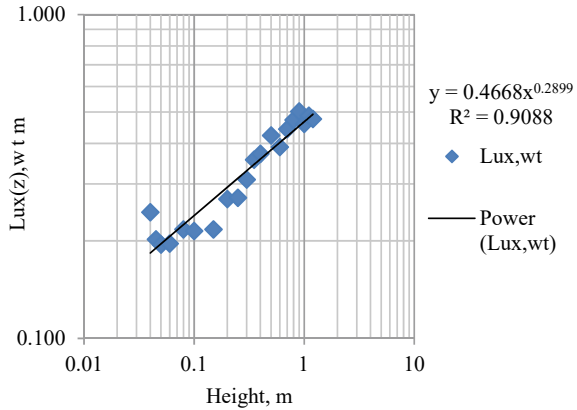


Fig. 5 Variation of reduced power spectra at different heights

**Fig. 6** Variation of  $L_{ux}(z)$ , wt as a function of height



The variation of  $L_{ux}(z)$ , wt in wind tunnel as a function of different heights is plotted in Fig. 6, which follows a power law equation given by:

$$L_{ux}(z), wt = 0.47z^{0.29}. \tag{5}$$

It may be noted that the above equation is similar in form to Counihan equation.

The value of length scale  $L_{ux}(z)$  as calculated through standard spectrum equation is matching with ESDU in nature to a scale of 1:300. At reference height of 12 m, considering scale of 1:300, the estimated  $L_{uz}$  value and ESDU value are matching well. As given in literature,  $L_{ux}(z)$  parameter at any given height has a scatter and hence is valid for a range of flow scale. Since it is already shown that mean velocity profile and turbulence intensity profile are providing a flow scale (1:300), the same flow scale is tried with  $L_{ux}(z)$  also; the values of  $L_{ux}(z)$  along the heights in full scale (1:300) are compared with corresponding full-scale value as per ESDU and it is found that there is a reasonable matching among them as shown in Fig. 7.

## 6 Summary and Conclusions

The simulation was carried out for an open terrain category using hotwire anemometry system. The vortex generator system used included a 200 mm high trip board and a set of roughness cubes of 40 mm size spaced at 160 mm c/c in both ways. No spire was used in this experiment. Based on wind tunnel simulation, the values of aerodynamic roughness length,  $z_0$ , shear friction velocity,  $u_*$ , and the power law coefficient,  $\alpha$ , are evaluated as 0.000033 m, 0.45 m/s, and 0.156, respectively. The above experimental results of mean velocity profile, turbulence intensity and length scale show a good comparison with corresponding recommended full-scale values, with a flow scale of 1:300. The simulated profiles of mean velocity and turbulence intensity are compared well with corresponding profiles recommended by IS Code

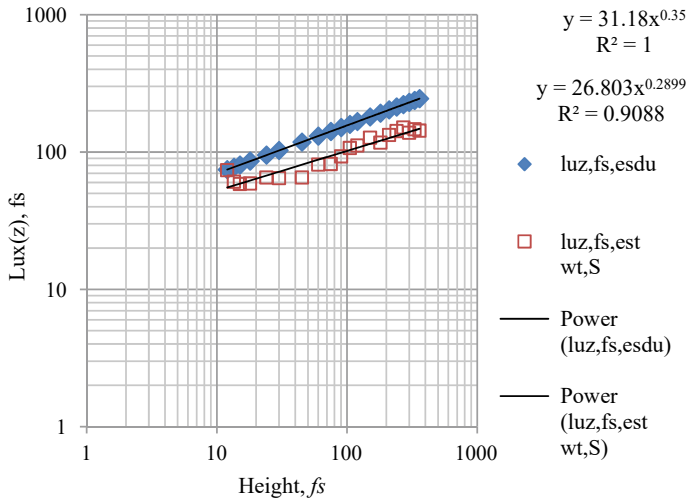


**Fig. 7** Variation of  $L_{ux}(z)$  with height

875 (Part3) [3] and ESDU guidelines. The power spectra of wind speed at different heights based on wind tunnel test data showed a good comparison with von Karman spectrum, widely being used in the literatures.

Therefore, the present simulation demonstrates that the above vortex generator system can be utilized for further experiments and simulation studies in a flow scale of 1:300 using BLWT at JUET, Guna.

**Acknowledgements** The authors sincerely thank the Vice Chancellor of JUET for his support and staff of JUET Guna for their technical assistance rendered.

## References

1. Simiu E, Scanlan RH (1996) Wind effects on structures, 3rd edn. Wiley Interscience, Newyork
2. Cook NJ (1985) Designers guide to wind loading of building structures, part 1, building research establishment. Butterworth publishers, First edn, U.K.
3. IS:875 (PART 3) (2015) Design loads (other than earth quake) for buildings and structures-code of practice, part 3 wind loads. Bureau of Indian standard, New Delhi, India

# Tornado Speed Estimation Using Convolutional Neural Networks (CNNs) and Long Short-Term Memory (LSTM)-Based Video Processing Approach



Anirudh Marathe, Prerit Daga, Sudha Radhika , and Yukio Tamura

**Abstract** Many natural processes in the universe occur in a rotational motion, such as the formation of drastic events including tornadoes and cyclones. For the past few decades, research has progressed to estimate the occurrence of such unpredictable small-scale meteorological events and their damage paths and to estimate the amount damage caused. In the case of short-lived yet disastrous tornadoes, it is possible to track the damage path. However, to estimate the damage through the Fujita Scale (*F*-Scale) or the Enhanced Fujita scale (EF-Scale), it is still necessary to rely on Radar Data Acquisition (RDA) systems working on Doppler effect to estimate the wind speed. For this, the equipment needs to be placed in the vicinity of where the tornadoes form, so they are often at risk of being damaged. Thus, in the current research, the tornado speed is estimated using video processing and AI techniques: Convolutional Neural Networks (CNNs) and Long Short-Term Memory (LSTM) conjointly. A video model of a rotating tornado (without translational motion) is artificially generated with a tracking object inside it. The wind speed is estimated by tracking the speed of this object caught in the tornado's whirl. CNN in combination with LSTM effectively predicts the shift of the object in each frame of the video in comparison with a reference frame.

**Keywords** Wind engineering · Tornado · Video processing · CNN · LSTM · Python

---

A. Marathe · P. Daga · S. Radhika (✉)  
BITS-Pilani Hyderabad Campus, Hyderabad, India  
e-mail: [sradhika@hyderabad.bits-pilani.ac.in](mailto:sradhika@hyderabad.bits-pilani.ac.in)

Y. Tamura  
School of Civil Engineering, Research Center of Wind Engineering, Environment, and Energy,  
Chongqing University, Chongqing, China

Wind Engineering Research Center, Tokyo Polytechnic University Atsugi Campus, Atsugi, Japan

Y. Tamura  
e-mail: [yukio@arch.t-kougei.ac.jp](mailto:yukio@arch.t-kougei.ac.jp)

## 1 Introduction

A tornado is a violently rotating column of air that extends from a thunderstorm and comes into contact with the ground taking a massive shape and creating a lot of damage along the traversed course. These strong winds occur across the world, including the USA which experiences it more often than other regions. Every year, the USA reports about 1300 tornadoes of varying intensities [1]. The intensity of a tornado is measured on Enhanced Fujita (EF) Scale [2], which takes in to account 28 different damage indicators. The speed of tornado can describe tornadoes more accurately. However, it is difficult to estimate the speed due to the massive damage it can cause to the equipment like anemometer that is used to measure wind speed. Radar-based techniques [3], used by WSR-88D and Mobile Doppler Radar, provide some means for prediction and measurement of speed using Doppler effect. The WSR-88D Doppler radar network obtains weather information (precipitation and wind) based upon returned energy generated and received at the Radar Data Acquisition (RDA) unit. This helps in forecasting tornadoes, but due to physical limitations such as beam spreading and radar horizons, the rotation as well as speed of tornado cannot be measured. Mobile Doppler Radars can be positioned close enough to the storm to resolve the rotation within the tornado itself. This method is still not widely used to measure speed. This project aims at using image and video processing techniques to estimate the speed of rotation of still tornadoes. The image processing systems in development and use today have become more robust, accurate, and less expensive with the advancement in digital camera technology. The low cost of development, use and maintenance of digital cameras, and related processing equipment make them widely used for image processing-based applications. Various such techniques are already in use for tracking and measuring the speed of objects in linear motion like vehicles in traffic. Such techniques require capturing of video at known frame rate and observing the motion. They can also be used for the linear path traversed by a tornado. Using similar techniques with modifications, the speed of rotation can be estimated.

## 2 Methodology

The speed of rotation of an object is calculated as number of rotations completed in unit time. For identifying a complete rotation, we mark a reference point on the rotating object that appears at the same location after certain amount of time. Since a tornado is composed of winds, it is difficult to mark a single or group of identifiable points to make the required observations. Therefore, we choose an object stuck in the tornado and observe its location to identify the speed at which it rotates or appears to rotate, which is assumed to be the speed of the tornado [4].

The proposed methodology follows the approach of tracking an object stuck in the tornado to calculate the speed. Video processing is used to identify the object and its

position in each frame. First, the speed is calculated in terms of no. of frames traversed for unit rotation and then that is converted into the number of rotations per unit time based on the rate of frame capture. Furthermore, as the video obtained through a digital video camera is not continuous, we expect that the speed obtained through this process needs to be scaled to obtain the original speed. This scaling factor is obtained by first calculating the speed of a reference rotating object of known speed and comparing it with the actual speed. This scaling factor will be specific to camera frame rate and can be used to scale the speed obtained for the test object.

In this work, we have used a rotating cone as a simplified model of a tornado and a certain pattern on the cone as the object under observation. This approach helps in simplifying the creation of desired relations that can later be extended to complex tornado simulations.

The various steps that are involved are explained as follows:

## ***2.1 Video Capturing***

The video of a tornado is captured from a high-resolution digital camera at a known frame rate. A higher frame rate will ensure that less rotations are skipped while capturing the motion and better accuracy is expected.

## ***2.2 Preprocessing***

The video is to be processed frame by frame. Each frame is converted from RGB to grayscale image for performing fast operations.

## ***2.3 Reference Object Selection***

A distinguishable object that was stuck in the tornado is selected from a frame of the video in initial run. The location of the object in the frame is noted.

## ***2.4 Reference Object Tracking***

As the tornado rotates, the object location in the subsequent frames also changes. On completion of a rotation, the location on the corresponding frame is expected to be same as that in the initial frame. The location will repeat again in further rotations. This seems straightforward for human observer; however, to perform this

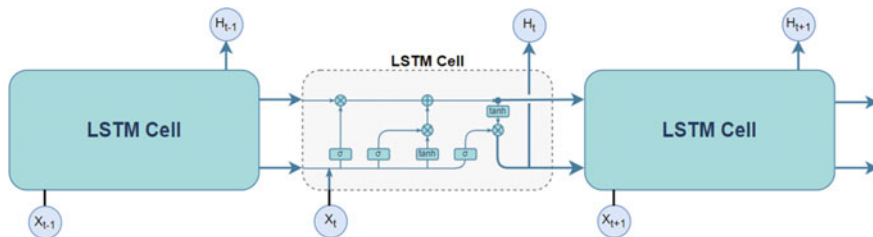


Fig. 1 LSTM internal structure

task through video processing, an object tracking algorithm is used. The results of this step are then used in speed estimation, as explained in next subsection.

The object tracking methodology used in this work makes use of CNN and LSTM that is explained as follows.

A reference object stuck in tornado is selected and cropped from the first frame of the video. To track its position in the subsequent frame, the same set of pixels needs to be searched. Now, since an object may change its orientation and shape while rotating, we cannot directly search the cropped image with good accuracy. Hence, we use Convolutional Neural Network (CNN) to predict the location of cropped image in the subsequent frames [6–8]. The learning method used is Long Short-Term Memory (LSTM) [9, 10].

**LSTM.** In LSTM, a training set of first few frames is given to the network. It stores in its memory buffer, the information gained from each training frame. Based on the information stored, it can predict the next frame of a video, using backpropagation method. The block diagram of an LSTM network is shown in Fig. 1. Each rectangular box is a neuron/cell. The internal working of an LSTM network is described as follows from left to right direction.

$\sigma$  represents the sigmoid function which takes input as  $X_t$  and  $H_{t-1}$ . This sigmoid function is called as the forget gate. The task of the forget gate is to decide how much of the previous output data will be forgotten and how much of the previous data will be used in next steps. Both these inputs are multiplied with their corresponding weights and added and fed to the sigmoid function  $\sigma$  where the output could be in range of 0–1.

The middle  $\sigma$  and  $\tanh$  function together comprises the input gate and new memory cell. They decide what relevant information can be added from the current step. The inputs to the new memory cell are  $X_t$  and  $H_{t-1}$ . These inputs are taken and multiplied together with their corresponding weights and fed to sigmoid function. The multiplication output of input gate and new memory cell could be any value between 0 and 1. The previous cell state input and the output from forget gate are multiplied and added with the total output of input gate and new memory cell calculated in the previous step to give the current cell state which would be given to the next cell [10].

The rightmost  $\sigma$  and  $\tanh$  function together comprises the output gate. This gate tells the amount of relevant information to be taken from the cell state. The inputs  $X_t$



and  $H_{t-1}$  are taken and multiplied together with their corresponding weights and fed to sigmoid function. The output of sigmoid function and the final value of cell state obtained from by passing the cell state through the tanh function are both taken and multiplied to produce the hidden state output which would be given to the next cell.

## 2.5 Speed Estimation

Let  $r_{\text{obs}}$  denote the number of rotations observed in  $f_{\text{obs}}$  frames. This gives speed in terms of number of rotations per frame. Multiply this with frame rate fps (frames per second) to obtain the observed speed,  $s_{\text{obs}}$ , in rotations per second, Eqs. (1 and 2).

$$s_{\text{obs}} = \frac{r_{\text{obs}}}{f_{\text{obs}}} \times \text{fps}, \quad (1)$$

$$s_{\text{obs}} = r_{\text{obs}}/\text{sec}. \quad (2)$$

Eq. (2) is called as the ‘‘observed speed’’, as a camera setup with frame rate less than the actual speed of tornado can skip a few rotations. Thus, a scaling factor is calculated from a reference training video, which is used here to scale the observed speed into actual speed, Eq. (3).

$$\text{scale} = \frac{r_{\text{actual}}/\text{sec}}{r_{\text{obs}}/\text{sec}}. \quad (3)$$

The scaling factor of Eq. (3) is obtained by first running the model on a video of an object of known speed. Then, we calculate the speed of rotation of desired object,  $s_{\text{cal}}$ , using Eq. (4).

$$s_{\text{cal}} = \text{scale} \times s_{\text{obs}}, \quad (4)$$

## 3 Experimental Setup and Results

The proposed method was implemented in Python, on a video sequence of a tornado model represented by a rotating cone Fig. 2, simulated through VPython [4], a python-based programming language to write programs that generate navigable real-time 3D animations.

The number of rotations to be simulated were manually given, and based on the time taken for the completion of simulation, the speed was calculated in rotations per second (rps) [5]. This gives ‘actual speed’ or ‘known speed’ [9]. Since the idea is to identify complete rotations of the cone, a texture was applied to the cone image.

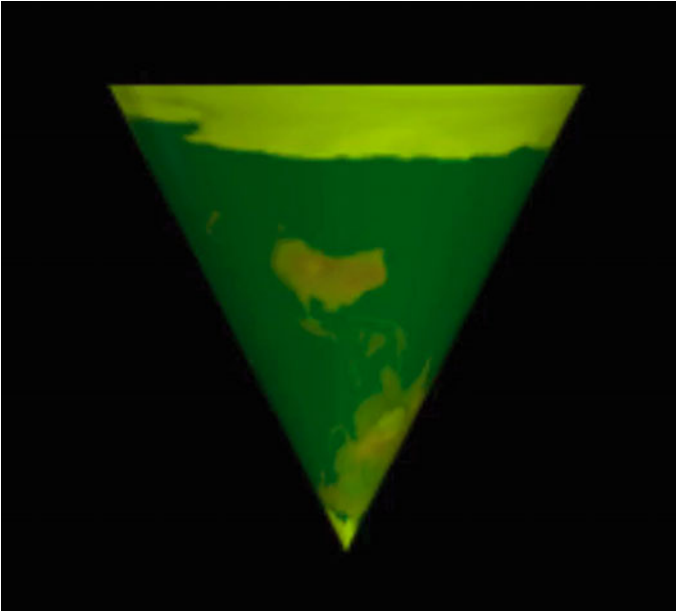


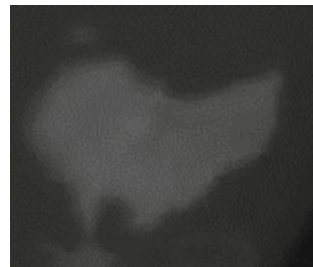
**Fig. 2** Frame of simulated cone

The texture consisted of an inverted map of the Earth, on which any known and distinguishable place could be identified in each frame. Screen recorder was used to obtain the video of the rotating cone. The 'frame rate' of the screen recorder was taken to be 30 fps.

The reference object image chosen is an inverted map of Australia, Fig. 3.

The location of image and frame number is noted and compared. The difference between the first two frames that contain the reference image at almost the same location as the first frame is calculated, and subsequent frame numbers are estimated.

**Fig. 3** Reference object



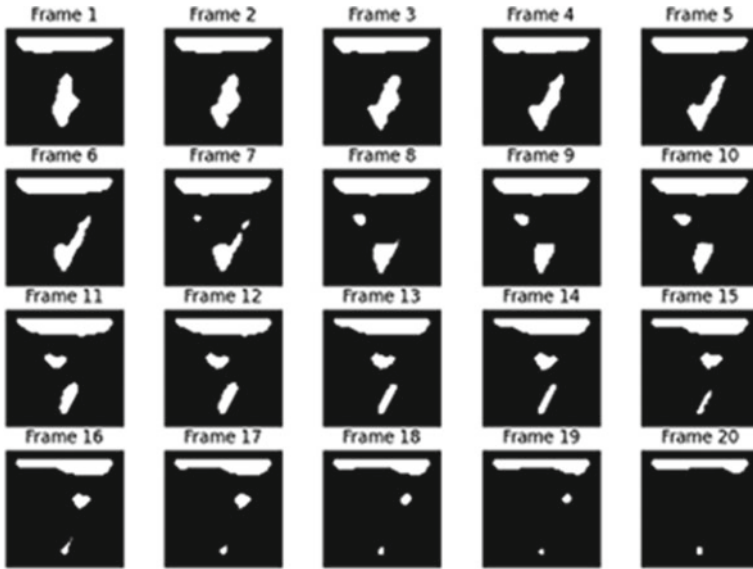


Fig. 4 Dataset for training

### 3.1 Results for LSTM Network Next Frame Prediction Computation

A dataset is created by taking 6000 image frames from a sample video. Out of these, 20 images are taken as training dataset, Fig. 4.

After the model has been trained, all the weights of trained model are then provided as the input to the prediction module. The LSTM model is tested for the next frame prediction. And, the next frame prediction is done with a frame rate of 5 fps as shown in Fig. 5.

### 3.2 Scale Calculation from Video of Known Speed

The model was first run on a rotating cone with speed = 4 rps. Figure 6 shows a frame where the reference object is marked.

Table 1 shows the estimated and actual values of frame numbers along with the location of the reference image.

Each row in the table corresponds to a calculated rotation of the object image which is identified with position. From Table 1, we observe that though the first rotation takes about 14 frames per observed rotation the subsequent rows show an average of about 15 frames per observed rotation. Using this value and frame rate of 30 fps in Eq. (2), we get

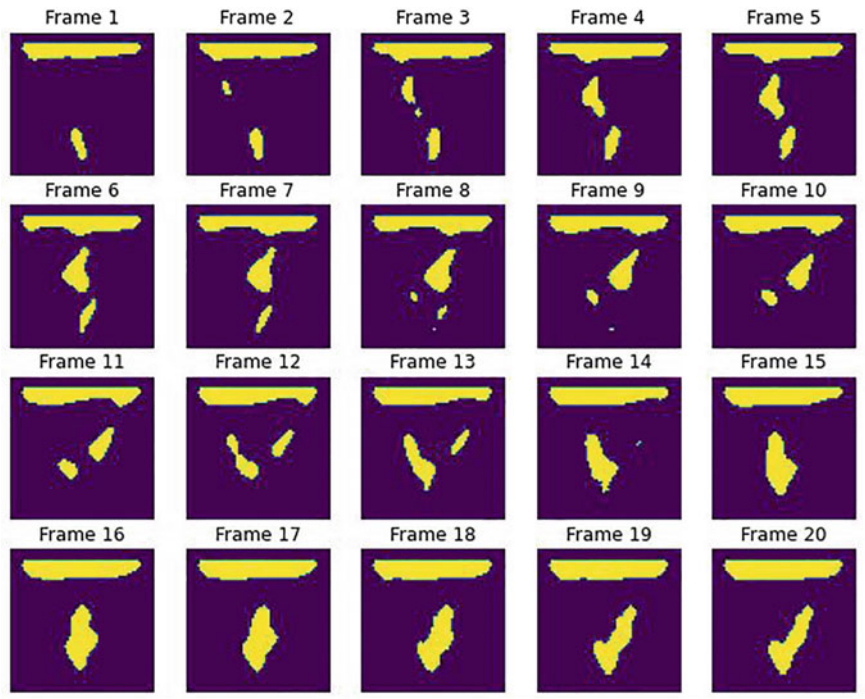
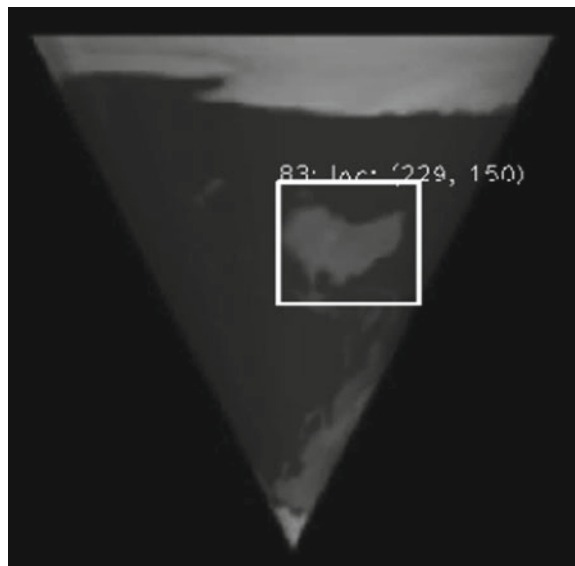


Fig. 5 Predicting the next video frames using dataset for the trained model

Fig. 6 Reference object identified and marked



**Table 1** Predicted and actual values of frame numbers along with the location of the reference image (for reference video)

S No.	Frame No.		x-location	Frame difference	Remarks
	Predicted	Actual			
1	–	8	251	–	
2	–	22	253	14	
3	36	37	198	15	
4	50	52	241	15	x-location to far to be considered as complete rotation
5	64	60	214	8	
6	78	76	255	16	
7	92	91	249	15	
8	106	106	243	15	
9	120	121	237	15	

$$s'_{\text{obs}} = 2 \text{ rps.} \quad (5)$$

We use this value and the actual speed of 4 rps in Eq. (4) to obtain scaling factor, Eq. (6):

$$\text{scale} = \frac{4 \text{ rps}}{2 \text{ rps}} = 2. \quad (6)$$

Thus, one calculated rotation at a frame rate of 30 fps is equivalent to two actual rotations. We used this factor to estimate the speed of another rotating object.

### 3.3 Speed Estimation for Video 2

A rotating cone was again simulated with a speed of rotation = 2.11 rps. This was captured as a video at 30 fps. Table 2 shows the various values of frame location for each match of reference object image.

Following the procedure mentioned earlier, we obtained *estimated speed*  $\approx 2.14$  rps. This shows that our model estimates the speed with about 98.6% accuracy.

**Table 2** Predicted and actual values of frame numbers along with the location of the reference image (for test video)

S No.	Frame No.		x-location	Frame difference
	Predicted	Actual		
1	–	7	212	–
2	–	33	205	14
3	59	63	198	15
4	85	78	220	15
5	111	108	214	8
6	137	138	207	16

## 4 Conclusion

The proposed method can be used to measure the rotational speed of a tornado from a video sequence. The method works quite well for simulated models of tornado and can be extended to tornados in real world, with constraint of objects stuck in the tornado being identifiable by the code. Since models are usually of lesser speed as compared to the actual tornados, videos captured at higher frame rate can be helpful. This work does not consider the orientation and position changes of the reference object and the hiding and unhiding of the object that happens in real tornado. A more robust object tracking can be used to enhance the results on real tornados.

## References

1. Radhika S, Tamura Y, Matsui M (2012) Use of post-storm images for automated tornado-borne debris path identification using texture-wavelet analysis. *J Wind Eng Ind Aerodyn* 107:202–213
2. Sabareesh GR, Matsui M, Tamura Y (2011) Characteristics of surface pressures on a building under a tornado-like flow at different swirl ratios. *J Wind Eng* 8(2):30–40
3. Radhika S, Tamura Y, Matsui M (2017) Application of remote sensing images for post-wind storm damage analysis. In: *Remote sensing of hydro-meteorological hazards*. 1st edn. Taylor & Francis
4. Sabareesh GR, Matsui M, Tamura Y (2013) Characteristics of internal pressure and resulting roof wind force in tornado-like flow. *J Wind Eng* 112:52–57
5. Elhamod M, Levine MD (2013) Automated real-time detection of potentially suspicious behavior in public transport areas. In: *IEEE transactions on intelligent transportation systems*, vol 14(2), pp. 688–699
6. Freer JA, Beggs BJ, Fernandez-Canque HL, Chevrier F, Goryashko A (1996) Automatic video surveillance with intelligent scene monitoring and intruder detection. In: *30th annual 1996 international carnahhan conference in security technology in security technology*, pp 89–94
7. Lai TY, Kuo JY, Liu C-H, Wu YW, FanJiang Y-Y, Ma S-P (2013) Intelligent detection of missing and unattended objects in complex scene of surveillance video. In: *2012 international symposium on consumer and control in computer (IS3C)*, pp 662–665
8. Chowdhury A, Tripathy SS (2014) Detection of human presence in a surveillance video using fuzzy approach. In: *2014 international conference on signal processing and integrated networks (SPIN)*, pp 216–219

9. Bird ND, Masoud O, Papanikolopoulos NP, Isaacs A (2005) Detection of loitering individuals in public transportation areas. In: 2005 IEEE transactions on intelligent transportation systems, pp 167–177
10. Ajitha A, Goel M, Assudani M, Radhika S, Goel S, Design and development of residential sector load prediction model during COVID-19 pandemic using LSTM based RNN. Electric Power Syst Res